# THE NEW HRIBF RECOIL MASS SPECTROMETER — PERFORMANCE AND FIRST RESULTS

By

Thomas Nelson Ginter

Dissertation

Submitted to the Faculty of the

Graduate School of Vanderbilt University

in partial fulfillment of the requirements

for the degree of

DOCTOR OF PHILOSOPHY

in

Physics

December, 1999

Nashville, Tennessee

Approved: Date:

_____ _____

_____ _____

_____ _____

_____ _____

_____ _____

ACKNOWLEDGMENTS

I am pleased to acknowledge the support of my Vanderbilt research advisors, Professors J. H. Hamilton and A. V. Ramayya. I am also very grateful for the encouragement and guidance I received from the many people I worked with at the Holifield Radioactive Ion Beam Facility of Oak Ridge National Laboratory. In particular, I thank Carl J. Gross and Krzysztof Rykaczewski — Krzysztof, for the enthusiasm and vision he has instilled into the work on $^{150}$Lu and $^{146}$Tm presented here, and Carl, for performing the difficult and sometimes painful task of serving as my mentor on a day-by-day basis over the years as I learned about a recoil mass spectrometer and obtained a Ph. D. I am deeply indebted to Robert Grzywacz of the University of Tennessee for his support on matters both technical and scientific and, most importantly, for his very dear friendship that has kept me sane over the past two years.

The research at Vanderbilt University is supported by the U. S. Department of Energy under grant No. DE-FG05-87ER40407. Oak Ridge National Laboratory is managed by Lockheed Martin Energy Research Corporation for the U. S. Department of Energy under contract No. DE-AC05-96OR22464.

PHYSICS

# THE NEW HRIBF RECOIL MASS SPECTROMETER — PERFORMANCE AND FIRST RESULTS

THOMAS NELSON GINTER

Dissertation under the direction of Professors J. H. Hamilton and A. V. Ramayya

For more than 15 years recoil mass spectrometers have served as an important tool for nuclear structure and decay studies. This dissertation documents the newest addition to the family of these devices: the Recoil Mass Spectrometer (RMS) housed at the Holifield Radioactive Ion Beam Facility (HRIBF) of Oak Ridge National Laboratory. The HRIBF RMS is a new generation device that combines a momentum achromat in front of the traditional components of a recoil mass spectrometer to give higher beam rejection (particularly in inverse reactions), higher mass resolution, and more space around the target and focal plane for multi-detector arrays. This dissertation shows how the RMS fits into the context of existing devices, provides a detailed description of the RMS in terms of its ion optics, and describes the efforts to commission the RMS both in terms of calibration and in terms of characterizing its performance. This dissertation demonstrates the power of the HRIBF RMS as a mature research tool by discussing some of the work carried out with the device. Emphasis is placed on proton emission studies including two particular cases of this work: the study of the odd-odd proton emitters $^{150}$Lu and $^{146}$Tm. For $^{150}$Lu a new short-lived proton transition was identified, while for $^{146}$Tm new proton transitions were identified possibly from the population of excited states in $^{145}$Er.

Approved_____ Date_____

Approved_____ Date_____

TABLE OF CONTENTS

LIST OF FIGURES

LIST OF TABLES

# CHAPTER I

## THE ROLE OF RECOIL MASS SPECTROMETERS IN NUCLEAR SPECTROSCOPY

A wide variety of experimental tools facilitate the study of nuclear structure physics. Recoil mass spectrometers are one of the field's more versatile devices. The environment these instruments provide makes possible highly selective, highly sensitive experiments needed to tackle the challenging problems of modern day nuclear spectroscopy. When combined with the appropriate detector systems, recoil mass spectrometers provide the high channel selectivity needed to study nuclei very far from stability which are weakly populated in nuclear reactions. This dissertation will document the commissioning and performance of one particular device — the Recoil Mass Spectrometer (RMS) at the Holifield Radioactive Ion Beam Facility (HRIBF) of Oak Ridge National Laboratory. This powerful new generation recoil mass spectrometer was initiated at Vanderbilt University about twelve years ago. The RMS was designed by a collaboration between Idaho National Engineering Laboratory, Texas A. & M. University, and Vanderbilt University. [1]. Financial support to purchase the RMS came from the Georgia Institute of Technology, the Idaho National Environmental and Engineering Laboratory, Louisiana State University, Oak Ridge Associated Universities, Oak Ridge National Laboratory, the State of Tennessee, the University of Maryland, the University of Tennessee, the U. S. Department of Energy, and Vanderbilt University. The RMS is the central component of the HRIBF nuclear structure experimental end station. The research results presented here will demonstrate the contribution that this new device is already making to just one area of nuclear structure physics.

This first chapter provides a brief introduction to the science of nuclear structure. It discusses the role played by recoil mass spectrometers in this science. It introduces the HRIBF RMS and shows what makes this next generation device stand apart from its predecessors.

Chapter II provides a detailed look into the workings of the HRIBF RMS by exploring the device in terms of ion optics. Chapter III reports on how the RMS was commissioned by describing its calibration and performance. Chapter IV illustrates the performance of the RMS as a powerful new

tool for nuclear spectroscopy by discussing its use in the study of two proton emitting nuclei ($^{150}$Lu and $^{146}$Tm) and by presenting the results of this research.

## Nuclear Structure

The task before us — understanding a new manifestation of an experimental tool and evaluating its performance — demands at least an overview of the field it serves: nuclear structure physics. We briefly look into the issues and questions that drive the field and then sketch the approaches used to grapple with those questions.

### Goals

The Chart of Nuclides serves as a road map to the known nuclei by providing a concise summary of their vital statistics. While symbolizing the progress of nuclear structure physics which is characterized by the meticulous collection and assembly of data sometimes involving strenuous experimental effort, the chart does not convey the spirit that drives the field. What drives the field is much more than merely the search for another box on the chart, a better lifetime measurement, or a more complete level scheme. The purpose of this section is to show how the field of nuclear structure takes its place among the other disciplines of human inquiry by in some way addressing the question of who we are by understanding the world in which we live.

According to our current conception of the universe, there are four fundamental forces governing the interaction of matter with matter: the gravitational force, the electromagnetic force, the weak force, and the strong force. What is truly amazing is not how much we know about these forces, but how little we know about one of them: the strong force. Our ignorance about the strong force is particularly profound in the context in which the interaction most commonly manifests itself — in the nucleon-nucleon interaction within the many body system of the nucleus. The science of nuclear structure physics is one field with the task of addressing this fundamental question.

The thousands of isotopes, with their rich variety of phenomena to be measured and studied, give us many approaches to the difficult challenge of understanding the strong interaction. While much progress has been made, there is much work yet to do. Not only have we not yet begun to exhaust the countless ways of applying the many phenomena of nuclear structure to gain access

into the mystery of the strong force, but also we have not yet even conquered the full territory in which these phenomena manifest themselves. The gaping hole in the Chart of Nuclides between the studied nuclei and the neutron drip line offers the promise of many new phenomena and insights through studies of nuclear matter under new extremes in the proton/neutron ($Z/N$) ratio. As our experimental capabilities progress, the nuclear worlds we can explore extend to systems farther and farther from stability. As we push our investigation into such nuclei, perhaps some effect that is too weak to be measured in the known nuclei, yet crucial to unwrapping the mystery of the strong force, will manifest itself. As we approach nuclei at the extremes, who knows what part of the behavior we observe in nuclear matter will change, what part will stay the same, what new behavior we will uncover, and what all of this can tell us about the strong interaction.

Another fundamental conception about our universe that we can explore in the realm of nuclear spectroscopy is quantum mechanics. Each isotope provides a unique laboratory for studying the interplay of quantum mechanical observables. The study of nuclear matter give us the chance to gain new insights into the formalism of quantum mechanics. The nucleus is a unique quantum many body system with too many particles to be treated on a one-by-one basis and too few to apply quantum statistics. Perhaps one day these systems can give us the insight into what lies behind this formalism.

Another area of human inquiry addressed by nuclear spectroscopy is the field of nuclear astrophysics. By making careful measurements of the half-lives of nuclei far from stability, of the existence of isomers, and of reaction cross-sections, not only do we probe the mechanisms powering far away stars, but we also learn more about our own home planet by understanding how the abundances of elements we observe here were generated in stellar processes.

The study of nuclear structure may also have much more immediate and practical consequences for humanity. Our capability to model complex systems will perhaps more than anything else define the next revolution in the progress of our civilization. Not only are computational techniques a necessary tool for building an insight into the science of nuclear structure, but also the computational challenges presented by nuclear structure provide a fertile ground for exploring and expanding the limits of computational science. The challenge of modeling the nuclear many-body system on a nucleon-by-nucleon basis provides an expandable system just at the limits computational modeling

capability. Larger nuclear systems are complex enough to be beyond our present computer modeling capability, yet simple enough to be within reach of the near-term advances of our computational ability. These systems offer a rich variety of observable phenomena; the ability of models to predict these phenomena can serve as a stringent test of the success or failure of our attempts to apply new computational resources. Meanwhile, our attempt to model nuclear systems could turn out to be the exercise that leads to the crucial insights into understanding the strong force. More complete and precise data to feed these models is necessary for progress to continue; likewise, the models help guide and inspire new measurements.

It is clear that the study of nuclear structure is pursued as an area of basic research without an eye to the technologies it could spawn. However, basic nuclear research has had an enormous impact through new technologies on diverse fields of human endeavor ranging from medicine to defense to art. There is no way to guess how the nuclear structure discoveries of today will shape the human society of tomorrow. Two possible future technologies which could rest on present day research efforts are $\gamma$-ray lasers and the transmutation of high-level radioactive waste into less hazardous waste with energy production as a byproduct.

## General Overview of Experimental Techniques

The study of nuclear structure requires collecting the results of many laborious measurements. Fortunately, each attempt to learn new details about the nuclei can be fascinating not only because of the insight such details can offer into the fundamental questions, but also because of the sheer pleasure from the intellectual challenge of applying the ever evolving experimental tools to overcoming the ever increasing technical demands. This section shows how nuclear structure research fits into the more general context of nuclear physics. It also reviews in very general terms how it is possible to extract data from nuclei that allow us to address the questions that ultimately drive this research.

There are currently three major types of experimental nuclear physics work funded by the U. S. Department of Energy. One arena for research is the Relativistic Heavy Ion Collider (RHIC) located at Brookhaven National Laboratory. The mission of this facility is to explore nuclear matter in the realm of high temperature and density produced in the collision of 100 GeV beams of heavy ions.

Researchers hope to discover and study a new phase of nucleonic matter where the nucleons are no longer identifiable as separate entities. This Quark-Gluon Plasma (QGP) is believed to have existed in the early universe immediately after the Big Bang.

Another arena for nuclear science work is the Thomas Jefferson National Laboratory. This facility's research is based on a high-intensity 4 GeV continuous beam of electrons. This beam serves as a probe for nuclear matter at the sub-nucleonic level.

A third arena for nuclear research is in the context of interactions produced with low energy beams of ions or heavy ions. Three of the Department of Energy Laboratories pursuing this work are the ATLAS Accelerator Facility at Argonne National Laboratory, the 88 Inch Cyclotron Facility at Lawrence Berkeley National Laboratory, and the Holifield Radioactive Ion Beam Facility at Oak Ridge National Laboratory. Another major laboratory pursuing this work is the National Superconducting Cyclotron Facility at Michigan State University which is funded by the National Science Foundation. In addition, there are several smaller university-based centers funded — for example, one at Yale University and another at the University of Washington. It is in this arena that nuclear structure research takes place.

The nuclei of interest are short-lived and, thus, are not available in our natural environment. These short-lived nuclei must therefore be produced directly in reactions or as the result of the decay of nuclei that are often even more short-lived than the nuclei being studied. The ways to gain information about the structure of nuclear systems include: observing their de-excitation from high energy states; observing how they behave as projectiles or targets in reactions (by measuring things like cross-sections, excitation functions, and reaction modes); observing how they decay (by examining such things as the types of decay, the half-lives, the energies, and the branching ratios); and measuring isotopic masses. The excited states studied are typically populated promptly following the creation of the nucleus in a reaction or as the product of a decay.

The usual approach taken by physicists who use low energy ion beams to conduct nuclear structure research is to direct the beam composed of ions of one isotope onto a target composed of atoms of some other isotope. As the beam strikes the target, a range of nuclear reaction products are generated. The reaction products generated depend on the reaction processes that take place. These reaction processes, in turn, depend on the energy of the beam. Examples of some of these processes

include fragmentation reactions at higher energies, fusion-evaporation reactions at medium energies, and Coulomb excitations at lower energies. The experimenter can control the range of isotopes produced by selecting the beam energy, the beam isotope, and the target isotope. The special advantages and challenges of using radioactive ion beams to extend the range of accessible isotopes are addressed in the section beginning on page 29. Photon and particle detectors placed around the target provide the experimenter with information about the various reactions and reaction products in the target. Particle detectors are useful only to the extent that the target is thin enough for the particles released in the reaction to escape from the target.

A problem with this general approach is that if the isotope of interest is produced in a very low cross-section compared to the other reaction products, it is difficult to identify the events in the detectors belonging to the isotope of interest. Another problem is that the large fraction of beam particles that do not induce reactions can also generate uninteresting events that flood the detectors. The challenge of these studies is to develop ways to deal with these two sources of background events in order to select out the weakly populated reaction channel of interest. Recoil mass spectrometers are one of the tools available for meeting this challenge. These devices can assist with both "in-beam studies" of nuclei produced in reactions as the beam strikes the target and with "decay studies" of nuclei generated in the reaction or in the decay from short-lived nuclei produced in the target.

## Recoil Mass Spectrometers — a Tool for Nuclear Structure Studies

When a beam of heavy ions strikes a thin target with sufficiently high energy to overcome the Coulomb barrier between the nuclei in the beam and target, not only do nuclear reactions take place between these nuclei, but also the new nuclei produced in these reactions recoil out of the target. These "recoils" can be collected and spatially sorted by using a device known as a recoil mass spectrometer. The environment of spatially separated recoils provided by recoil mass spectrometers enable highly sensitive, highly selective experiments that allow the study of the structure of weakly produced nuclei very far from stability. These devices have been used to study nuclei with production yields of less than 0.001% of the total reaction cross-section. This section provides an overview of these devices by describing what they do, how they are used with auxiliary detectors to perform experiments, how they work, and how their performance is characterized.

## What They Do

A good recoil mass spectrometer should perform two important tasks: (1) separate recoils spatially by their mass-to-charge ratio $M/Q$, and (2) prevent the beam particles that pass through the target without reacting from scattering into the focal plane where the recoils are separated. This section discusses the issues involved with these two jobs; it also shows how recoil mass spectrometers fit within the context of other types of separators and thin target devices. Details of working recoil mass spectrometers can be found in References [1, 2, 3, 4, 5, 6, 7, 8, 9, 10, 11, 12].

Because the HRIBF RMS has so far only been used to study the products of fusion-evaporation reactions or the decays of such products, the discussion of recoil mass spectrometers in this dissertation will be limited to this context. These devices can also be used for other types of work: for example, reaction studies or to study the products of deep inelastic reactions. Thus, a "recoil" here is the residual heavy ion that remains after the compound nucleus (formed when a beam nucleus fuses with a nucleus in the target) de-excites by emitting (or evaporating) particles (protons, neutrons, and/or $\alpha$-particles). This residual heavy ion exits the target because of the kinetic energy transfered to it from the beam particle. Because of the loss or pickup of electrons as they pass through the target, the recoils emerge with a distribution of atomic charge states $Q$.

The primary function of a recoil mass spectrometer is to separate the recoils leaving the target according to their mass-to-charge ratio $M/Q$. The location where this spatial dispersion of recoils into groups by $M/Q$ is realized is called the "focal plane". This dispersion generally allows the identification of recoils within a group by mass; ambiguities can arise, however, because recoils with different masses and different charge states can have the same value of $M/Q$. (Ambiguities in general are not a significant problem since only a limited range of masses and charge states are populated within a given reaction.) Figures 1 and 2 show examples from the HRIBF RMS of recoil distributions observed at the focal plane. No $M/Q$ ambiguities arise in Figure 1, making identification of recoils in the groups by mass possible; ambiguities in $M/Q$ cause some of the recoil groups in Figure 2 to overlap, preventing the mass identification of some of the recoils by position alone.

The other primary function of a recoil mass spectrometer is the rejection of scattered beam particles. The use of thin targets to ensure that the reaction products recoil with the right energy distribution means that the recoils are completely dominated by the beam particles that pass through

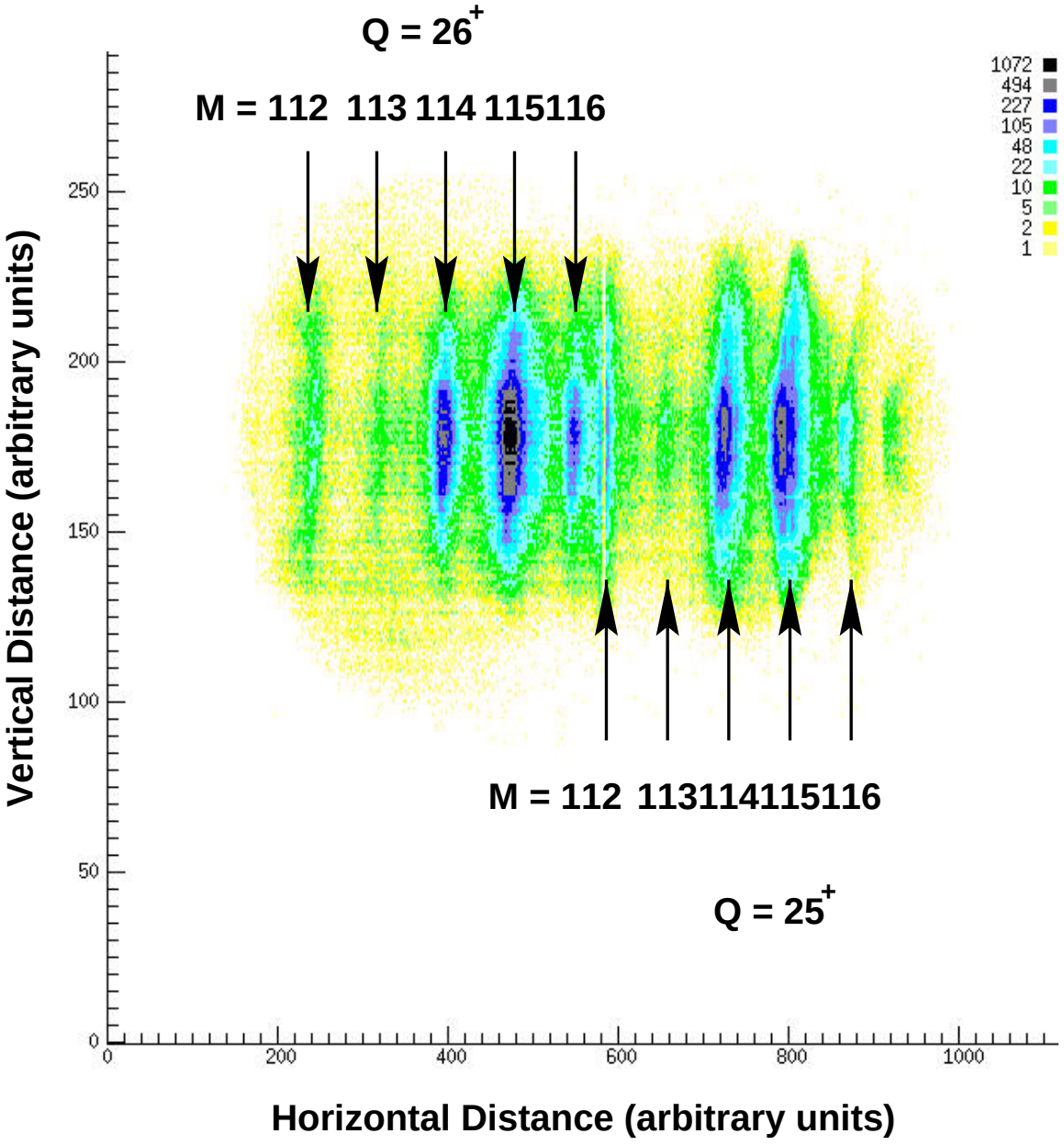


Figure 1: Sample of the spatial distribution of recoils by $M/Q$ from the HRIBF RMS produced by using the $^{60}$Ni($^{58}$Ni, $xp\ yn\ z\alpha$) reaction. The beam energy was 220 MeV and the target thickness was 300 $\mu$g/cm$^2$; the RMS was scaled to accept central ions of $^{114}$Te at an energy of 103 MeV and with a charge state of $25.3^+$. The number of particles observed as a function of position are given by the color code at the upper right corner of the figure. As shown by the labels which indicate the masses and charge states of the recoil groups, the absence of $M/Q$ ambiguities allows the identification of the masses of the recoil groups by their positions alone. Note the absence of a background from scattered beam events in this data. The gap in the center of the figure is an artifact of the data display and does not represent a blind spot in the detector.

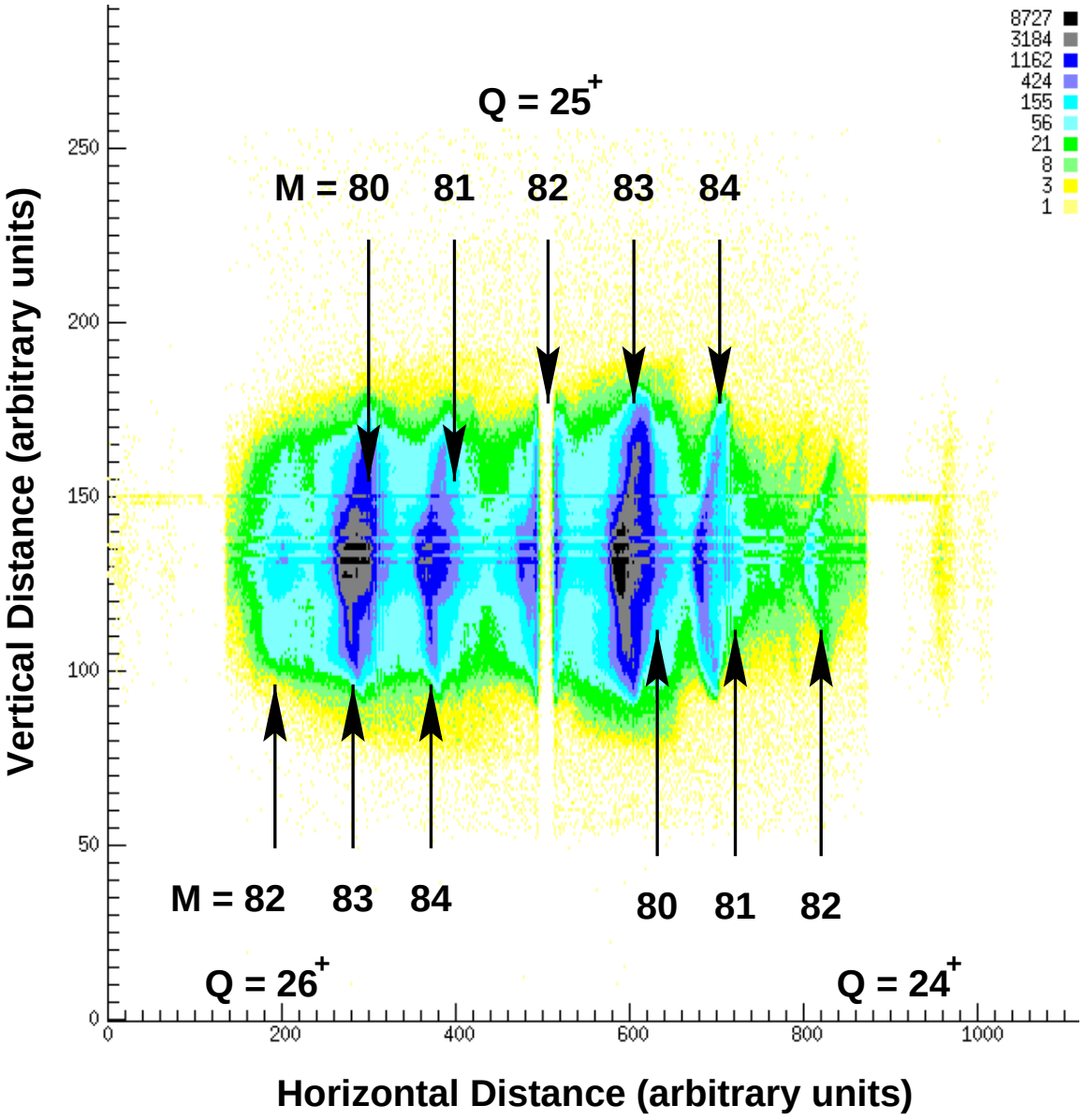


Figure 2: Sample of the spatial distribution of recoils by $M/Q$ from the HRIBF RMS produced by using the $^{28}$Si($^{58}$Ni, $xp\ yn\ z\alpha$) reaction. The beam energy was 208 MeV and the target thickness was 400 $\mu$g/cm$^2$ (with a 900 $\mu$g/cm$^2$ Ta backing placed facing the beam); the RMS was scaled to accept central ions of $^{84}$Mo at an energy of 113.5 MeV and with a charge state of $25.5^+$. The number of particles observed as a function of position are given by the color code at the upper right corner of the figure. As shown by the labels which indicate the masses and charge states of the recoil groups, the presence of $M/Q$ ambiguities prevents the identification of the masses of some of the recoils by their positions alone. Roughly 10% of the data in this plot are from scattered beam events. The gap in the center of the figure is an artifact of the data display and does not represent a blind spot in the detector.

the target without reacting. For the typical beam energies used for reactions at the HRIBF RMS (in the range of 3 to 5 MeV/$A$), the target thicknesses are on the order of 1 mg/cm$^2$ or less. The recoils from fusion-evaporation reactions are concentrated in a fairly small angular range centered around the initial beam direction of 0°. In order to maximize recoil collection efficiency, recoil mass spectrometers must be capable of operating at 0° — the direction in which all of the unreacted beam particles enter. As they are separated from the recoils, these beam particles scatter off of surfaces within the spectrometer with a range of energies and trajectories and can even create new reaction products which then pass through the device. If even a tiny fraction of these "scattered beam" events has the right kinematic and charge characteristics, enough will be transmitted to the final focal plane to flood the detectors. The high sensitivity required for observing exotic nuclei at the focal plane depends very much on the level of beam rejection; if the detectors at the focal plane are swamped with beam events, the rare "good" events will be lost because of dead time and a high background.

In contrast to ion-source based, on-line isotope separators, recoil mass spectrometers are in-flight separators. An on-line isotope separator physically separates nuclei by $M/Q$ which are extracted and ionized from a thick target where they are produced when a beam of ions strikes the target. Thus, an extremely useful feature of a recoil mass spectrometer is the short time scale on which it operates after nuclei are generated in the target. This time scale is determined by the time-of-flight of recoils through the system — typically on the order of 1 or 2 $\mu$s. This feature means that the mass identification it provides can be applied to the study of very short-lived nuclei. Furthermore, this short time scale means that it is possible to preserve correlations between prompt events observed at the target and decay events occurring at the focal plane within a few tens of $\mu$s. These timing advantages are not available in on-line isotope separators because of the time delay involved in extracting the nuclei produced in the thick target. Another advantage of recoil mass spectrometers compared to on-line isotope separators is that what enters the spectrometer is not moderated by intermediate effects (thermalization, ionization, sticking, etc.) present with ion sources. Thus recoil mass spectrometers directly see the nuclei and their kinematic properties resulting from target reactions. Hence, these devices can be used for nuclear reaction and production studies.

Recoil mass spectrometers are not the only type of in-flight or thin target devices used for studies

in nuclear spectroscopy. Tagging separators used for fragmentation studies such as the LISE3 [13] spectrometer at GANIL form another class of spectrometers. Such devices do not so much provide physical separation of the reaction products based on $M/Q$, but instead provide complete isotopic identification of the reaction products by employing the energy loss and time-of-flight techniques available in the context of the higher energy regime of fragmentation reactions. A drawback of such devices is that it is difficult to tag in-beam $\gamma$-ray events observed at the target position because the high count rate prohibits the use of germanium detectors at the target position.

Another type of in-flight or thin target device is a gas-filled recoil separator — for example, the Berkeley Gas-filled Separator [14] at Lawrence Berkeley National Lab or the RITU [15] separator at the University of Jyväskylä in Finland. The primary advantage such devices offer is their high efficiency for collecting recoils. The small amount of gas introduced into these devices allows them to achieve this high efficiency by equilibrating the recoils which leave the target with a distribution of charge states into a trajectory based on an average charge state which fits into the separator acceptance. These devices are capable of physically separating the reaction products from scattered beam particles, but they do not provide good mass separation of the reaction products from each other. Thus, the advantage they offer over recoil mass spectrometers in terms of collection efficiency is offset by the fact that they cannot provide as high a level of channel selectivity based on the separation of recoils by mass.

We conclude this introduction to recoil mass spectrometers by examining a result discussed in a later chapter in terms of how it illustrates spectrometer performance. The case we consider is that of $^{150}$Lu produced in the $^{96}$Ru($^{58}$Ni,$p3n$) reaction with a 315 MeV beam and a target thickness of 540 $\mu$g/cm$^2$ (with a 2 mg/cm$^2$ gold backing placed facing the beam). The reaction code HIVAP [16] predicts a total cross-section for fission and fusion-evaporation events of $\sim$460 mb, for the range of beam energies (292 - 282 MeV) present in the $^{96}$Ru portion of the target. This number is consistent with the value of 470 mb predicted by the reaction code evapOR [17] at a beam energy of 282 MeV. The predicted cross-section for the production of $^{150}$Lu from HIVAP is $\sim$5 $\mu$b; this predicted value is consistent with the estimated value of 3 $\mu$b from the experiment. Hence, $^{150}$Lu represents 0.001% of the total reaction cross-section. Given the fact that roughly 2% of the $^{150}$Lu events observed were from a new short-lived proton emitting state, the $^{150}$Lu nuclei produced that were in this new state

(assuming negligible in-flight losses due to decay) represent something like 0.00002% of the total reaction cross-section.

We can also use these numbers to estimate the amount of primary beam entering the spectrometer compared to the number of recoils. Taking the total reaction cross-section to be 0.5 barns we get a reaction rate for the 5 particle nA beam of $5 \times 10^4$ events/second. The number of beam particles entering the target per second for this beam current is $3 \times 10^{10}$ particles per second. Thus, for every recoil entering the spectrometer, there are something like 600,000 beam particles also entering the spectrometer. Despite this large number of beam particles, there was essentially no background from scattered beam events observed at the focal plane to interfere with the experiment.

The ability to make in-flight separation of recoils by $M/Q$ in a recoil mass spectrometer means coping with the disadvantages of using a thin target: the need to suppress the resulting scattered beam, on the one hand and, on the other hand, the low production yields arising from the limited material in the target and the low beam currents required to prevent target damage. As we shall see from the detection strategies that in-flight $M/Q$ separation make possible, the gain in sensitivity can more than compensate for the inconveniences of using thin targets.

## High Channel Selectivity Through Auxiliary Detector Systems

The $M/Q$ separation and beam suppression capabilities alone offered by recoil mass spectrometers cannot provide the high channel selectivity necessary for studying nuclei very far from stability with production cross-sections lower than around 100 $\mu$b. This high sensitivity comes from the detector systems used together with these devices. This section lists some of the detectors typically used with recoil mass spectrometers and where they are placed; it discusses some of the strategies used for combining these detectors to make possible the highly demanding present day experiments in nuclear structure.

### Detectors and Placement

Detectors are typically placed at two locations at a recoil mass spectrometer. One location is the focal plane where recoils identified by $M/Q$ can be studied by energy loss or radioactive decay. Another position is surrounding the target to detect the prompt radiation emitted shortly after the

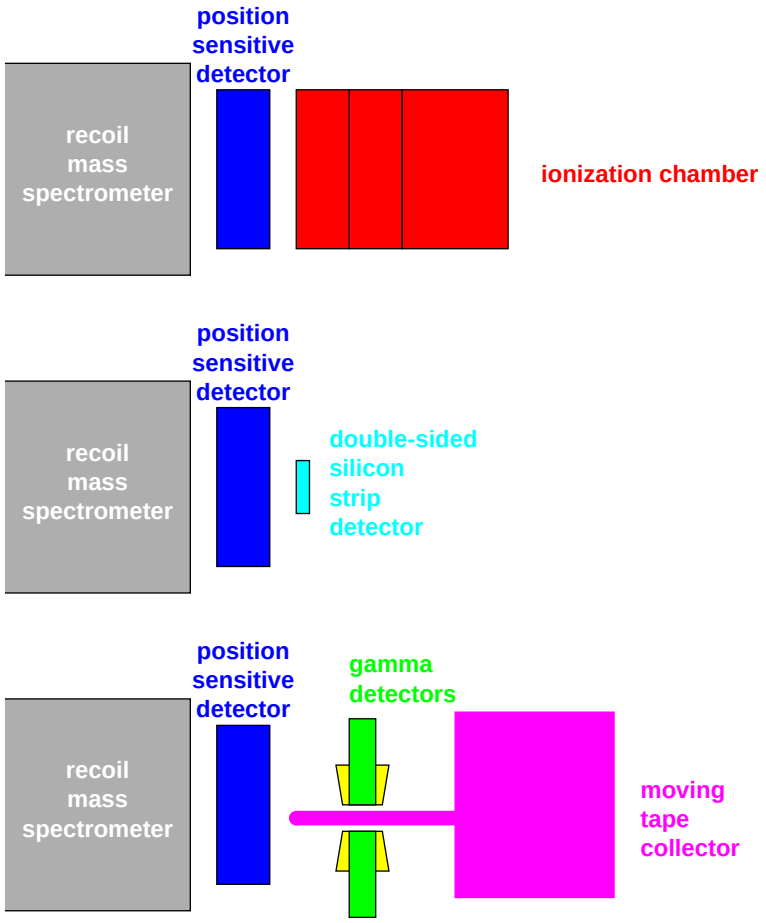


Figure 3: Three common arrangements of focal plane detectors used behind a recoil mass spectrometer show how an ionization chamber, a double-sided silicon strip detector, or a moving tape collector with a detector station might be placed behind a position sensitive detector for different types of experiments.

nuclei are produced. Figure 3 shows a schematic view of three common detector arrangements which can be used at the focal plane. Figure 4 gives a schematic view of a detector setup that might be used at the target position.

Perhaps the most critical detector system used with a recoil mass spectrometer is the position sensitive detector placed at the focal plane to provide $M/Q$ identification and arrival time information for the recoils. Even if this detector is not needed in an actual experiment, the position information it provides is critical for optimizing the spectrometer settings at the beginning of the experiment. These detectors commonly follow one of two designs. One is a gas-filled multi-wire proportional counter; the gas volume is isolated from the high vacuum environment inside the spectrometer by thin windows. The other design uses a micro-channel plate to amplify signals from electrons emitted as the recoils pass through a thin carbon foil extending across the focal plane.

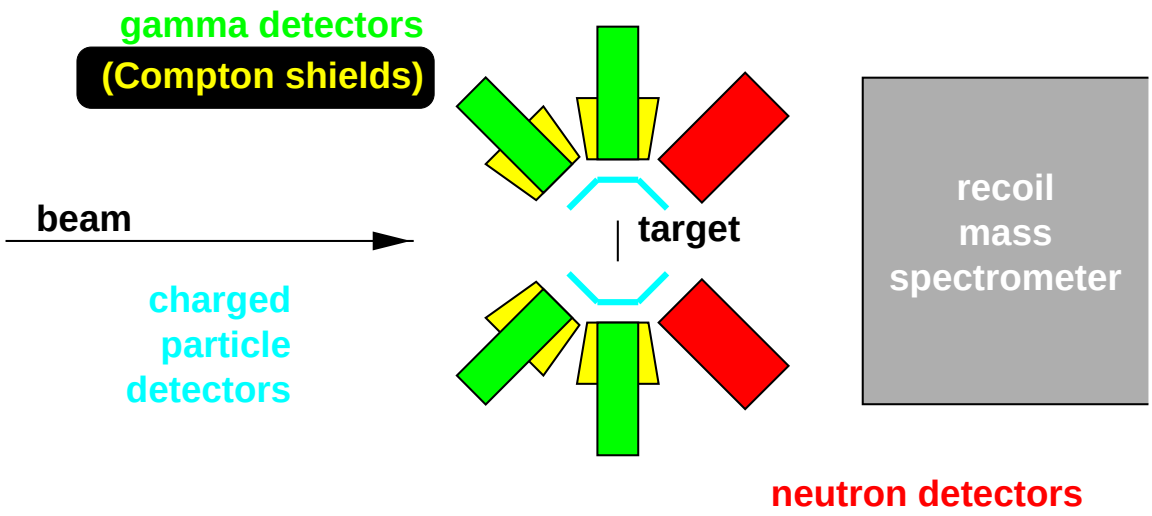


Figure 4: Arrangement of typical target position detectors at a recoil mass spectrometer showing how Compton-suppressed germanium detectors for observing $\gamma$-emission, charged particle detectors, and neutron detectors can be combined in a single setup.

Both of these designs have a high detection efficiency while at the same time allowing the recoils to pass on to other detectors placed downstream. Typically these devices detect and transmit better than 90% of the recoils entering them. The advantage of position sensitive detectors based on the micro-channel plate design is their capacity to handle higher count rates; however, it is more difficult to build such detectors that can cover large focal plane areas.

Other commonly used focal plane detectors include an ionization chamber, a double-sided silicon strip detector, and a moving tape collector. An ionization chamber can be used to provide $Z$-identification of recoils within mass groups based on their energy loss in a gas. These detectors can be made large enough to accept all of the mass groups entering the focal plane. A double-sided silicon strip detector (DSSD) [18] can be used to study the decay of implanted recoils by proton or $\alpha$-particle emission. A moving tape collector may also be used to accept one or more of the mass groups. Movements of the tape are used either to prevent long-lived activity from building up in front of a detector station placed at the focal plane or to transport the activity of the implanted recoils to a detector station away from the background activity of the focal plane. In the latter case a moving tape collector system works by stopping recoils from a particular mass group on a section of movable tape positioned at the focal plane. After some fixed period of time the tape is advanced so that the portion of tape containing the implants is quickly positioned in front of a detector station which can collect decay information about nuclei on the tape. As the decay information is gathered,

a new set of recoils is collected on a fresh section of tape at the focal plane. When the tape advances again these new implants are moved to the detector station and a new fresh section of tape is moved into position at the focal plane to collect new recoils. The time between tape movements is optimized based on the half-life for the activity observed.

Germanium detectors to measure the energies of emitted $\gamma$-rays can be placed either at the target position or at the focal plane. Anti-Compton shields surrounding the germanium detectors can be used to veto events in which $\gamma$-rays Compton scatter out of the germanium crystal and hence give rise to a distribution of energies because the full $\gamma$-ray energy is not deposited in the detector. An array of charged particle detectors at the target can be used to provide additional channel selection of events based on the observation of protons and $\alpha$-particles evaporated from the compound nuclei formed in reactions. Because not much material is needed for charged particle detection, these detectors have a small cross-section for absorbing $\gamma$-rays; hence, they can be placed between the target and the germanium detectors. Neutron detectors placed at forward angles at the target position can also be used to enhance the channel selection.

Techniques

Recoil mass spectrometer experiments typically employ two general strategies. One strategy is to set up detectors in the clean environment of the focal plane (clean because of $M/Q$ selection and the absence of scattered beam) to study the decays of nuclei produced in the target or their isomeric properties. The use of a DSSD to study the decay of nuclei by proton emission is one example of the application of this strategy. Within a given mass group from a particular reaction, there is usually no more than one (odd-$Z$) nucleus expected to decay by proton emission which is produced with a sufficient cross section to be observable; thus, the $M/Q$ identification provided by a recoil mass spectrometer is enough to allow for the unique isotopic assignment of any new decays that are observed.

Another example of this strategy is the use of germanium detectors at the focal plane to study the $\gamma$-emission from nuclei within a mass group that have microsecond isomers. These isomers live long enough to survive the flight time (typically 1 or 2 microseconds) through the recoil mass spectrometer. A clean spectrum of the isomeric decay is obtained by recording the $\gamma$-rays occurring

within a time window of a few tens of microseconds after the arrival of the recoil at the focal plane. This technique has been used, for example, with the velocity filter SHIP at GSI to study [19] the decay of the 3.2 $\mu$s isomer in $^{76}$Rb. The $M/Q$ separation provided by a recoil mass spectrometer is usually enough to provide clean conditions for the study of these isomers, since typically not more than one or two such isomers will be found within any mass group.

Another way to perform decay experiments at the focal plane is to use a moving tape collector to study the decay of recoils from a mass group. A variety of setups can be used at the detector station depending upon the type of decay being studied; typical detectors used include germanium detectors (with and without Compton shields), $\beta$-scintillaters, X-ray detectors, and $e^+/e^-$ pair spectrometers.

The other general strategy employed in recoil mass spectrometer experiments is to use focal plane detectors to tag events of interest observed at the target. One technique involves using the germanium array at the target position together with the position sensitive detector and ionization chamber at the focal plane. The focal plane detectors provide $M/Q$ and $Z$ identification of recoils to provide isotopic tagging of gamma rays observed at the target. The DSSD at the focal plane can also be coupled to the germanium array at the target. This arrangement makes it possible to correlate prompt $\gamma$-rays observed at the target with the known proton or $\alpha$-emission from an exotic nucleus, thus enabling an in-beam study of the nucleus. This technique is known as recoil decay tagging (RDT) [20]. Another idea for tagging prompt target $\gamma$-ray events is to make use of a known $\gamma$-decaying isomer observed at the focal plane as in RDT.

The selection of detector systems and techniques presented here is not intended to be exhaustive. The topics discussed are guided by experiments that have actually been done at the HRIBF RMS.

## How They Work

The recoils enter a recoil mass spectrometer not only with a range of masses and charges, but also with a range of angles and energies. A recoil mass spectrometer must disperse these recoils by their mass-to-charge ratio $M/Q$ alone, and not according to their angles or energies. This section describes how a recoil mass spectrometer accomplishes this task; it also discusses what happens to the flood of beam particles that enter the device after passing through the target without reacting.

The mass of a recoil generated in a fusion-evaporation reaction of course depends on the number

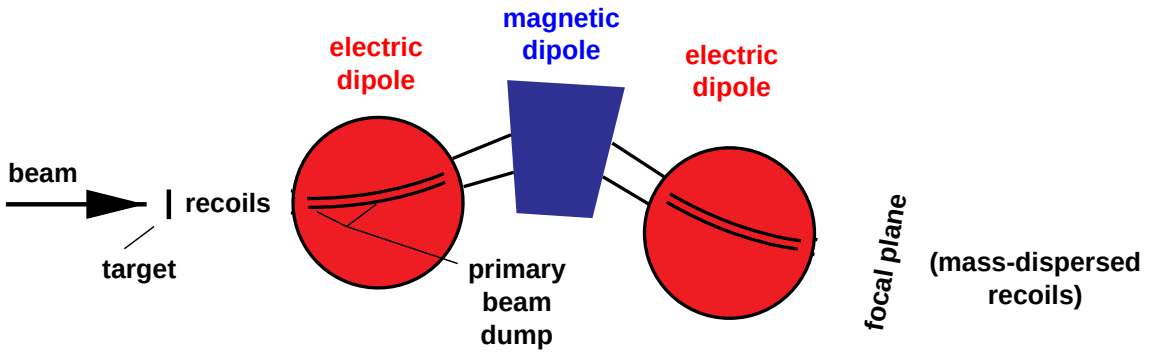


Figure 5: Arrangement of electric and magnetic elements in a split electric dipole mass separator. Also shown is the typical location of the primary beam dump in normal kinematic reactions.

of particles evaporated from the compound nucleus produced in the collision. The charge state of the recoil depends upon how many electrons are stripped from or picked up by the nucleus as it leaves the target and on whether there is significant decay of an excited state by internal conversion. The angle with which a recoil leaves the target depends not only on the impact parameter of the collision that produces it but also on the number, type, and direction of the particles evaporated in the reaction. The angle is also a function of the target thickness and the depth the recoil is formed in the target because of multiple scattering within the target. The energy with which a recoil leaves the target depends on how many particles are evaporated in the reaction and their directions; it is also a function of the depth within the target at which the recoil is formed. A recoil mass spectrometer is a collection of ion-optical bending and focusing elements; these elements are arranged to make use of the fact that the recoils are charged and moving in a vacuum to separate and focus them as a function of their mass-to-charge ratio.

The specific arrangement of elements usually used to provide $M/Q$ separation is known as a "split electric dipole mass separator". This arrangement consists of two electric dipoles and a magnetic dipole arranged as shown in Figure 5. The electric dipoles disperse recoils of a given charge state entering the device according to energy. The magnetic dipole disperses these recoils according to momentum. The magnetic dipole is matched to the electric dipoles in such a way that the energy dispersion it produces exactly counteracts the energy dispersion produced by the electric dipoles. The net effect is that recoils of a given charge state are dispersed at the final focal plane according to their masses alone — recoils of the same mass, even though they have a range of energy values, end up at the same position at the focal plane. (Equations describing the function of magnetic and electric

dipoles will be presented in the discussion of ion optics in Chapter II.) Magnetic focusing elements, typically quadrupole doublets, are placed between the target and the triple dipole arrangement and again between this arrangement and the focal plane to provide geometric focusing of the recoils at the focal plane, to control the image size and dispersion observed at the focal plane, and to enhance the solid angle acceptance from the target.

The very high beam rejection capability that allows recoil mass spectrometers to be used at $0^\circ$ arises from the use of the two separate electric dipole elements instead of only one. For most reactions, since the charge-to-mass ratio $M/Q$ for charge states of the primary beam is sufficiently different from recoils, the beam particles have no way to enter the focal plane directly. The source of beam background in the focal plane is instead from beam particles that scatter or make reactions on the interior surfaces of the spectrometer. Since the beam particles have higher rigidity than the recoils, they strike the anode of the first electric dipole producing a forward spray of reaction products and elastically scattered beam particles with a broad energy distribution. (The location where the beam strikes the spectrometer wall is called the "primary beam dump" and varies depending upon the reaction used to produce the recoils of interest. Figure 5 shows one possible location of the primary beam dump.) The magnetic dipole then selects only a window in momentum/charge of the scattered particles which it passes to the second electric dipole. For many reactions the additional dispersion provided in turn by the second electric dipole can be enough to prevent the scattered particles reaching it from scattering further into the focal plane.

### Other Devices

This section briefly describes some of the recoil mass spectrometers from around the world used for research in nuclear spectroscopy. This discussion provides a context for understanding the unique characteristics of the new HRIBF RMS at Oak Ridge National Laboratory.

The first device to employ the split electric dipole mass separator design is the Recoil Mass Spectrometer (RMS) [6, 7] located at the University of Rochester's MP tandem Van de Graaff laboratory. In addition to the three dipole elements, this machine has a quadrupole triplet behind the target and another quadrupole triplet before the focal plane to control the spatial focusing of the recoils. This device clearly demonstrated the success of the strategy of using two electric dipoles

to achieve excellent beam suppression. The first experiments using the $M/Q$ identification of recoils at the focal plane as a tag for target $\gamma$-rays to enhance channel selectivity were performed at the Rochester RMS. (See, for example, References [21, 22].)

Another important spectrometer is the Recoil Separator (RS) [23] originally located at the Nuclear Structure Facility at Daresbury Laboratory. This device, however, is *not* a typical recoil mass spectrometer because it does not employ the usual split electric dipole arrangement. Instead it uses a pair of velocity filters to reject the beam; these velocity filters are coupled to a dipole magnet to eliminate the velocity dispersion of the recoils and, hence, to achieve $M/Q$ dispersion. What makes this device noteworthy is its role in pioneering important additional detection techniques used with recoil mass spectrometers. These strategies include the use of an ionization chamber for $Z$-identification of target $\gamma$-rays (see, for example, References [24, 25]), use of a strip detector at the focal plane [18], and recoil decay tagging [20]. The device is currently located at the Holifield Radioactive Ion Beam Facility at Oak Ridge National Laboratory where it serves as the centerpiece of the facility's experimental nuclear astrophysics program.

Two other spectrometers based on the split electric dipole design are the recoil mass spectrometer [8, 9] at the Laboratori Nazionali di Legnaro (LNL) in Italy and the Fragment Mass Analyzer (FMA) [10, 11] located at the ATLAS accelerator facility at Argonne National Laboratory. Both of these devices were designed with the benefit of experience gained from the Rochester RMS. Presently the FMA is coupled to the GAMMASPHERE germanium detector array providing the most selective device in the world for in-beam studies.

## Performance Characteristics

It is not feasible to build a recoil mass spectrometer with reasonable $M/Q$ dispersion that can accept the full ranges of masses, energies, charges, and angles for the recoils produced in a reaction. Thus, the design of the device must incorporate trade-offs between how the various acceptance windows are optimized in order to match the general kinds of experiments planned for the device and the operating conditions at the facility where the machine will be used. This section discusses the figures of merit commonly used to evaluate and compare the performances of these devices.

In an experiment with a recoil mass spectrometer, the field settings of the device are specified in

terms of the mass, the energy, and the charge state of a "central ion" that best represents the recoils of interest. It is thus possible to adjust the positions of the energy and $M/Q$ acceptance windows to suit the reaction used and the needs of the experiment by making the appropriate choice for the central ion used to scale the device. Energy acceptance and $M/Q$ acceptance values are used to quantify the ranges of recoils around the central recoil values that can pass through the device.

Recoil mass spectrometers do not have a sharply defined energy acceptance window. The fraction of recoils passed drops from a maximum value at the central recoil energy setting used to define the spectrometer scaling to zero at some energy values above and below the central energy setting. The full-width-half-maximum (FWHM) of this distribution of energies is usually taken to be the energy acceptance range for the spectrometer.

There are several ways to probe the spectrometer energy acceptance experimentally. One way is to use 180° Rutherford scattering of beam particles to knock out target nuclei into the spectrometer. These reactions create a mono-energetic beam of recoils that fill the angular acceptance with a rather flat angular dependence. A germanium detector placed at the target to detect $\gamma$-rays from Coulomb excitation can be used to normalize the counts observed in the focal plane over fluctuations of the beam current. Another essentially mono-energetic probe for exploring the energy acceptance can be obtained by passing a low intensity beam through a thin carbon foil at the target position to split the beam particles that pass through the target without reacting into a distribution of charge states. Since the count rate from charge states at the upper and lower tails of the distribution will be low enough not to overload the focal plane detectors, the spectrometer can be tuned to accept these charge states directly into the focal plane. Particles from the low intensity beam have a very narrowly defined angular spread and thus do not fill the spectrometer's angular acceptance. With either of these probes the response of the spectrometer can be explored over an energy range either by varying the beam energy or by changing the central recoil energy setting used to scale the spectrometer. Another way to get a feel for the energy acceptance of a spectrometer is to use the fusion-evaporation recoils from a reaction and to vary the spectrometer's central recoil energy setting. (In this case it does not really make sense to change the beam energy because effects arising from the fixed target thickness and from the changing cross sections for different reaction channels can be confused with the response of the spectrometer to energy changes.)

The finite energy acceptance of recoil mass spectrometers means that it is crucial to choose the thickness of targets used for experiments appropriately to maximize the yield of reaction products while keeping the energy spread of the recoils within the energy acceptance of the device.

The finite spectrometer $M/Q$ acceptance together with the fact that recoils have a charge state distribution means that only a part of the recoils of a specified mass can be collected at the focal plane. The most probable charge state in the distribution for an isotope typically contains up to 20% of that isotope. Thus, a recoil mass spectrometer with an $M/Q$ acceptance large enough to collect two or even three charge states of a particular mass has an obvious advantage over devices that can only collect one charge state. Making use of more than one charge state of a mass at the focal plane can be a bit more tricky, perhaps requiring baffles at the focal plane to block the uninteresting intervening mass groups or perhaps requiring converging focal plane optics to fit the different charge states onto a small focal plane detector. The transmission drops off for mass groups approaching the edge of the $M/Q$ acceptance window because a larger fraction of the recoil trajectory and energy ranges from these groups end up being collimated by apertures within the spectrometer than is the case for mass groups at the center of the acceptance window. Measuring the $M/Q$ acceptance is straight-forward — it is simply a matter of identifying the mass groups appearing at the focal plane. The intensity of a mass group appearing at one of the edges of the $M/Q$ acceptance window (at one of the edges of the focal plane) can be reduced down to a few percent of the value observed if the spectrometer is scaled to bring the group into the center of the $M/Q$ acceptance window. The values quoted for a recoil mass spectrometer's $M/Q$ acceptance account only for the range of masses appearing in the focal plane; they do not necessarily imply that all the masses within the range appear with a strong enough intensity to be useful.

Mass resolution is a measure of the quality of the mass separation provided by a recoil mass spectrometer. For a given device, this number can vary from experiment to experiment depending on such things as the size and shape of the beam spot, the thickness and uniformity of the target, and on how the reaction used fills the energy and angular acceptances of the spectrometer. Mass resolution is defined as $M/\Delta M$: $\Delta M$ is the width of a mass group on the axis along which the mass groups are dispersed; $M$ is the distance of the center of the same mass group from the point where a recoil of zero mass would appear (calculated assuming a uniform spacing between the mass groups).

Mass resolution is determined simply by projecting the distribution of recoils observed at the focal plane onto the axis of dispersion and reading off channel numbers for peak positions and widths. If the position of recoils observed at the focal plane varies as a function of the position in the direction perpendicular to the axis of dispersion — for example, if aberrations in the optics produce mass groups which are curved into crescent shapes — this method will result in a mass resolution value that is lower than what can actually be achieved with the device. (For most applications, all that really matters is that the mass groups are well separated, not that they are also distributed along vertical lines.) The number calculated for mass resolution is rather sensitive to judgment calls about peak positions and peak widths.

Mass dispersion is a measure of the size of the mass group distribution observed at the focal plane; it does not reflect the quality of the mass separation. It is defined as the distance along the dispersion axis per percent change in mass. In most devices the dispersion can be adjusted to suit the arrangement of detectors used at the focal plane.

Angular acceptance is difficult to measure because the only way to define the solid angle acceptance physically is to place slits between the target and the spectrometer. As discussed in Reference [7], however, slits placed near the target area can lead to uncontrolled beam scattering which can flood the focal plane. The effective angular acceptance for a spectrometer can be adjusted by tweaking element settings — in particular the settings of the elements nearest the target (typically quadrupoles) which are most responsible for gathering the recoils from the target.

Another aspect of recoil mass spectrometer performance worth investigating is the beam rejection capability — especially since this capability is one of the defining characteristics of what these devices do. Unfortunately, the beam rejection ability is hard to quantify because it can vary dramatically from reaction to reaction. One way to measure the beam rejection is to place an empty target frame at the target position and observe how many events make it to the focal plane for different spectrometer settings. This approach does not really reflect how the spectrometer will actually perform in a reaction because the beam entering the spectrometer is not split into a charge state distribution and is not distributed into an angular spread from multiple elastic scattering in the target as it would be for a reaction. (This method can also serve as a check of beam quality; if the beam has a halo, beam particles in this halo scattered from the target frame can make their

way into the focal plane.) Perhaps the use of a thin carbon foil at the target position to split the beam into a distribution of charge states would provide a more realistic test of the beam rejection performance. Another approach which uses an actual reaction to study beam rejection is to employ an energy measuring device at the focal plane (for example, an ionization chamber or a DSSD) which can distinguish between the recoils and scattered beam events based on the observed energy.

The single number people most want to know in the discussion of a recoil mass spectrometer's performance is its efficiency for transmitting recoils. However, recoil transmission depends on too many factors external to the spectrometer design, such as the reaction kinematics (inverse, symmetric, or normal), the reaction channel (neutron, proton, or $\alpha$ evaporation), and the target thickness. Transmission efficiency is therefore *not* a good figure of merit to describe a device's performance. It only makes sense to talk about the transmission efficiency of a device in the context of a specific reaction channel from a specific reaction.

### Inverse Reactions

We now consider the special advantages and challenges offered by inverse reactions in the context of recoil mass spectrometers; this is an important issue for understanding the significant improvement offered by the HRIBF RMS.

An "inverse" reaction is one in which the nuclei of the beam ions are more massive than the nuclei in the target. We will refer to reactions where the beam ions are lighter than the target nuclei as having "normal kinematics". A "symmetric" reaction is one in which the beam ions have about the same mass as the target nuclei. The primary advantage of using inverse reactions with a recoil mass spectrometer is that collection efficiency for recoils from inverse reactions is much higher than for recoils from the corresponding normal reactions. This higher collection efficiency is particularly true for $\alpha$-particle evaporation channels. The improved recoil transmission comes about because the kinematic properties of the recoils from inverse reactions are better matched to the spectrometer acceptances than those of recoils from normal reactions; this phenomenon is referred to as "kinematic focusing".

Kinematic focusing results from the much higher energy of the recoils from inverse reactions; this higher energy arises not only from the much higher beam energy required to open the desired reaction

channel than for the corresponding normal reaction, but also because of the increased momentum transfered to the recoil from the more massive projectile. The higher recoil energy means that particle evaporation leads to a smaller spread in the recoil energies and angles. Thus, the recoils do not get knocked out of the spectrometer acceptance windows as easily. The higher recoil energy also means that multiple scattering in the target does not cause as much angular spread of the recoils. The higher recoil energy also results in a higher recoil charge state distribution which means that more charge states can fit into the fixed spectrometer $M/Q$ acceptance window. The smaller recoil energy spread allows a thicker target to be used in the reaction to increase the production yield while still matching the spectrometer energy acceptance window.

An example discussed in Reference [1] illustrates the dramatic increase in the count rate for an isotope observed at the focal plane anticipated from the use of inverse reactions. The example compares the production of $^{70}$Kr from the normal reaction $^{58}$Ni($^{16}$O,4$n$) at $E(^{16}\mathrm{O}) = 80$ MeV to that from the corresponding inverse reaction $^{16}$O($^{58}$Ni,4$n$) at $E(^{58}\mathrm{Ni}) = 290$ MeV. For a spectrometer with an angular acceptance of 10 msr, an energy acceptance of $\pm 10\%$, and an $M/Q$ acceptance of $\pm 5\%$, the $^{70}$Kr count rate will be nearly a factor of 500 greater for the inverse reaction (assuming the target thickness is increased so that the energy spread of the recoils due to the target thickness fills the energy acceptance of the device).

Another crucial advantage offered by inverse reactions is that energy loss detectors used for $Z$-identification of recoils at the focal plane work more effectively with the resulting high velocity recoils. In many cases, experiments that require such recoil $Z$-identification are only possible with an inverse reaction.

There is, of course, a price to pay for the dramatic advantages of using inverse reactions with recoil mass spectrometers. Inverse reactions are much more demanding on the performance of recoil mass spectrometers from the standpoint of beam rejection than are normal reactions. In inverse reactions, the kinematic properties of the recoils are much more similar to those of the beam particles entering the spectrometer than is the case for normal kinematic reactions. Thus the beam particles reach much farther into the spectrometer and the chance for significant amounts of these to scatter into the focal plane increases dramatically. The problem becomes more severe for more inverse reactions: the more negligible the mass of the target nucleus is compared to the mass of the projectile, the

more similar the kinematic properties of the recoils are to those of the beam particles.

As discussed earlier, in normal kinematic reactions, the location of the primary beam dump is on the anode plate just inside the entrance of the first electric dipole as shown in Figure 5. For inverse reactions the beam dump location shifts towards the exit of the first electric dipole; in more inverse reactions, the higher charge states of the beam even make it all the way through the first electric dipole. For beam charge states making it all the way past the first electric dipole to scatter instead off the anode of the second electric dipole, the role of the second dipole as a secondary dispersive element to stop scattered beam particles from reaching the focal plane is defeated. In the most extreme cases, charge states of the beam can fit directly into the spectrometer $M/Q$ acceptance window; the spectrometers discussed so far have no defense against this situation other than the use of selective, physical blocking of the affected parts of the focal plane.

## The HRIBF Recoil Mass Spectrometer

We now turn our attention to one recoil mass spectrometer in particular — the Recoil Mass Spectrometer (RMS) of the Holifield Radioactive Ion Beam Facility (HRIBF) at Oak Ridge National Laboratory. The quality that distinguishes the HRIBF RMS from its predecessors is its enhanced beam suppression capability. This capability makes the RMS well suited for use with inverse reactions where kinematic focusing leads to greater recoil transmission efficiency and is needed for use at a radioactive ion beam facility.

### Introduction

The RMS consists of two distinct optical components. In addition to the mass separator portion which makes use of the usual split electric dipole arrangement to provide $M/Q$ dispersion of the recoils, there is also a momentum achromat to provide enhanced beam suppression. The RMS is composed of 14 element: two electric dipoles (E1 and E2), three magnetic dipoles (D1 – D3), seven magnetic quadrupoles (Q1 – Q7), and two magnetic sextupoles (S1 and S2) arranged as shown in Figure 6. The flight path through the device from the target position to the focal plane where the recoils are dispersed according to $M/Q$ is 25 m. The recoil time-of-flight through the RMS varies depending on the reaction but is typically on the order of 2 $\mu$s. (The recoil time-of-flight for other

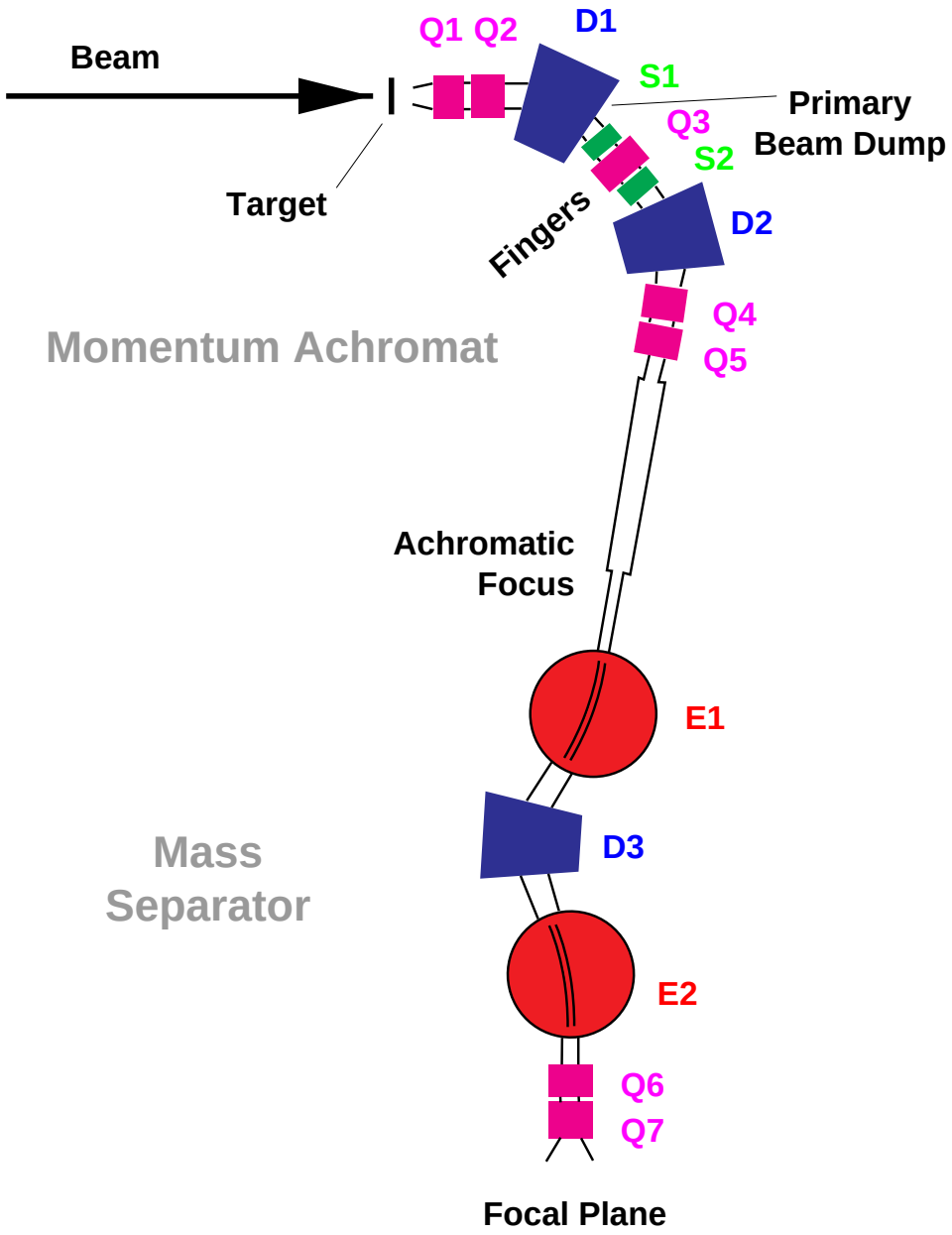


Figure 6: A schematic view of the HRIBF Recoil Mass Spectrometer. The beam enters the target shown at the top of the figure from the left. The recoils are dispersed according to their charge-to-mass ratio $M/Q$ at the focal plane. The device consists of two electric dipoles (E1 and E2), three magnetic dipoles (D1 – D3), seven magnetic quadrupoles (Q1 – Q7), and two magnetic sextupoles (S1 and S2).

recoil mass spectrometers is less because they have shorter flight paths.) The momentum achromat extends from the target position to the location labeled "achromatic focus" and includes elements Q1 through Q5. The mass separator extends from the achromatic focus to the focal plane and includes elements E1 through Q7.

The most striking physical difference between the RMS and other machines is the large size of the dipole elements in the mass separator. The large electric dipole radius of curvature (6 m) gives the RMS a much higher electrical rigidity than other machines without increasing the electric field needed for the dipoles. (The RMS can accommodate recoils with an electric rigidity up to 15 MeV/$Q$ compared to 9 MeV/$Q$ for the FMA.) This high rigidity is essential for use with inverse reactions — recoils from inverse reactions have a much higher energy and, hence, typically a much higher electrical rigidity than recoils produced in reactions employing normal kinematics. A consequence of the longer plates in the electric dipoles, however, is a smaller energy acceptance.

Details about the design and expected performance of the RMS are given in Reference [1]. The RMS is designed to have a large solid angle acceptance compared to its competitors. The calculated solid angle acceptance is 13 msr compared to 8 msr for the FMA. (All FMA information quoted here is from Reference [11].) The FMA value presumably gets worse with the use of the germanium array GAMMASPHERE because of the need to increase the distance between the target position and the FMA to accommodate GAMMASPHERE. The RMS value corresponds to an opening angle from the center of the beam spot of $\pm 30$ mrad ($\pm 1.7^\circ$) in the horizontal direction and $\pm 115$ mrad ($\pm 6.6^\circ$) in the vertical direction. The RMS is designed to accommodate a beam spot size of $\pm 0.25$ mm (horizontal) $\times$ $\pm 1.0$ mm (vertical). A ray tracing calculation (see Figure 15 in Reference [1]) suggests an energy acceptance for the RMS of $\pm 9\%$ FWHM dropping to zero transmission at $\pm 15\%$. (The energy acceptance quoted for the FMA is $\pm 20\%$.) The $M/Q$ acceptance for the RMS suggested by ray tracing calculations (see Figure 14 in Reference [1]) is somewhere in the range of $\pm 3$ to $\pm 4\%$. (The FMA $M/Q$ acceptance is quoted to be $\pm 7\%$; however, Figure 8 from Reference [11] suggests an $M/Q$ acceptance closer to $\pm 3.5\%$.) The mass resolution $M/\Delta M$ predicted for the RMS is as high as 1050. (The FMA mass resolution is 340.)

The size of the focal plane, as defined by the size of the position sensitive detector used to observe the recoil positions there, is 36 cm horizontally by 10 cm vertically. (The FMA focal plane is 15 cm

horizontally × 3 cm vertically.) RMS settings can be used to adjust the size, shape, and dispersion of the mass groups. A typical size (FWHM) for the mass groups as measured in the symmetric reaction of a $^{58}$Ni beam on a $^{60}$Ni target is 1 cm wide by 2 cm high. (See Figure 1; the scale is 2 channels/mm in both the horizontal and vertical directions.) The spacing between mass groups in this reaction was 3.5 cm, and the mass dispersion was 40 mm/%. (For the FMA the typical mass dispersion is 10 mm/%.)

One distinguishing feature of the RMS is the large distance of 75 cm between the target position and Q1 and the large image distance of 93 cm from Q7 to the focal plane position. These distances allow for the placement of GAMMASPHERE at either the target or the focal plane positions with minimal modifications to the array and allow for the array to be incorporated without needing to make changes that compromise the RMS performance. (The FMA has an original design value for the image distance of 30 cm — variable over ∼50 cm — and for the object distance of 30 cm [11].) The large RMS beam line height of 81 inches was also chosen to make it easy to couple GAMMASPHERE to the spectrometer.

## Beam Rejection

The momentum achromat gives the RMS significantly enhanced beam rejection compared to its predecessors. This section explains how this beam suppression is achieved.

In the momentum achromat the magnetic dipole D1 acts to create a focal plane in which particles leaving the target are dispersed by momentum; this focal plane is located inside quadrupole magnet Q3. (See Figure 6.) Dipole D2 is matched to counter the momentum dispersion induced by D1, thus creating an achromatic focus in front of the entrance to the mass separating section of the RMS. This achromatic focus can be thought of as a virtual target for the mass analyzer

The key to understanding how the momentum achromat provides beam rejection is to consider what happens at the Q3 focal plane. For normal kinematic reactions the Q3 focal plane is not important. In such reactions the primary beam dump location is inside of D1. This situation is much better than for other recoil mass spectrometers where the beam particles are stopped inside the first electric dipole corresponding to E1 of the RMS. (See Figure 5 and the discussion of beam rejection in normal split electric dipole mass separators beginning on page 16.) In the RMS the fact

that the beam dump is much farther away from the focal plane and is separated from it by a 90° bend makes it much more difficult for scattered beam events to reach the final focal plane.

For inverse reactions, the higher charge states of the beam have a low enough rigidity to exit D1 along with the recoils. Thus, they pass through the Q3 focal plane, and progress deep within the spectrometer (even into E2) before scattering. The RMS, therefore, can have the same problems with scattered beam reaching the final focal plane that other devices have. The Q3 focal plane, however, makes possible a strategy for stopping beam particles not available in other devices. This strategy even works for charge states from the most extreme inverse reactions which fit directly into the final focal plane $M/Q$ acceptance — charge states against which other machines have no defense other than placing collimators at the focal plane.

Because of the narrowly defined momentum of the beam particles originating from the tandem accelerator, charge states of the beam entering the RMS can be focused into very narrow vertical spots inside the Q3 focal plane. The recoils, on the other hand, leave the target with a wide spread in energy and mass as a consequence of the reactions that produce them; they thus do not have a well defined focus in the Q3 focal plane, but instead are distributed across it more-or-less uniformly. It is therefore possible to use thin metal rods, called "fingers", at the Q3 focal plane to intercept charge states of the beam while having a minimal impact on the transmission of the recoils through the spectrometer. The "virtual target" provided by the RMS momentum achromat to the mass analyzer thus has the advantage over the real target that the beam particles have already been eliminated.

### Use With Radioactive Ion Beams

The RMS was designed for use in a stable heavy ion beam facility with beams accelerated by two coupled accelerators: a tandem followed by a cyclotron. During the construction of the RMS the mission of the Holifield facility changed: its new role is to provide beams of radioactive rather than stable heavy ions. The order of the two accelerators has been reversed; the job of the cyclotron is to accelerate intense beams (up to 20 $\mu$A) of hydrogen or helium ions onto a thick target to generate radioactive nuclei which are then extracted and separated for acceleration by the tandem. This section discusses the advantages offered by using radioactive ion beams (RIBs) in fusion-evaporation reactions. It also shows how the features that make the RMS an excellent device for use with stable

heavy ion beam reactions also make it very well suited to meet the special challenges of dealing with recoils produced with RIBs.

There are two reasons behind the current interest in using radioactive ion beams to produce isotopes in fusion-evaporation reactions. The first is that RIBs make it possible to generate isotopes for study not available from reactions with stable beams and targets. The second reason is that the relative yield is typically much higher for isotopes far from stability in reactions from RIBs even though these isotopes may also be produced with stable beams; thus, RIBs provide much cleaner conditions for studying such isotopes.

Several major technical challenges arise from using RIBs that make it difficult to take advantage of the benefits they offer, however. One challenge is low beam intensity. Producing and separating short-lived isotopes for acceleration is currently a great technical challenge; we are just beginning to learn the many tricks needed to accomplish this task effectively. The beam intensity of $10^8$ particles/s currently within reach for RIBs is down by about three orders of magnitude from the stable beam intensities we have used with the RMS ($10^{11}$ particles/s $\approx$ 15 particle nA). Low beam intensity of course means a low yield of the isotopes produced in reactions from RIBs. So, even though the need to pull out weakly produced reaction products from a large background of other reaction channels may not be as great with RIB reactions, highly efficient and sensitive detection systems are still required to catch the events of interest even in the strongest reaction channels.

A second technical challenge is the background introduced into the experimental setup from decaying beam particles. Special care must be taken to prevent the presence of the RIB from crippling the target area detectors, and good beam rejection is critical to prevent beam particles from contaminating focal plane detector stations.

A third complication can arise with the use of RIBs if the beam is strongly contaminated with a stable isobar. In such instances the experimental setup must be capable of coping with and sorting out events from two sets of reaction products instead of just one.

A recoil mass spectrometer cannot tell and does not care whether the recoils it separates and the beam it rejects originate from stable or radioactive ions. The features that make the HRIBF RMS an excellent experimental environment to use with reactions originating from stable beams are even

more critical for experiments involving RIBs: superior beam rejection together with high sensitivity and selectivity.

# CHAPTER II

## ION OPTICS OF THE RMS

In the first chapter we explored the important role that recoil mass spectrometers play in the science of nuclear structure. We also began examining the HRIBF RMS in order to understand its capabilities compared to other mass separators. The purpose of this chapter is to provide a more detailed description of how the RMS works from the point of view of ion optics.

Designing and operating a device with fourteen elements which must work together and which are independently adjustable can be a daunting task. The only reasonable way to develop a full understanding of a device as complicated as the RMS and to optimize its performance is through detailed simulations by using ion-optical codes. It is not the intention of this section, however, to describe these efforts. The goal rather is to provide enough background for understanding how the fruits of such efforts came about. This section also provides the qualitative understanding of the device and a discussion of details necessary to bring it into operation.

### Notation

The motion of a particle through an ion-optical element is defined relative to a reference path called the optic axis. The optic axis through an electric or magnetic dipole is a circular arc defined by the radius of curvature of the dipole. For all other elements used in the RMS (magnetic quadrupoles and sextupoles), the optic axis is a straight line along the element's axis of symmetry. The components of the RMS are arranged so that if straight lines are used in the field free regions between the elements to join their optic axes, the optic axis of the RMS is a single smooth line in a horizontal plane.

Figure 7 illustrates how the position and trajectory of a particle in an ion-optical system can be represented in terms of the coordinates $x$, $y$, $z$, $\theta$, and $\phi$. The $z$-axis of the coordinate system is a horizontal line that lies along (or tangent to) the optic axis. Within any plane perpendicular to the optic axis, the position of a particle is described with respect to two axes: the $x$-axis is the horizontal line that passes through the optic axis, while the $y$-axis is the vertical line that passes

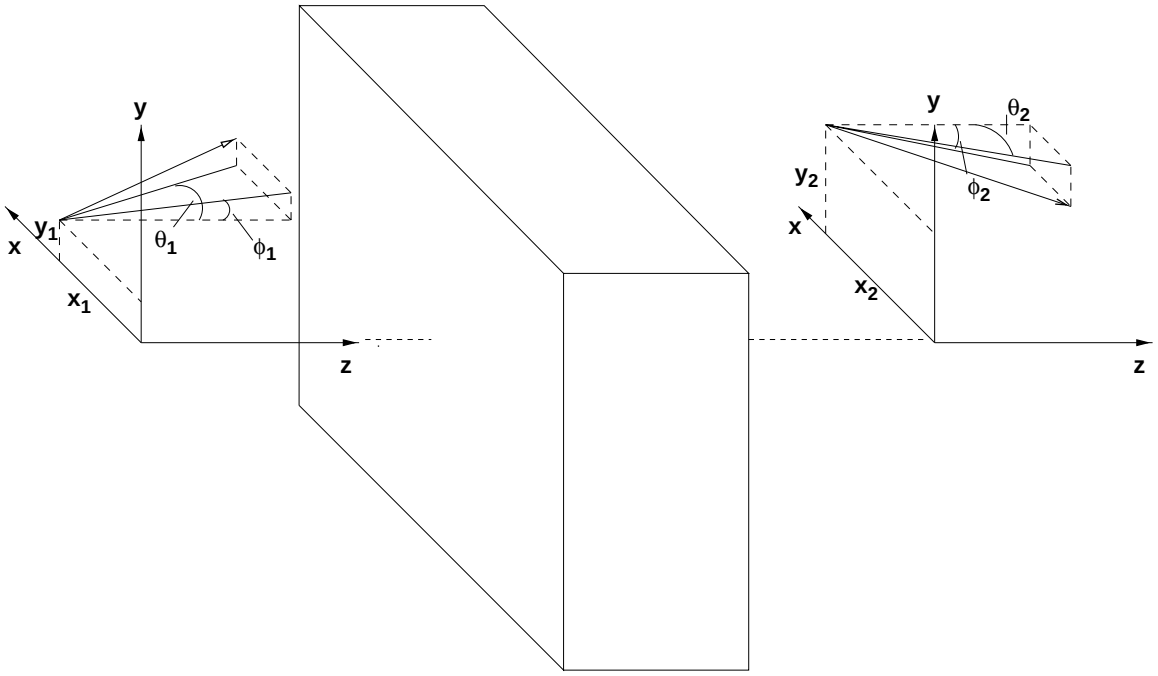


Figure 7: The coordinate system used to describe a particle trajectory. The figure illustrates the coordinates $(x_1, \theta_1, y_1, \phi_1)$ of an ion at some point before entering an ion-optical device and the coordinates $(x_2, \theta_2, y_2, \phi_2)$ at some point after leaving the device. The $z$-axis lies along the optic axis of the device.

through the optic axis. A particle's location in the system is thus defined in terms of its position $z$ along the optic axis and in terms of its distances $x$ and $y$ away from the optic axis. The particle's direction of motion at any point is given in terms of the angle $\theta$ its trajectory makes with respect to the $yz$ (vertical) plane and the angle $\phi$ with respect to the $xz$ (horizontal) plane. Figure 7 shows an example of the coordinates $(x_1, \theta_1, y_1, \phi_1)$ of a particle entering an ion-optical device and the coordinates $(x_2, \theta_2, y_2, \phi_2)$ of the particle leaving the device.

The field settings of the RMS elements are determined with reference to a "central ion" having some particular energy $E_0$, charge state $Q_0$, and mass $M_0$ which enters the RMS along the optic axis ($x_0 = y_0 = z_0 = \theta_0 = \phi_0 = 0$). The energy of an arbitrary ion is specified in terms of the central energy $E_0$ by using the fractional value $\delta E$. The mass-to-charge ratio of an arbitrary ion is specified in terms of the central value $M_0/Q_0$ by using the fractional value $\delta m$. The electric and magnetic field settings needed for the RMS elements are determined by requiring that the trajectory of the central ion follows the optic axis.

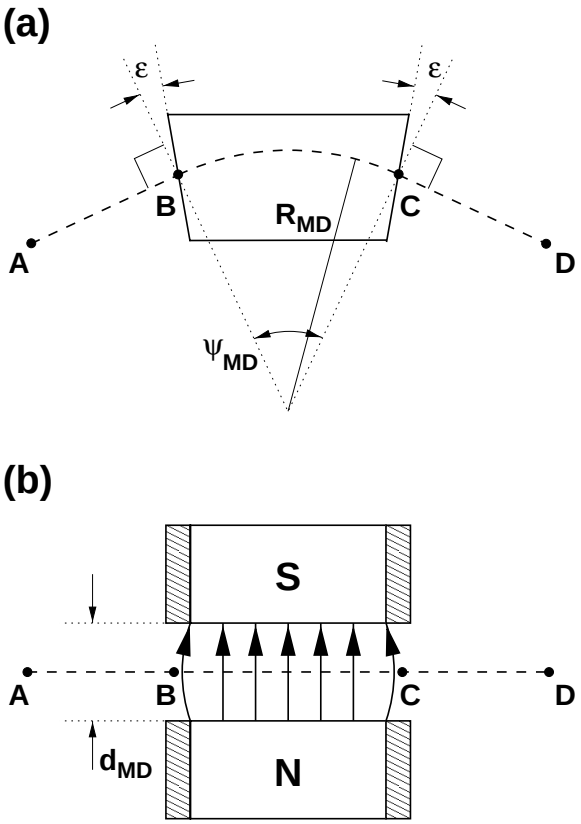


Figure 8: Schematic diagram of a magnetic dipole showing (a) top view and (b) side view. Within the magnet the optic axis lies along the circular arc $BC$ defined by the magnet's deflection angle $\psi_{\mathrm{MD}}$ and radius of curvature $R_{\mathrm{MD}}$. In the field-free regions at the entrance and exit of the dipole, the optic axis lies along the straight line segments $AB$ and $CD$. The entrance and exit shim angles $\varepsilon$ provide vertical focusing to enhance transmission of ions through the dipole.

## RMS Components and How They are Scaled

This section provides an introduction to the different ion-optical components used within the RMS: magnetic dipoles, electric dipoles, magnetic quadrupoles, and magnetic sextupoles. It also gives a derivation of the simple relations used to calculate and scale the fields of these components.

### Magnetic Dipoles

As illustrated in Figure 8 the deflection angle $\psi_{\mathrm{MD}}$ and the radius of curvature $R_{\mathrm{MD}}$ define the dimensions of a magnetic dipole. In the field-free regions at the entrance and exit of the dipole, the optic axis lies along the straight line segments $AB$ and $CD$, while within the dipole it follows the circular arc $BC$. Another important design parameter of a magnetic dipole is the vertical separation $d_{\mathrm{MD}}$ between the poles. A larger gap makes it easier to get ions through the magnet, but also requires

more current to produce a given field. It is possible to create a vertical focusing effect which enhances the transmission of ions through the dipole by rotating the field boundary by an angle $\varepsilon$ about the vertical line passing through the optic axis at the entrance and exit of the dipole. The presence of this shim angle introduces a horizontal component in the fringing field which acts to create a component of force directed towards the central horizontal plane for particles above and below the central plane. The three RMS magnetic dipoles all deflect particles in the horizontal plane and are all designed to the same specifications. They each have a deflection angle of 50.0°, a 1.400 m radius of curvature, and entrance and exit shim angles of 15.0°.

For a magnetic dipole the correct field setting $B$ is the one which causes a central ion entering the magnet to follow the circular optic axis as it passes through the element. Within the dipole, the velocity $v_0$ of the central ion is directed perpendicular to the magnetic field. Thus, by equating the centripetal force (arising from the interaction of the magnetic field on the moving ion) to the centrifugal force, we have

$$Q_0 v_0 B = \frac{M_0 v_0^2}{R_{\mathrm{MD}}} \,. \tag{1}$$

Hence,

$$B = \frac{M_0 v_0}{Q_0 R_{\mathrm{MD}}} = \frac{p_0}{Q_0 R_{\mathrm{MD}}} = \frac{\sqrt{2 M_0 E_0}}{Q_0 R_{\mathrm{MD}}} \tag{2}$$

where $p_0$ is the momentum of the central ion. Once the field value is determined for some particular central ion, the field needed for any other central ion value can be determined simply by scaling according to Equation 2:

$$B \propto \frac{p_0}{Q_0} \propto \frac{\sqrt{M_0 E_0}}{Q_0} \,. \tag{3}$$

Note that the magnetic dipole field equations have been derived by assuming non-relativistic dynamics. At the beam and recoil energies in use with the RMS, it is not necessary to worry about relativistic corrections.

For particles entering a dipole along the optic axis with the same charge state $Q = Q_0$ as the central ion, but with a momentum $p > p_0$, it is clear from Equation 2 that the field $B$ will be too weak to deflect the particles enough to follow the optic axis. Similarly, the field $B$ will be too strong and hence provide too much deflection for particles with a momentum $p < p_0$. Thus a magnetic dipole disperses ions of a given charge state according to their momentum $p$, or more generally it

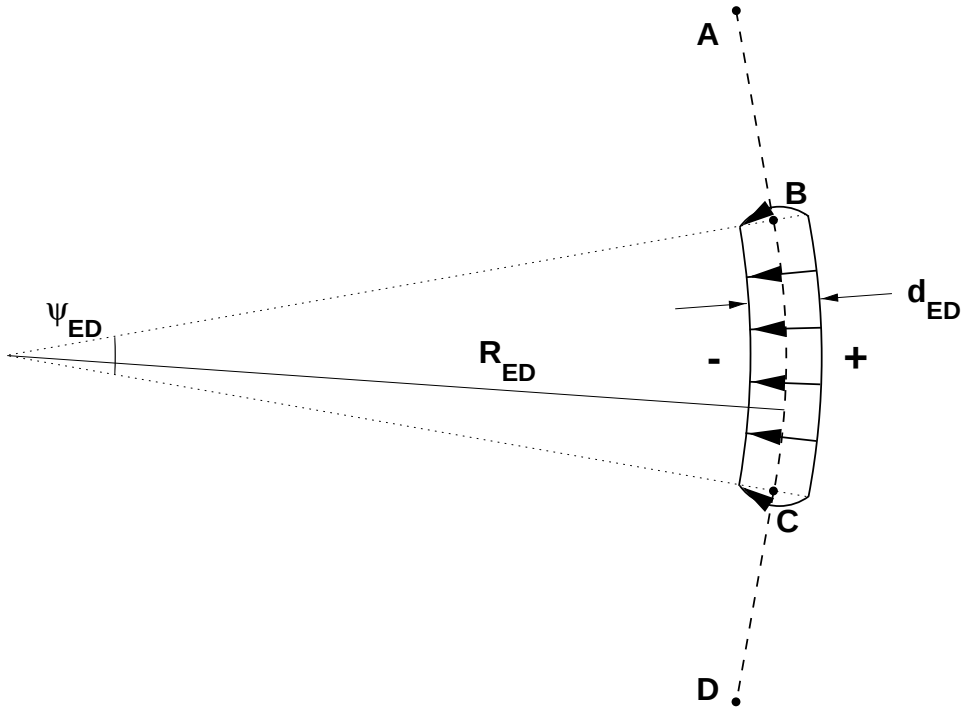


Figure 9: Top view of an electric dipole showing the radius of curvature $R_{\mathrm{ED}}$, the deflection angle $\psi_{\mathrm{ED}}$, and the gap between the electrodes $d_{\mathrm{ED}}$. Within the dipole the optic axis lies along the circular arc $BC$, while in the field-free regions at the entrance and exit, the optic axis lies along the straight line segments $AB$ and $CD$.

disperses ions according to their momentum-to-charge ratio $p/Q$.

The ions entering an ion-optical system can be described in terms of their response to magnetic fields by using a quantity called the magnetic rigidity $k_M$. This quantity is defined as:

$$k_M = \frac{ME}{Q^2} \, . \tag{4}$$

It is of course possible for ions with different values of $M$, $E$, and $Q$ to have the same magnetic rigidity value. As Equation 2 shows, such particles entering a magnetic dipole along the same trajectory will follow the same path through the dipole.

## Electric Dipoles

An electric dipole consists of two parallel electrodes bent along cylindrical surfaces as shown in Figure 9. The radius of curvature $R_{\mathrm{ED}}$, the deflection angle $\psi_{\mathrm{ED}}$, and the gap $d_{\mathrm{ED}}$ between the electrodes define the dimensions of an electric dipole. In the field-free regions at the entrance and exit of the dipole, the optic axis lies along the straight line segments $AB$ and $CD$, while within the dipole it follows the circular arc $BC$. Unlike in a Wien filter, where the deflection of the central ions

from the electric field is counter-balanced by a crossed magnetic field, the electrodes of an electric dipole must be curved instead of flat to keep the central ions moving along a path perpendicular to the electric field lines. The two RMS electric dipoles are both designed to the same specifications: a deflection angle of 20.0°, a 6.000 m radius of curvature, and an electrode gap of 10.0 cm. They deflect ions in the horizontal plane.

For an electric dipole the correct field setting $\mathcal{E}$ is the one which causes a central ion entering the dipole to follow the circular optic axis as it passes through the element. Thus, by equating the centripetal force (arising from the interaction of the electric field on the moving ion) to the centrifugal force, we have

$$Q_0\mathcal{E} = \frac{M_0 v_0^2}{R_{\mathrm{ED}}} \,. \tag{5}$$

Hence,

$$\mathcal{E} = \frac{2E_0}{Q_0 R_{\mathrm{ED}}} \,. \tag{6}$$

Once the dipole fields are determined for some particular central ion, they can be determined for any other central ion value simply by scaling according to Equation 6:

$$\mathcal{E} \propto \frac{E_0}{Q_0} \,. \tag{7}$$

Again it is not necessary to worry about relativistic corrections.

For particles entering an electric dipole along the optic axis with the same charge state $Q = Q_0$ as the central ion, but with an energy $E > E_0$, it is clear from Equation 6 that the field $\mathcal{E}$ will not be strong enough to keep the particles following the optic axis. Similarly, the field $\mathcal{E}$ will be too strong and hence provide too much deflection for particles with an energy $E < E_0$. Thus an electric dipole disperses ions of a given charge state according to their energy $E$, or more generally it disperses ions according to their energy-to-charge ratio $E/Q$.

The ions entering an ion-optical system can be described in terms of their response to electric fields by using a quantity called the electric rigidity $k_E$. This quantity is defined as:

$$k_E = \frac{E}{Q} \,. \tag{8}$$

It is of course possible for ions with different values of $E$, and $Q$ to have the same electric rigidity

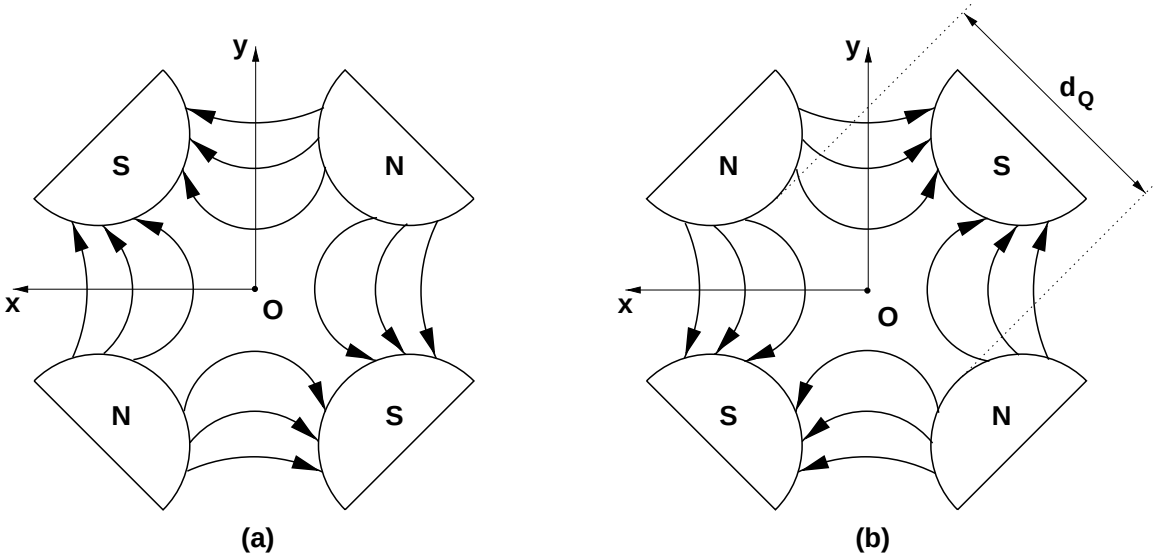


Figure 10: Side view of (a) an $x$-focusing magnetic quadrupole and (b) a $y$-focusing quadrupole. The optic axis is directed into the page at point $O$.

value. As Equation 6 shows, such particles entering an electric dipole along the same trajectory will follow the same path through the dipole.

### Magnetic Quadrupoles

Figure 10 shows side views of a magnetic quadrupole energized to provide $x$-focusing (a) and $y$-focusing (b). The optic axis is a straight line perpendicular to the plane of the figure and is directed into the page at point $O$. The important physical dimensions defining the properties of a quadrupole are the distance between the poles (also called the bore diameter) $d_Q$ — see Figure 10(b) — and the effective length of the quadrupole along the optic axis $L_Q$. For a given current setting, a quadrupole has a weaker field near the optic axis (dropping to zero at the optic axis) and a stronger field in the horizontal and vertical directions away from the optic axis. As can be seen from the fields shown in Figure 10(a) by applying the right-hand force rule for charged particles moving in a magnetic field, particles entering in the horizontal plane containing the optic axis ($y = 0$) experience a force directed towards the optic axis. Charged particles entering this quadrupole in the vertical plane containing the optic axis ($x = 0$) experience a force directed away from the optic axis. Similar arguments show why a quadrupole energized as shown in Figure 10(b) provides focusing in $y$ and defocusing in $x$. Two or more quadrupoles that are alternately $x$- and $y$- focusing must be used in sequence to create

a net focusing in both the $x$- and $y$- directions. The particles that are defocused in one quadrupole are directed into a region of higher field in the next quadrupole and, hence, experience a stronger focusing force that over-compensates the defocusing effect of the first quadrupole.

The RMS employs quadrupole doublets to provide focusing. The three doublets contain the element pairs Q1–Q2, Q4–Q5, and Q6–Q7. Quadrupoles Q2, Q3, Q4, and Q6 are $x$-focusing and Q1, Q5, and Q7 are $y$-focusing in the original RMS design. All quadrupoles have a bore diameter $d_Q$ of 20.32 cm. Elements Q1, Q5, and Q6 have an effective length $L_Q$ of 45.72 cm while Q2, Q3, Q4, and Q7 have an effective length of 60.96 cm. The poles of Q3 are split into two parts along the axial direction which are energized by a single set of coils. The 10 cm gap provides access to the focal plane in the center of the magnet for placing the finger system.

Because the field at the optic axis of a magnetic quadrupole is zero independent of the setting of the current, the strategy of using the influence of the field on the trajectory of central ions does not provide a way of determining the proper field setting for quadrupoles as it does for dipoles. Instead, the proper quadrupole field setting for a given central ion value must be determined from modeling codes and from experimental observations based on the optimization of various focusing conditions and the minimization of aberrations. However, once these fields are determined by meeting some set of criteria for a given central ion value, the corresponding fields required to meet the same set of criteria for any other central ion value are obtained simply by scaling according to the same relation 3 used for setting the magnetic dipoles.

### Magnetic Sextupoles

The six poles of a magnetic sextupole are arranged as shown in the side view given in Figure 11. The three shaded poles are energized to have a polarity opposite to that of the unshaded poles. The optic axis is a straight line passing into the page at point $O$ through the center of the device and perpendicular to the plane of the figure. Since sextupoles are used to correct aberrations of second order (see the discussion below), there is no simple way to conceptualize how they work. The two RMS sextupoles have a bore diameter of 20.32 cm and an effective length of 30.00 cm; they are energized with the same polarity. As with the quadrupoles, the proper field settings for the sextupoles for a given central ion value are obtained by using optical modeling codes and

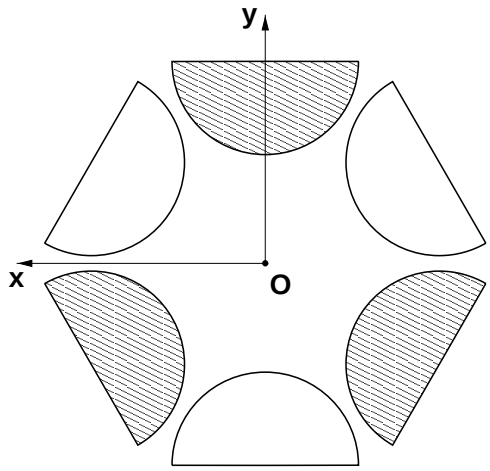


Figure 11: Side view of a magnetic sextupole. The optic axis is a straight line perpendicular to the plane of the figure passing through the device at point $O$. Adjacent poles are energized to have opposite polarity as indicated by the shading in the figure.

experimental observations. Once the proper sextupole field setting is found for a given central ion setting, the proper field setting corresponding to any other central ion setting is found simply by scaling the fields according to relation 3.

## Modeling the RMS

The discussion up to now has only considered the effect of idealized ion-optical elements on central ions. Life quickly becomes complicated even for ions entering a device along the optic axis but with $M \neq M_0$, $E \neq E_0$, or $Q \neq Q_0$ or for ions that have the central mass, energy, and charge but which do not follow the optic axis. Most ions passing through a recoil mass spectrometer, of course, not only enter not along the optic axis but they also differ in mass, charge, and/or energy from the central ion. The only reasonable way to design an ion-optical device as complicated as the RMS and to optimize its performance is in terms of an understanding of the device achieved by using models provided by computer codes. The present discussion on how devices such as the RMS are modeled also provides a further introduction to the language used to describe ion-optical systems.

The heart of any ion-optical code is how the different kinds of elements are modeled. A complication present for each of the RMS elements is the existence of fringing fields at the entrance and exit

of the element. Ion-optical codes generally treat these fringing fields by using some sort of approximation. One approach for handling fringing fields is the construct of an effective field boundary. An effective field boundary is an imaginary boundary at which the field rises discontinuously from zero on the side away from the element to the full field value inside the element. The position of the effective field boundary is chosen so that the effect of the resulting idealized element is equivalent to the effect of the actual element with its fringing field. Field clamps, also called fringing field shunts, can be used to help define the position of the effective field boundary, as well as to make the fringing field drop off more sharply away from the element so that the fringing fields are not as vulnerable to distortion from the presence of nearby magnetic or conducting surfaces. Field clamps are positioned around the element entrance and exit and consist of pieces of iron for magnetic elements and of conducting surfaces for electric dipoles. Only the electric dipoles in the RMS employ field clamps.

In addition to providing for the usual ion-optical elements such as dipoles and quadrupoles, ion-optical codes make use of a "drift region" element to represent the field-free regions between elements. An inherent limitation of any modeling approach is the ability to simulate in terms of an idealized model real ion-optical elements with their manufacturing or alignment imperfections. This section discusses two approaches commonly used to model ion-optical systems.

One approach uses matrices to represent ion-optical elements and vectors to represent the trajectories and physical properties of ions at an element's entrance and exit. Reference [26] provides a thorough discussion of this approach. The action of a series of elements on a particle trajectory is simply given by the result of a matrix multiplication.

This approach can be illustrated by using a very simple idealized example. Consider a hypothetical ion-optical device whose only function is to operate on the horizontal trajectory of a particle described by the variables $x$ and $\theta$. The trajectory of the particle $\begin{pmatrix} x_2 \\ \theta_2 \end{pmatrix}$ as it leaves the device will be given in terms of the trajectory $\begin{pmatrix} x_1 \\ \theta_1 \end{pmatrix}$ it has entering the device by

$$\begin{pmatrix} x_2 \\ \theta_2 \end{pmatrix} = \begin{pmatrix} (x/x) & (x/\theta) \\ (x/\theta) & (\theta/\theta) \end{pmatrix} \begin{pmatrix} x_1 \\ \theta_1 \end{pmatrix} . \tag{9}$$

where the $2 \times 2$ matrix represents the device. From this matrix equation, the position $x_2$ of a particle

leaving the system is given as

$$x_2 = (x/x)x_1 + (x/\theta)\theta_1 \tag{10}$$

The condition for a spatial focus here is that the matrix element $(x/\theta) = 0$; as Equation 10 states, this condition ensures that the final position $x_2$ is only a function of the initial position $x_1$ and not of the initial angle $\theta_1$. The matrix element $(x/x)$ here gives the image magnification produced by the device represented by the matrix. If $|(x/x)| < 1$, then the image will be smaller than the object. If $|(x/x)| > 1$, then the image will be larger than the object. If $(x/x) < 0$, the image will be inverted.

The vectors and matrices used to represent the particle trajectories and elements in a real device such as a recoil mass spectrometer will, of course, have many more terms. These terms include ones such as $(x/\delta m)$ and $(\theta/\delta E)$ that take into account the fact that recoils have a spread in mass, charge, and energy about the central values $M_0$, $Q_0$, and $E_0$. The condition for a horizontal spatial focus in a recoil mass spectrometer is $(x/\theta) = (x/\phi) = 0$, and the condition describing the fact that the recoils are not dispersed horizontally according to energy is $(x/\delta E) = (\theta/\delta E) = 0$. The mass dispersion along the horizontal axis is given by the term $(x/\delta m)$. The matrices representing the ion-optical devices in a mass spectrometer can be simplified by using the fact that the fields are symmetric about the horizontal plane and the fact that the devices are non-accelerating.

The terms in the matrices representing ion-optical elements are referred to as *aberrations*. In the design phase of an ion-optical system a wide range of options is available for controlling the values of the aberrations. These options include the types of elements used in the system, how they are arranged, and their physical dimensions. Once an ion-optical system is in place, however, the options for adjusting the aberrations are limited to changes in the field settings of the elements.

A limitation of using matrices to represent ion-optical elements is that the matrices are based on mathematical approximations; the way to include higher order terms of the approximation is to include them explicitly as terms in the vector representing the particle trajectory and in the matrices representing the elements. Typical higher order terms affecting mass resolution in a recoil mass spectrometer are $(x/\theta\delta E)$ (a second order term) and $(x/\theta\phi^2)$ (a third order term).

Another approach generally taken to model the trajectory of an ion through the system is to calculate the trajectory point-by-point in terms of the forces experienced by the ion as it passes

through the system. In this approach, called ray tracing, an ion-optical device is modeled simply in terms of the magnetic or electric field it produces. A particle ends up where the forces direct it based on its initial trajectory; one can calculate any aberrations from the system's effect on a set of particles with some standard initial trajectories.

The RMS was designed and has been implemented with the help of both a matrix code and a ray tracing code. The matrix code GIOS [27] was used not only to work out the initial general RMS design, but also to help calibrate and optimize the settings of the magnetic quadrupoles and sextupoles. The ray tracing code RAYTRACE [28] was used to finalize the RMS design as well as to calculate its expected performance. The notation given here to define aberrations and particle trajectories follows the RAYTRACE conventions.

## A Qualitative View of the RMS Optics

Although the results of detailed optics calculations are an absolutely essential part of the design and implementation of a system as complex as the RMS, a qualitative insight into the ion-optics is just as crucial for understanding the system and making it work. A qualitative view not only provides a context to motivate and guide the ion-optical modeling, but this view also gives a perspective which protects against getting lost in the details of these calculations and which gives a way to link the results back to the real device. This section attempts to establish a general insight into the RMS ion optics by discussing three topics: (1) the role played by groups of elements within the system and how they work together to achieve the overall design objective; (2) the factors which affect the positioning of mass groups at the focal plane; and (3) how to anticipate the presence of scattered beam particles at the focal plane.

### Element Functions

The function of the E1–D3–E2 mass separator arrangement, the heart of the RMS, has already been described in the discussion of Figure 5 which begins on page 17. A general overview of the function of the momentum achromat portion of the RMS was given in the section describing the RMS beam rejection which begins on page 28.

The Q1–Q2 doublet controls how recoils from the target are collected. These magnets determine

the horizontal focus of the beam charge states at the finger focal plane in the center of Q3. The vertical role of this doublet is to optimize the recoil transmission through the momentum achromat by allowing as many recoils as possible to make it through the narrow 11 cm vertical gaps in D1 and D2.

The dipole D1 provides dispersion in $p/Q$ that separates the beam charge states in the finger focal plane. The dipole D2 counters the $p/Q$ dispersion of D1 to create the achromatic focus in front of E1. The quadrupole Q3 provides energy matching of the recoils reaching the achromatic focus. This magnet is the least critical component of the RMS; the RMS can still function even with Q3 turned off. The setting of Q3 does affect the vertical transmission through the momentum achromat portion of the RMS. (See Report #2, August 7, 1995, from Reference [29].)

The Q4–Q5 doublet determines the horizontal focus in the final focal plane — that is, the overall RMS resolution; this focus is set by allowing the position of the achromatic focus to vary along the drift region between Q5 and E1. The vertical task of this doublet is to optimize the transmission through the mass separator section of the RMS by fitting recoils through the aperture created by the 11 cm vertical gap in D3. The setting of this pair has a minimal impact on other RMS properties such as the $M/Q$ acceptance and second order aberrations.

The Q6–Q7 doublet controls the dispersion of the recoils leaving the mass separator. This doublet also controls the vertical spread of recoils entering the focal plane and subsequent detectors.

The magnetic sextupoles S1 and S2 are for eliminating the second order kinematic aberrations $(x/\delta E\delta E)$ and $(x/\theta\delta E)$ that affect mass resolution. There is no easy way to conceptualize how they are used since they each couple to several aberration coefficients. The sextupoles are absolutely essential to maintaining reasonable mass resolution.

### Position of Mass Groups at Focal Plane

Figure 1 is a good example of how the RMS separates recoils into groups by $M/Q$ as observed at the focal plane. The figure shows the focal plane as viewed looking downstream from Q7 — that is, from the point of view that the ions have before entering the focal plane. In terms of the coordinate system presented in Figure 7, the $x$-axis is directed to the left, the $y$-axis is pointing up, and the $z$-axis is directed into the plane of the figure. These same conventions for "left," "right," "up," and

"down" will be used when discussing the ion distribution at any other point along the RMS optic axis. The gap in the figure is an artifact of how the data from the two electrically isolated halves of the position sensitive detector used at the focal plane are displayed; it does not represent an area of the focal plane not seen by the detector. The focal plane detector is aligned so that the split at its center between the electrically isolated halves coincides with the optic axis. Note that the horizontal axis of the recoil distribution in the focal plane corresponds to $M/Q$: the mass for a given recoil charge state increases towards the right while the charge for a given recoil mass increases to the left. This section discusses three ways of affecting the position of the recoils groups at the focal plane.

One way to move the mass groups in the focal plane is by changing the central recoil specification for the mass $M_0$ or the charge $Q_0$. Increasing $M_0$ will bring a higher mass to the center of the focal plane, thus shifting the mass groups to the *left*. Increasing $Q_0$ will bring a higher charge to the center of the focal plane, thus shifting the mass groups to the *right*. (As the masses shift left or right, mass groups will disappear from one side of the focal plane because they fall out of the RMS $M/Q$ acceptance range while other mass groups will appear on the other side of the focal plane.) Fractional changes in the values for $M_0$ and $Q_0$ are possible since the magnetic and electric fields can be varied continuously, even though ions with, for example, a fractional charge state do not exist. Changing the central ion energy setting $E_0$ does not affect the position of the recoils at the focal plane since the RMS separates the recoils that enter it independently of their energies. Shifting masses by making fractional changes to the $Q_0$ setting is the method typically used during experiments to direct a particular mass group onto a specific region of the focal plane — for example onto a detector or around baffles used to keep masses not of interest from entering the detectors. No shifting of the recoils up or down in the focal plane is possible by changing the element field settings because all of the dipoles in the RMS bend ions in the horizontal plane and all of the remaining elements (assuming that they are aligned properly) are focusing, not bending, devices.

Another way to shift the position of the mass groups at the focal plane is by moving the position of the beam at the target. Table 1 shows the effect that horizontal or vertical changes in the beam position have on the position of the recoils. The horizontal shift at the focal plane that can be obtained from a horizontal shift in the beam position at the target is small. Typically, if the beam is moved enough to shift the masses by more than about half the spacing between adjacent mass groups

Table 1: Observed effect on ion position at RMS focal plane from shift of beam position at target. Although the position of the peak from the projection of recoil positions onto the focal plane vertical axis does not shift in response to a vertical shift in beam position, a shift in the symmetry of the shoulders of this peak is observable.

| Beam Position Shift at Target | Ion Position Shift at Final Focal Plane |
|---|---|
| ↑ | ↑ (shoulders) |
| → | → |

of a charge state, it will hit the target holder frame and cause a large amount of scattered beam particles to enter the focal plane. Figure 12 shows that a vertical shift in beam position does not so much affect the center of the vertical distribution of recoils observed at the focal plane as it does the shoulders of the distribution. Changing the location of the beam at the target is not a reasonable way to position the recoils at the focal plane in a real experiment; instead, the distribution of recoils at the focal plane can be used as a diagnostic tool to help decide if the beam is hitting the target on axis.

Another way to change the horizontal position of recoil groups at the final focal plane (or at the two intermediate focal planes) is by varying the fields of individual dipoles. This is only ever done as an exercise to help calibrate the dipole fields. The effect of changing each of the five dipole fields on the position of recoils at each of the focal planes is summarized in Table 2.

### Anticipating the Presence of Scattered Beam in the Focal Plane

This section discusses two approaches useful for understanding the presence of scattered beam in the RMS focal plane. One approach is to look for charge states of the beam that give rise to $M/Q$ values that fit directly into the RMS $M/Q$ acceptance. For example, in one run a 100 MeV beam of $^{32}$S was used with a 400 $\mu$g/cm$^2$ $^{29}$Si target. The RMS was scaled to $M_0 = 56.94$ (for $^{57}$Co), $Q_0 = 16^+$, and $E_0 = 44.6$ MeV. The only charge state of the beam that gives rise to an $M/Q$ value in the range from 3.38 to 3.74 ($\pm 5\%$ around the central ion value of 3.56) is $9^+$ with $M/Q = 3.56$. Indeed, use of the ionization chamber revealed the presence of low energy events at the same focal plane position as the $16^+$ $^{57}$Co recoils (also with $M/Q = 3.56$). Since the charge state of the beam

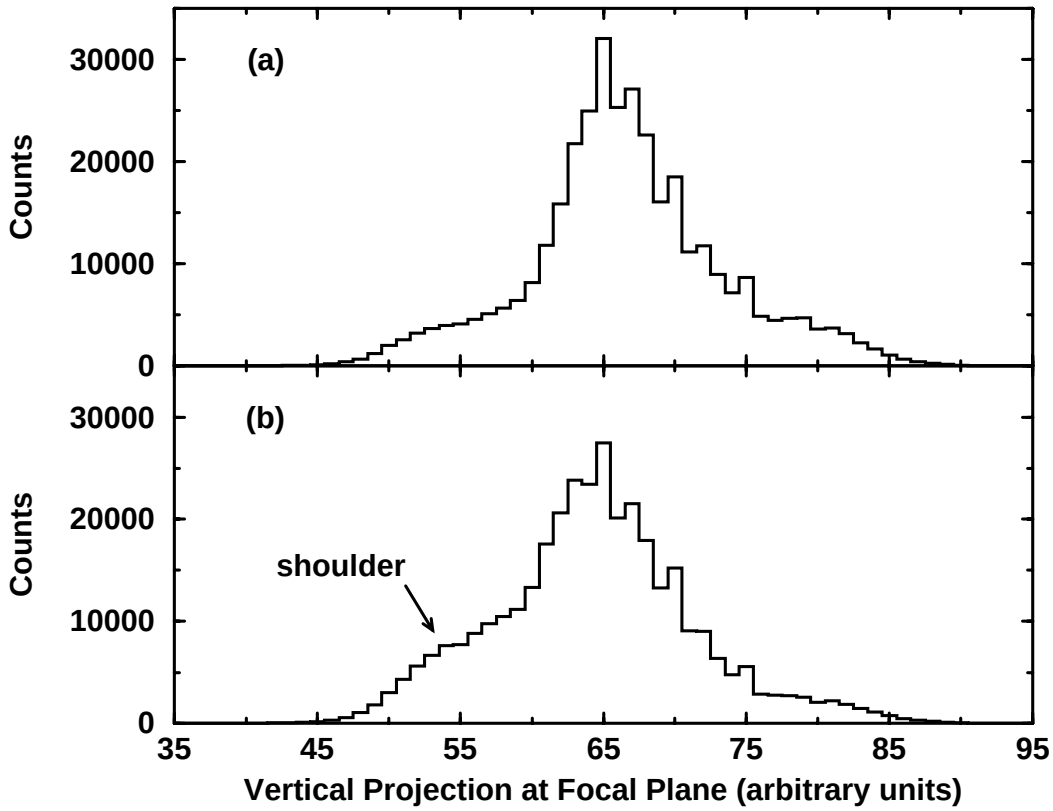


Figure 12: Vertical projections of events observed at the focal plane (a) with the beam properly positioned on the target and (b) with the beam positioned too low. Although the central peak of the projection does not shift for the two cases, an asymmetric shoulder appears on the low side of the distribution in (b) as a result of the incorrect positioning of the beam. This data is from the same reaction used in Figure 2.

Table 2: Observed effect of changes in dipole fields on the position of ions observed in the three RMS focal planes. The focal planes not affected by a dipole (because the dipole is down stream from the focal plane) are marked by "×".

| | Ion Position Shift in Response to Increasing Dipole Field | | |
|---|---|---|---|
| Element | Q3 Finger Focal Plane | Achromatic Focal Plane | Final Focal Plane |
| D1 | → | ← | → |
| D2 | × | → | ← |
| E1 | × | × | → |
| D3 | × | × | ← |
| E2 | × | × | → |

entering the target was $5^+$, these $9^+$ events arose from beam particles that lost four electrons in the target. The reason that these beam particles did not completely flood the focal plane is because their energy ($\sim$94 MeV after exiting the target) was so far outside the nominal RMS energy acceptance of $\pm$10% that only a small fraction of them had the right trajectory to make it through the RMS. These beam particles showed up in the ionization chamber as having *less* energy than the recoils because the gas pressure in the ionization chamber was optimized for the recoils and thus was not high enough to stop the beam particles and absorb their full energy.

Another approach that can be used to anticipate the presence of beam at the focal plane involves estimating which beam charge states can make it far enough into the RMS to scatter off the plates of the electric dipoles. Since all the elements leading up to E1 are magnetic, a range in magnetic rigidity $k_M = \frac{ME}{Q^2}$ (see Equation 4) can be used to determine the beam charge states reaching this far into the system. A reasonable range for the acceptance of ions in terms of $k_M$ is taken to be $\pm$10%; this value is consistent with the $\pm$10% RMS energy acceptance (which happens to be limited by the gap of the electric dipoles) or to a $\pm$20% energy acceptance for the magnetic elements (since the magnetic elements scale according to $(k_M)^2$ — see Equations 3 and 4). In the example just discussed, the resulting range in $k_M$ is from 16.6 to 18.3. By this criterion no beam charge states will make it into the electric dipoles to scatter: the only two charge states for $^{32}$S within this $k_M$ range, $17^+$ and $18^+$, do not exist. For other cases in which the beam charge states do make it into the electric dipoles, it is not possible to determine where scattered particles will end up in the focal plane because the process is so unpredictable.

## Implementation

Two features of the RMS control system make it possible to take advantage of ion-optical simulations to optimize the performance of the spectrometer without requiring any detailed knowledge about the simulations: knobs and modes. This section describes these features and discusses how they are implemented.

Table 3: Summary of the knobs available for adjusting the RMS. Elements which are weakly affected by a knob setting are listed in parentheses.

| Knob # | Knob Function | Affected Elements |
|---|---|---|
| 1 | mass resolution | Q4, Q5 |
| 2 | vertical transmission through momentum achromat | Q1, Q2 |
| 3 | second order correction ($x/\theta\delta E$) | S1, S2 |
| 4 | second order correction ($x/\delta E\delta E$) | S1, S2 |
| 5 | target-Q1 distance | Q1, Q2 |
| 6 | mass dispersion ($x/\delta m$) | Q6, Q7, (Q4), (Q5) |
| 7 | vertical focus | Q6, Q7, (Q4), (Q5) |
| 8 | vertical transmission through mass separator | Q4, Q5, Q6, Q7 |

## Knobs

Perhaps the most critical link between the detailed understanding of the RMS that comes from simulations made by using ion-optical codes and the day-to-day operation of the RMS is the control system feature called "knobs". A knob is a mechanism through which it is possible to perform a minor adjustment or optimization of the RMS without requiring expertise in ion-optics or the running of an ion-optical modeling code to figure out how to make the adjustment. Knobs are used (1) to calibrate the magnetic quadrupoles and sextupoles and (2) to optimize the RMS operation on a day-to-day basis to match the changing needs from experiment to experiment.

Table 3 lists the currently available knobs and their functions. Each knob is designed to affect a separate observable of the RMS performance. In general, different subsets of the 14 RMS elements affect different observables. For example, the Q1–Q2 doublet determines the vertical transmission of recoils through the momentum achromat section of the RMS (knob 2), while the Q4–Q5 doublet determines the vertical transmission of recoils through the mass separator section (knob 8). The elements affected by each knob are also listed in Table 3. The knobs, which are sometimes referred to as "vectors", are designed to be for the most part non-interfering. It is thus possible to optimize one observable by adjusting the associated knob without significantly affecting other aspects of the RMS performance.

The knobs for the RMS were designed by Arthur James (see Reports #2, August 7, 1995, #3, August 6, 1996, #6, August 28, 1996, and #7, September 2, 1996 of Reference [29]) by using the

matrix code GIOS [27]. Aberrations of third order and higher were ignored in creating the knobs since no elements in the RMS design provide for control over such effects. The RMS control system implements knobs through user specified settings (that can range from -10.00 to +10.00) and system defined coefficients. The system defined coefficients determine what elements are affected by a given knob and the relationship between the elements that must be preserved when the knob setting is changed. A coefficient of zero for an element means that the element is not affected by the knob. The user specified settings determine the strength of a knob's effect — a setting of 0.00 disables the knob. A more complete description of how knobs are implemented is given in the discussion which begins on page 55.

How knobs are used in calibrating the magnetic quadrupoles and sextupoles is discussed in the section beginning on page 58. Knobs provide experimenters a convenient way to select among RMS observables in order to optimize the device to meet the needs of a particular experiment. RMS observables affected by knobs include such items as transmission efficiency, mass resolution, and vertical focus of the recoils at the final focal plane. For example, a particular experiment may require better mass resolution at the expense of transmission efficiency. Another experiment, using a small detector placed behind the focal plane PSAC [1], might require a narrow vertical distribution of recoils to maximize the number of implants on the detector at the expense of mass resolution as observed in the focal plane PSAC.

The fact that eight knobs have been developed for the RMS can be understood in terms of the elements contained in the device. Each of the three quadrupole doublets has a knob associated with its vertical focusing capability (knob 2 for Q1–Q2, knob 8 for Q4–Q5, and knob 7 for Q6–Q7) and a knob associated with its horizontal focusing capability (knob 5 for Q1–Q2, knob 1 for Q4–Q5, and knob 6 for Q6–Q7). The remaining pair of knobs — knobs 3 and 4 — are tied to the two sextupoles. These knobs are used to correct for second order aberrations. An ionization chamber, placed behind the PSAC, is very useful for adjusting these knobs. Knob 3 is used to correct for the $(x/\theta\delta E)$ aberration which shows up as tails in plots of the energy as observed in the ionization chamber vs. the $x$ position of recoils from the PSAC. This aberration also appears as bad resolution of off center

[1] The PSAC is the position sensitive detector used to record the position of recoils entering the focal plane. "PSAC" is an acronym for "position sensitive avalanche counter".

masses. Knob 4 is used to correct for the $(x/\delta E\delta E)$ aberration which shows up as banana shapes in plots of ionization chamber energy vs. PSAC $x$ position.

It is possible to develop knobs affecting larger collections of elements. For example, a knob affecting the quadrupole doublets Q1–Q2 and Q4–Q5 could be created to adjust the position of the finger focal plane inside Q3. Development of knobs is an ongoing process; knobs will be added as needed.

### Modes

When an experimental setup requires large-scale changes in the RMS performance, the knob control feature does not offer enough flexibility to allow for a good optimization of the RMS. In such cases, the RMS optics must be re-optimized with the help of one of the ion-optics codes. Examples of situations requiring such a re-optimization include: changes in target position, changes in focal plane position, and fundamental changes in the focusing strategy at the focal plane. Once different optimization schemes are established, it is possible to switch among the available schemes depending upon the conditions of the experiment. The difference between these schemes lies in the way the quadrupole and sextupole elements of the RMS are scaled with respect to each other. The term we use to describe one of these fundamental scaling schemes is "mode". The knob coefficients that define the proper function of the knobs must be determined separately for each mode. Presently, the same knobs are available in the different modes, although it is conceivable that in the future some knobs could be created that are mode-specific. Currently, we are working with two modes. More modes can be developed in the future as the need arises.

The first mode is called the *diverging* mode. This mode essentially follows the original RMS design presented in Reference [1]. In this mode the position of the focal plane (and, hence, of the PSAC) is 93 cm after the exit of Q7. The horizontal physical separation of different masses at the final focal plane is maximized while preserving a good mass resolution. The horizontal profile in this mode is such that the mass groups diverge from the optic axis after passing through the focal plane. This mode is therefore not suited for experiments requiring the collection of recoil groups with different masses or with the same mass but different charge states in a single small area after they pass through the PSAC. The bottom frames of Figure 13 show the horizontal ($x$) and vertical

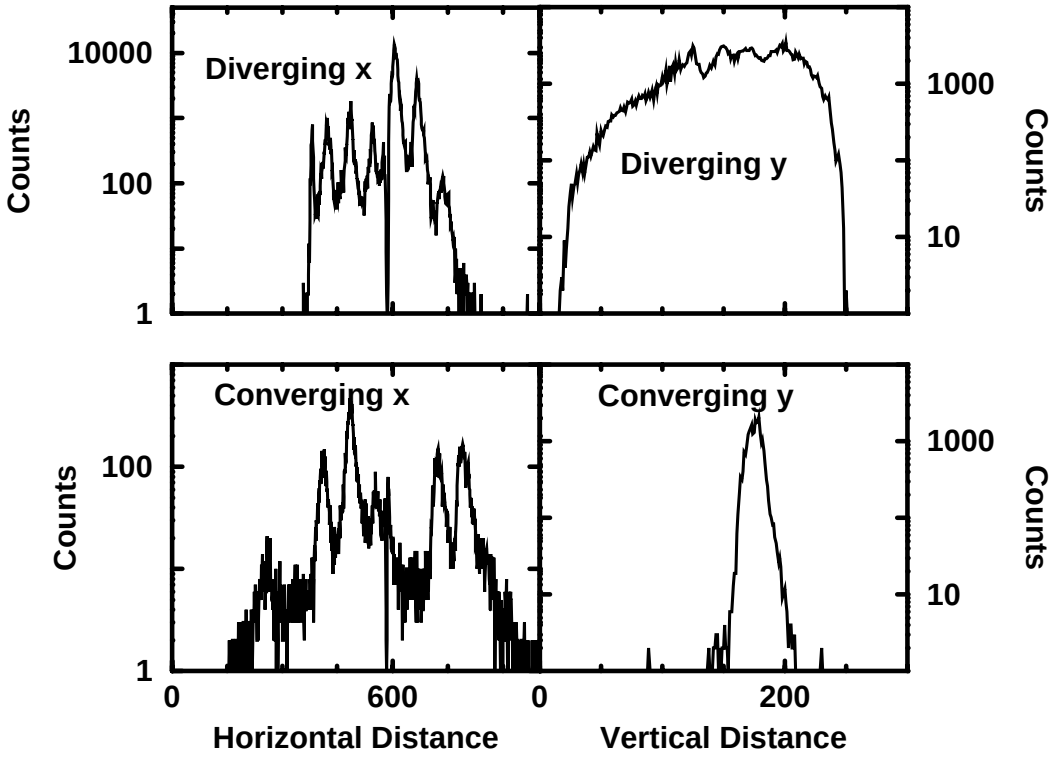


Figure 13: Horizontal and vertical projections of the focal plane recoil distributions obtained for the diverging and converging mass modes. The recoils in the diverging distribution are from the reaction of a 220 MeV $^{58}$Ni beam on a 300 $\mu$g/cm$^2$ $^{60}$Ni target with the RMS scaled to a central recoil of $^{114}$Te at an energy of 103 MeV and a charge state of 25.5$^+$. The recoils in the converging distribution are from the reaction of a 120 MeV $^{32}$S beam on a 300 $\mu$g/cm$^2$ $^{58}$Ni target with the RMS scaled to a central recoil of $^{86}$Zr at an energy of 38 MeV and a charge state of 17.5$^+$. (The RMS was run in early versions of the diverging and converging modes — "mode T" and "mode TN", respectively — described in Report #3, August, 6, 1996 of Reference [29]. In both cases the PSAC was positioned 93 cm from the exit of Q7.)

($y$) recoil distributions generated in this mode. (Note that here we have adjusted the knobs to give a narrow vertical focus to deliver as many recoils as possible from the central mass group onto a small detector placed behind the PSAC.) The diverging mode is the standard mode currently available for all experiments. Table 4 shows the basic field values that define this mode (calculated for a recoil with a mass of 100 amu, an energy of 100 MeV, and a charge state 10$^+$) and the coefficients that define the knobs within this mode.

The second mode is called the *converging* mode. (See Report #6, August 28, 1996 of Reference [29]). The goals of this mode are: (1) to deliver as many recoil mass groups as possible to a

Table 4: Basic field values and knob coefficients for the diverging mode ("mode J" from Report #4, August 6, 1996 of Reference [29]) with a focal plane distance of 93 cm from the exit of Q7. The basic field values listed in the second column are for a central recoil of mass 100 amu, energy 100 MeV, and charge state $10^+$. They are stated in units of Tesla for the magnetic elements and in units of kV for the electric dipoles.

| Element | Basic Field Value | Knob 1 | Knob 2 | Knob 3 | Knob 4 | Knob 5 | Knob 6 | Knob 7 | Knob 8 |
|---|---|---|---|---|---|---|---|---|---|
| Q1 | −0.6945 | 0 | −0.0165 | 0 | 0 | −0.0052 | 0 | 0 | 0 |
| Q2 | +0.3383 | 0 | +0.0017 | 0 | 0 | +0.0008 | 0 | 0 | 0 |
| D1 | +1.0302 | 0 | 0 | 0 | 0 | 0 | 0 | 0 | 0 |
| S1 | +0.5300 | 0 | 0 | +0.0500 | −0.0500 | 0 | 0 | 0 | 0 |
| Q3 | +0.3611 | 0 | 0 | 0 | 0 | 0 | 0 | 0 | 0 |
| S2 | +0.3800 | 0 | 0 | +0.0492 | +0.0499 | 0 | 0 | 0 | 0 |
| D2 | +1.0302 | 0 | 0 | 0 | 0 | 0 | 0 | 0 | 0 |
| Q4 | +0.2078 | +0.0042 | 0 | 0 | 0 | 0 | −0.0005 | −0.0006 | +0.0037 |
| Q5 | −0.2403 | −0.0022 | 0 | 0 | 0 | 0 | +0.0003 | +0.0003 | −0.0120 |
| E1 | 166.6 | 0 | 0 | 0 | 0 | 0 | 0 | 0 | 0 |
| D3 | +1.0302 | 0 | 0 | 0 | 0 | 0 | 0 | 0 | 0 |
| E2 | 166.6 | 0 | 0 | 0 | 0 | 0 | 0 | 0 | 0 |
| Q6 | +0.1169 | 0 | 0 | 0 | 0 | 0 | +0.0175 | +0.0150 | −0.0170 |
| Q7 | −0.3481 | 0 | 0 | 0 | 0 | 0 | −0.0100 | −0.0253 | +0.0289 |

small area behind the focal plane PSAC (for example, the DSSD) and (2) to preserve mass separation at the focal plane so that the PSAC can still be used for mass identification. This mode works by providing a converging focusing solution so that the separated mass groups approach the optic axis after passing through the focal plane PSAC. In order to use this mode, the polarities of Q6 and Q7 must be switched. In this mode the position of the focal plane (and, hence, of the PSAC) is 43 cm after the exit of Q7. Development and testing of this mode is still in progress. The top frames in Figure 13 show the recoil distribution in $x$ and $y$ that an early version of the converging mode generates. (Note that the PSAC is positioned at 93 cm from the exit of Q7, the focal plane position for this early version of the converging mode.) The figure shows that the recoils are spread over a smaller range in $x$ than for the diverging mass mode. Table 5 shows the basic field values (calculated for a recoil with a mass of 100 amu, an energy of 100 MeV, and a charge state $10^+$) that define this mode together with the coefficients that define the knobs within this mode.

Table 5: Basic field values and knob coefficients for the converging mode ("mode22" from Report #6, August 28, 1996, of Reference [29]) with a focal plane distance of 43 cm from the exit of Q7. The basic field values listed in the second column are for a central recoil of mass 100 amu, energy 100 MeV, and charge state $10^+$. They are stated in units of Tesla for the magnetic elements and in units of kV for the electric dipoles.

| Element | Basic Field Value | Knob 1 | Knob 2 | Knob 3 | Knob 4 | Knob 5 | Knob 6 | Knob 7 | Knob 8 |
|---|---|---|---|---|---|---|---|---|---|
| Q1 | −0.6945 | 0 | −0.0165 | 0 | 0 | −0.0052 | 0 | 0 | 0 |
| Q2 | +0.3383 | 0 | +0.0017 | 0 | 0 | +0.0008 | 0 | 0 | 0 |
| D1 | +1.0302 | 0 | 0 | 0 | 0 | 0 | 0 | 0 | 0 |
| S1 | +0.6170 | 0 | 0 | +0.0500 | −0.0500 | 0 | 0 | 0 | 0 |
| Q3 | +0.3665 | 0 | 0 | 0 | 0 | 0 | 0 | 0 | 0 |
| S2 | +0.4397 | 0 | 0 | +0.0492 | +0.0499 | 0 | 0 | 0 | 0 |
| D2 | +1.0302 | 0 | 0 | 0 | 0 | 0 | 0 | 0 | 0 |
| Q4 | +0.2140 | +0.0042 | 0 | 0 | 0 | 0 | 0 | 0 | +0.0037 |
| Q5 | −0.2421 | −0.0022 | 0 | 0 | 0 | 0 | 0 | 0 | −0.0120 |
| E1 | 166.6 | 0 | 0 | 0 | 0 | 0 | 0 | 0 | 0 |
| D3 | +1.0302 | 0 | 0 | 0 | 0 | 0 | 0 | 0 | 0 |
| E2 | 166.6 | 0 | 0 | 0 | 0 | 0 | 0 | 0 | 0 |
| Q6 | −0.3595 | 0 | 0 | 0 | 0 | 0 | −0.0083 | −0.0453 | +0.0479 |
| Q7 | +0.3333 | 0 | 0 | 0 | 0 | 0 | +0.0309 | +0.0175 | -0.0185 |

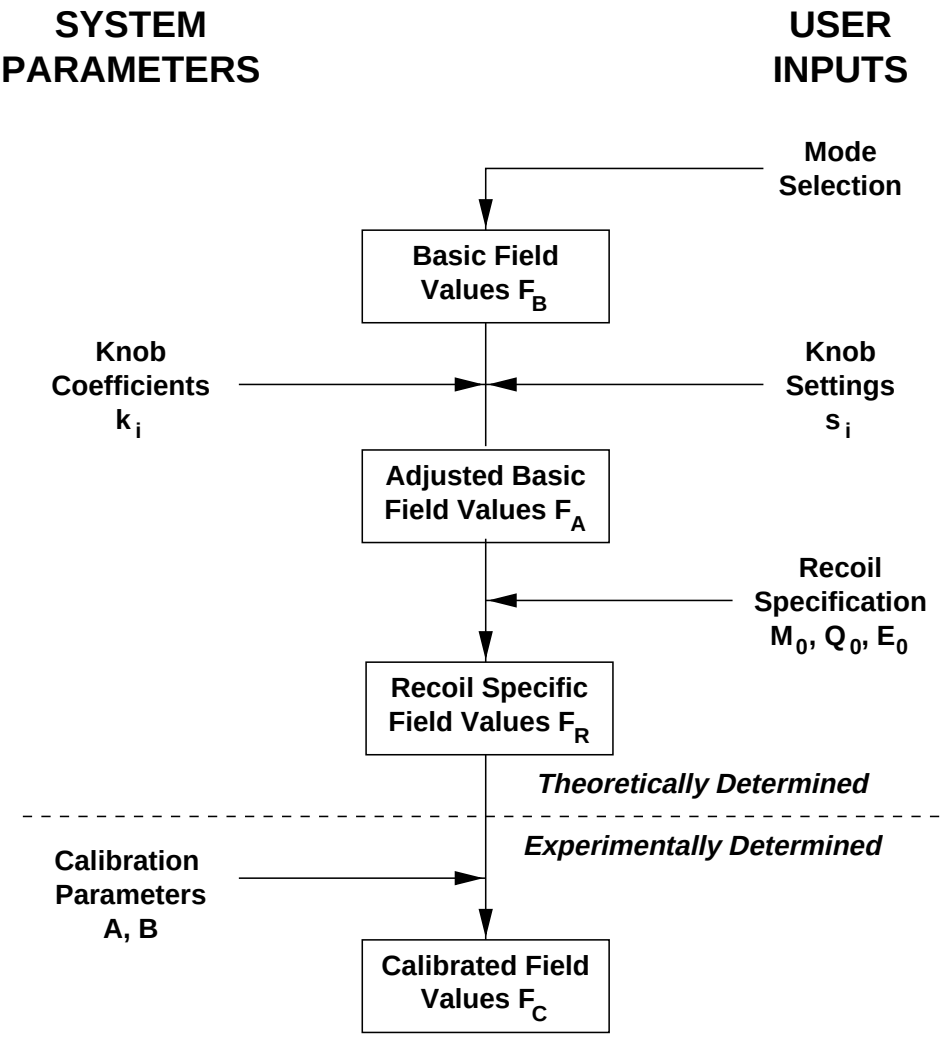


Figure 14: Summary of calculations performed by the control software to determine field settings for the RMS elements.

Element Scaling Algorithm

Figure 14 summarizes how the RMS control system determines the settings for the individual elements based on two categories of input. One category is user input to specify the mode, the central recoil (the ion or its mass, its charge, and its energy), and the knob settings. The second category of input is the system parameters: the numbers defining the modes and knobs, and the constants defining the calibrations of the RMS elements.

The control software starts the calculation with a basic field value set which is determined by the mode selected. The basic field values are simply the calculated element settings required to deliver a distribution of recoils about a central ion value of mass 100 amu, of energy 100 MeV, and

of charge state $10^+$ through the spectrometer in a manner that meets the design objective for the mode. Tables 4 and 5 list the basic field values for the diverging and converging modes. These settings were calculated by using the matrix ion-optical code GIOS [27].

The control software next converts the basic field values into adjusted basic field values which take into account any user requested knob settings. For a given element the adjusted basic field value $F_A$ is calculated from the basic field value $F_B$ by using the formula

$$F_A = F_B + \sum_i s_i k_i \tag{11}$$

where the index $i$ is the knob number, the $s_i$ are the user knob settings, and the $k_i$ are the knob coefficients. Table 4 lists the knob coefficients for the diverging mode, and Table 5 lists those for the converging mode.

The control software next converts these adjusted basic field values into recoil specific field values — that is, the element settings determined not for central recoils of mass 100 amu, energy 100 MeV, and charge state $10^+$, but for central recoils with the mass $M_0$, energy $E_0$, and charge state $Q_0$ requested by the user. The magnetic fields $B$ and the electric fields $\mathcal{E}$ are scaled according to the relations 3 and 7.

Up to this point all calculations for the element settings are based on theoretical considerations. The final step in the calculations makes use of the experimentally determined calibration parameters to convert from the recoil specific field values to calibrated field values. The calibrated field values are the element settings necessary to make the device actually perform in accordance with the predictions from the ion-optical calculations. The calibration parameters were obtained during commissioning runs as discussed beginning on page 57. For a particular element, the calibrated field value $F_C$ is calculated from the recoil specific field value $F_R$ by

$$F_C = A + BF_R \tag{12}$$

where $A$ and $B$ are the system supplied calibration coefficients.

# CHAPTER III

# COMMISSIONING OF THE RMS

In the last chapter we examined the RMS from the point of view of ion optics. This perspective offered not only a deeper qualitative understanding of how the device works, but also an insight into how the exercise of using computers to model the ion optics has been used in the design and optimization of the device. In this chapter we delve into the technical issues related to how the RMS was commissioned: how we have calibrated it and how we have measured its performance.

## Calibration

The point in calibrating a spectrometer is to match the actual field that results when an element is set by the control software to the theoretical value used to model the element's performance. The RMS control software uses measured fields to determine the element settings. The matching of the observed to the theoretical field values is achieved in the control software through use of calibration constants which are applied as described in the section starting on page 55. For the RMS the goal of calibration is to determine these constants. A good calibration essential not only for obtaining the proper fields as the RMS is scaled from one central ion value to another, but also for the successful implementation of new optics solutions based on computer simulations.

### Strategies and Tools

Calibrating a device with 14 elements that can be varied independently and which must be operated together to obtain the observable effects needed for making the calibration presents quite a challenge. Although we have placed much effort into calibrating the RMS, the calibration is still very much an on-going process. Our ability to calibrate the device has evolved as we have enhanced our control system to incorporate knobs to allow feedback from the ion optical models for doing the calibrations; as we have built up our experience working with the RMS under different circumstances, thus learning new strategies for performing calibrations and learning how to read old diagnostics better; as we have introduced more diagnostic tools to help us with the task; and as we iterate on

previous attempts to achieve an ever improving calibration.

We have employed three classes of ions for calibrating the RMS: $\alpha$-particles from a source, low intensity beams directly from the tandem accelerator, and recoils from fusion-evaporation reactions. The next three sections describe how the different characteristics of each class of ions were used to calibrate the RMS. This section provides an overview of the approaches used for calibrating the different kinds of elements within the RMS; it then describes the diagnostic tools available for performing the calibrations.

From the standpoint of calibration, the elements of the RMS can be divided into two groups which require different handling: the dipole elements (both magnetic and electric) and the focusing elements (the quadrupoles and sextupoles). A correct dipole calibration means that as the dipole is scaled for different central ion settings, the corresponding ions will follow the optic axis through the element. (By definition, a central ion is one which enters the element along its optic axis — see page 33.) Thus, the appropriate measured dipole field corresponding to a given central ion is determined by confirming that the ion remains on the optic axis at any arbitrary point after the dipole exit. We have used this direct approach to calibrate dipoles D1 and D2 individually. Because we do not have position diagnostics in place at the exits of E1 or D3, we must use more complicated approaches to calibrate the E1–D3–E2 combination of dipoles together. Two approaches — one with $\alpha$-particles and the other with recoils — are described in the corresponding sections below.

Tuning of the focusing elements cannot be accomplished with the use of central ions. Off-axis ions must be used because the field at the optic axis of these elements is by definition zero no matter what setting is applied. As discussed in the section beginning on page 43 which gives a qualitative description of the elements, the quadrupoles and sextupoles determine the distribution of off-axis particles and thus influence properties such as focusing and the transmission efficiency. A thorough approach to calibrating a focusing element would be to trace the paths of ions before they enter and then to measure their positions at some point after they exit. This approach, however, requires three position sensitive diagnostic tools; the two in front of the element must not interfere with the trajectory of the ion.

The knobs make possible a calibration strategy for the focusing elements which requires a much less complicated diagnostic setup. Observables affected by the focusing elements and by the knobs

which control these elements include transmission efficiency, mass resolution, and the distribution of recoils within the mass groups. As mentioned on page 49 the knobs were designed so that as long as the initial quadrupole and sextupole field calibrations are approximately correct, the knobs can be used to obtain the proper field settings for these elements by optimizing on the basis of the observables. These observables only appear clearly with ions that fill the spectrometer acceptances; thus, to tune the focusing elements with knobs, recoils should be used.

The fields of the RMS magnets are computer controlled via their current settings and magnetic field readings. Each magnet has a Hall probe mounted onto one of its pole faces; the control software adjusts the current of the magnet until the desired field setting as measured by the Hall probe is obtained. The magnetic dipoles are adjusted by using 16-bit controls to obtain a field setting accuracy of $\pm 0.2$ Gauss and maximum field settings of around 10,000 Gauss. All other magnets are adjusted by using 12-bit controls to obtain a field setting accuracy of $\pm 2$ Gauss and maximum field settings of around 8,000 Gauss.

An initial calibration of the magnets was obtained by comparing the field vs. current data provided by the manufacturer (measured along the optic axis) to that resulting from the present placement of the Hall probe on the pole face. This calibration was implemented by applying a linear correction factor (the constant $B$ in Equation 12) to the requested field value. These factors are listed in Table 6. This calibration was in place before any attempts were made to calibrate with ions.

The fields for the electrostatic dipoles are supplied by Cockcroft-Walton high voltage multiplier stacks powered by high frequency drivers. Each of the two plates in each of the electrostatic dipoles has its own multiplier stack and driver. Since the field settings requested by the computer are sent to the drivers via 16-bit DACs, the voltage can be set to something on the order of $\pm 0.005$ kV, given that the maximum possible field settings are 300 kV. The drivers use the current passing through 6 G$\Omega$ resistor chains from the high voltage end of the stacks to regulate the field settings. These current and the resulting voltage values are sent back to the computer from the high voltage drivers via 16-bit ADCs. When the electrostatic dipoles are being conditioned to hold high voltages, the control software uses these values to regulate the process. In normal operation, the control software monitors these values to prevent conditioning from taking place by dropping the requested voltage,

Table 6: Initial magnet calibration factors used to correct for the placement of Hall Probes on the pole faces of the magnets. These constants were derived from a comparison of field vs. current data measured at the optic axis by Danfysik, the magnet manufacturer, to that obtained from the Hall Probes as they are presently mounted.

| Magnetic Element | Scaling Factor |
|---|---|
| Q1 | 1.3173 |
| Q2 | 1.2869 |
| D1 | 1.0000 |
| S1 | 1.3931 |
| Q3 | 1.2744 |
| S2 | 1.4125 |
| D2 | 1.0000 |
| Q4 | 1.2820 |
| Q5 | 1.2183 |
| D3 | 1.0000 |
| Q6 | 1.2823 |
| Q7 | 1.2914 |

if necessary. No initial calibration was applied to E1 and E2 other than a hardware calibration within the high voltage drivers to match them to their stacks.

We have employed a variety of tools for calibrating the RMS. These tools provide information about the position, distribution, or energy of ions at various locations within the spectrometer. The most versatile diagnostic tool has been the position sensitive detector at the focal plane called the PSAC (for position sensitive avalanche counter). The $x$-position signal from the PSAC gives direct information on the horizontal position of ions at the focal plane with respect to the optic axis and is used to determine the RMS $M/Q$ acceptance, mass dispersion, and mass resolution. The two-dimensional distribution of recoils given by the PSAC is used to reveal the presence of aberrations in the focal plane image. Changes in the PSAC count rate can be used to optimize the transmission of recoils through the RMS as well as to infer position information on ions at intermediate RMS locations as mechanical blocking or collimating devices are inserted and removed. Changes in the observed position of ions at the PSAC in response to changes in a quadrupole field setting can be used to infer the position of the ions in relation to the optic axis at the quadrupole.

The *mini-PSAC* is a smaller version of the PSAC which can be used at the finger focal plane, at the achromatic focus, or at the final focal plane. It has an active area of 6 cm by 6 cm (compared

Table 7: Position at which fingers intercept the optic axis inside Q3.

| Finger | Position (cm) |
|---|---|
| 1 | 13.41 |
| 2 | 13.35 |
| 3 | 13.36 |
| 4 | 13.45 |
| 5 | 13.45 |
| 6 | 13.40 |
| 7 | 13.55 |

to the 10 cm vertical by 36 cm horizontal active area covered by the larger PSAC). The mini-PSAC provides the same information as the larger PSAC. The precise position of the detector with respect to the optic axis has not been checked at the finger focal plane location. At the achromatic focus location, we have verified that the optic axis passes close to the center of the detector.

Another diagnostic tool is the variety of mechanical devices described below for physically blocking or collimating ions within the RMS. All of these devices can be introduced and removed quickly without breaking vacuum.

Four collimators, one pair forming a vertical slit and the other pair forming a horizontal slit, are located about a meter in front of the target position. The positions of the collimators are adjusted by means of linear vacuum feed-throughs. A mechanical stop on each collimator marks the position where it reaches the optic axis. The use of these slits for positioning the beam is described in the section on beam tuning (see page 68).

The fingers at the Q3 focal plane provide another mechanical means for checking the position of ions within the RMS. The location of each of the seven fingers can be adjusted independently through the RMS control software. Table 7 list the position at which each finger crosses the optic axis.

Another mechanical means for defining the position of ions in the RMS is provided by collimators at the achromatic focus. Either one of two circular apertures can be brought into position centered about the optic axis — one with a diameter of 1 cm and the other with a diameter of 5 cm.

A possible pitfall of using collimators, fingers, or apertures is that beam particles scattered from

an edge of these devices may result in an increased count rate on a downstream detector when in fact the device is blocking part of the beam. The use of these devices may also lead to confusion if the distribution of ions is large compared to an opening used to transmit the ions or to a piece used to block them.

Eventually a beam profile monitor will be placed on the beam-line to the RMS just in front of the target position. Because this monitor will employ a residual gas detection strategy, it will not interfere with the beam. It can thus be used as a continuous position and intensity monitor.

Another diagnostic tool available is the ionization chamber which is used at the focal plane behind the PSAC to provide position, energy, and relative energy loss information about the ions which enter it. In particular, plots of the total ion energy from the ionization chamber vs. the horizontal ion position from the PSAC are useful in tests with recoils for adjusting the sextupoles with knobs 3 and 4 and for calibrating the mass separator dipoles.

Of course all of these tools are not available at all times. For example, the mini-PSAC at Q3 means no mini-PSAC at the achromatic focus — it is a non-trivial task to install or remove this detector. Using the mini-PSAC at the achromatic focus or at the Q3 focal plane prevents simultaneous use of collimators or fingers at those locations. Although the mini-PSAC allows most of the ions it detects to pass through to down stream detectors, it interferes with the ions by degrading them in energy and by changing their charge states.

### Alpha-Particle Tests

One class of ions employed for commissioning the RMS has been $\alpha$-particles from a radioactive source. The most obvious advantage of making calibrations with an $\alpha$-source is that accelerated beams from the tandem are not needed. In order to be useful, the source must be rather strong — especially if it is placed behind a collimator to localize the position and the emission angle of the $\alpha$-particles. Another advantage of $\alpha$-particles from a source is that they are mono-energetic; there may be uncertainty as to the exact energy of the emitted particles, however, depending on how deeply the activity is implanted into the source substrate. A disadvantage of these ions is that it takes some care and effort to mount and align the source — especially if it is a strong source because of the radiological control considerations. A disadvantage of a source emitting $\alpha$-particles with a single

energy is that it can provide only one calibration point for each element. Even though it is possible to see $\alpha$-particles from a source in the $1^+$ charge state which could be used for a second calibration point, these ions are not very useful for tests that require a series of measurements because of their low relative intensity.

We used a $^{244}$Cm $\alpha$-source with a strength of a few tens of $\mu$Ci to calibrate the elements of the RMS before the beam-line from the accelerator was in place. We assumed that the $\alpha$-particles emerged from the source with their full energy of 5.805 MeV. We placed the source at two positions for these tests: at the achromatic focus and at the target position. In each location we aligned the source along the RMS optic axis by using a 1 mm aperture which also served to collimate the source. For the electric and magnetic dipoles, the goal of the test was to insure that the $\alpha$-particles followed the optic axis as evidenced by the position of the particles observed either on the large PSAC placed at the focal plane or on the mini-PSAC placed either inside of Q3 or at the achromatic focus. For the quadrupoles the goal was to adjust the doublets Q1–Q2, Q4–Q5, and Q6–Q7 to minimize the distribution of $\alpha$-particles observed while keeping it symmetric horizontally and vertically. We used $\alpha$-particles to tune all elements of the RMS except S1, S2, and Q3.

To tune the elements in the mass separator section of the RMS, we placed the source at the achromatic focus and observed the resulting position of the $\alpha$-particles on the focal plane PSAC. We set D3 to its predicted value and sought the E1 and E2 settings that are matched to this value. The correctly matched pair of electric dipole settings has two characteristics: (1) it delivers the $\alpha$-particles to the optic axis at the PSAC, and (2) it directs particles along the optic axis between the exit of E2 and the focal plane. The test that the second requirement has been met is that no steering of the particles at the PSAC occurs when we make large changes to the quadrupole settings. To find this correctly matched pair of settings, we mapped out a set of points in E1, E2 space that delivered $\alpha$-particles to the optic axis at the focal plane PSAC with Q6 and Q7 turned off. From this set we found the pair for which steering of the $\alpha$-particles with Q6 and Q7 turned on was minimized as is illustrated in Figure 15. Using this matched pair, we then tuned the Q6–Q7 doublet by minimizing the spot size.

For tuning D1 we placed the $\alpha$-source at the target position and the mini-PSAC at Q3. We found the D1 value that steered the $\alpha$-particles to the center of the mini-PSAC. We used this same

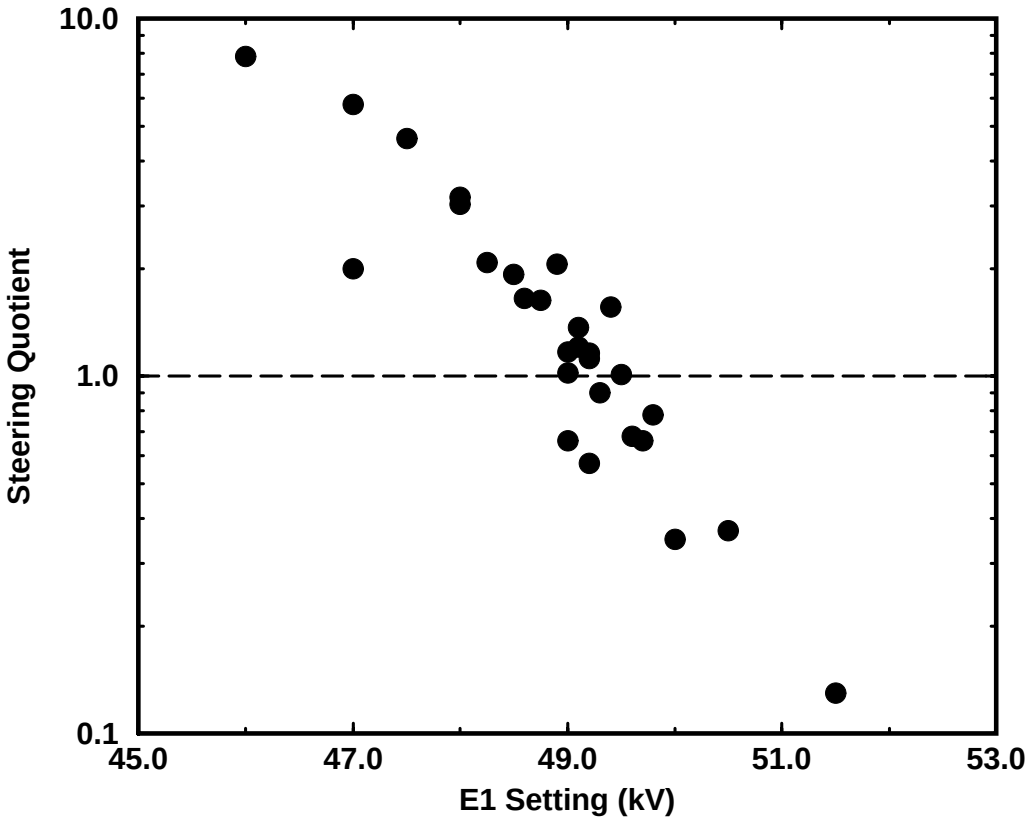


Figure 15: Plot of steering quotient vs. E1 values for pairs of E1–E2 values which deliver $\alpha$-particles to the optic axis at the focal plane PSAC. The steering quotient is defined as the ratio of the number of $\alpha$-particles on the left of the optic axis to the number on the right with quadrupoles energized divided by the same ratio observed with the quadrupoles not energized. A quotient of one thus indicates minimal steering. The number of events on the left or right side of the optic axis is easily determined because of the construction of the PSAC: the detector is electrically segmented into two horizontal sections which are positioned on either side of the optic axis.

Table 8: Data used for obtaining calibration coefficients for the mass separator dipoles D1, D2, E1, D3, and E2 in tests with $\alpha$-particles. The best field values determined experimentally are listed together with the corresponding theoretical values derived from GIOS calculations. To give a feel for how the field values used for the calibration compare to typical RMS field values, the table also lists the theoretical values for a typical RMS setting used to look at $^{113}$Cs recoils.

| | Calibration Field Value [a] | | $^{113}$Cs Field Value [b] |
|---|---|---|---|
| Element | Experimental | Theoretical | Theoretical |
| D1 (Gauss) | 2440.0 | 2482.96 | 3870.92 |
| D2 (Gauss) | 2445.0 | 2482.96 | 3870.92 |
| E1 (kV) | 49.20 | 48.35 | 58.30 |
| D3 (Gauss) | 2482.4 | 2482.96 | 3870.92 |
| E2 (kV) | 48.54 | 48.35 | 58.30 |

[a] For an RMS central ion setting of $^{4}$He at 5.805 MeV and charge state $2^{+}$.
[b] For an RMS central ion setting of $^{113}$Cs at 98 MeV and charge state $28^{+}$. These recoils are produced in the reaction of a 235 MeV beam of $^{58}$Ni on a 500 $\mu$g/cm$^2$ $^{58}$Ni target.

configuration to tune the Q1–Q2 doublet. We moved the mini-PSAC to the achromatic focus for tuning D2. Using the settings we found for Q1, Q2, and D1, we sought the D2 setting that delivered the $\alpha$-particles to the center of the mini-PSAC. We used this setting to tune the Q4–Q5 doublet.

Finally we checked the entire system by allowing the $\alpha$-particles to pass from the target position all the way through to the focal plane PSAC, noting that the particles appeared in a localized spot on the optic axis. Table 8 summarizes the optimum dipole fields found from these tests. In the first test with recoils, which was made by using only calibration coefficients obtained from work with $\alpha$-particles, we obtained an $M/Q$ dispersed image at the focal plane. The table also lists the calculated field settings for a representative reaction frequently run at the RMS to give a feel for how the field values obtained for the $\alpha$-particle calibration point compare to the fields actually used in a "typical" experiment. This representative reaction was chosen because the beam and target are easy to use, because it is similar to that used to measure many of the performance parameters of the RMS (see the second part of this chapter beginning on page 83), and because it produces the proton emitter $^{113}$Cs frequently used to test the DSSD setup.

Note that we made no attempt to optimize the setting of magnet D3. We simply assumed that the value we started with was the correct one to use. In other words, we assumed not only that the initial D3 calibration was correct so that we obtained the correct measured field setting for

Table 9: Example of hysteresis in magnetic dipole D3. Setting I was obtained by increasing the current from zero after "cycling" the magnet. Setting II was obtained by increasing the current from setting I. Setting III was obtained by dropping the current after the current was raised to its maximum value of 500 A. Setting IV was obtained by increasing the current from zero after "cycling" the magnet.

| Setting | Requested Current (A) | Measured Current (A) | Measured Field (Gauss) | $\alpha$-particle $x$-position Centroid at Focal Plane (channel #) |
|---|---|---|---|---|
| I | 120.96 | 120.92 | 2454.4 | 535 |
| II | 122.00 | 121.96 | 2475.2 | 415 |
| III | 120.96 | 120.92 | 2475.2 | 391 |
| IV | 121.98 | 121.94 | 2475.2 | 416 |

5.805 MeV $\alpha$-particles, but we also assumed that the central energy of the $\alpha$-particles was indeed the full 5.805 MeV. The consequence of this procedure is that, while E1–D3–E2 were properly tuned with respect to each other, they were probably tuned for some energy slightly off of the nominal value. It is certainly possible to miss the proper energy setting given the fact that the energy distribution of the $\alpha$-particles from the source is well defined and that the energy acceptance of the separator is $\pm 10\%$.

In the course of calibrating the RMS with $\alpha$-particles, we also made some measurements which show that the magnets can be subject to hysteresis effects, even though we are using the measured fields and not the currents to set the magnets. Our procedure for the mass separator dipole calibration was to leave D3 set to a particular value and to match the fields by varying E1 and E2. We took this approach to prevent having to worry about hysteresis effects from changing D3 and since it is much faster to change the electric dipole settings. To explore the effects of hysteresis, however, we did a test where we varied only the field of D3 while leaving the settings of E1, E2, Q6, and Q7 unchanged. Results from this test are summarized in Table 9. Only increases in current were used in making setting I and in going from setting I to setting II. Setting III, however, was made by dropping the current to around 120 A after the magnet was run at its maximum setting of 500 A. Note that, even though the current settings are identical, the measured field from III does not match the field measured in I and the response of the system differs as is demonstrated by the position of the $\alpha$-particles. (The central position of the $\alpha$-particles shifts at the focal plane by 144

channels horizontally which corresponds to a distance of 7.2 cm.) This is an example of the expected behavior from hysteresis. The surprise comes in comparing settings II and III: even though these have the same measured field values, the response of the system differs as is demonstrated by the $\alpha$-particle position shift of 24 channels (1.2 cm). Thus, the strategy of using the measured field from the magnets is not always enough to protect against hysteresis effects. Setting IV was obtained by increasing the current from zero after "cycling" D3 – *i. e.*, after setting the current to zero, ramping it to 500 A, and ramping it back to zero. Note that setting IV is almost identical to setting II both in terms of the measured field in response to the current setting and in terms of the resulting position of the $\alpha$-particles; it demonstrates that indeed the magnets do behave in a repeatable manner. In changing the RMS from one central ion setting to another, we do not normally cycle the magnets. The fact that we do not see any bad effects from not always cycling the magnets is presumably because the field changes involved are generally small.

### Tests with Beam

Another class of ions we have employed for commissioning the RMS has been low intensity beams of particles directly from the tandem accelerator. The crucial point here is that the beam intensity must be kept very low in order not to flood or damage detectors (such as the PSAC, the mini-PSAC, and the ionization chamber) used for diagnostic purposes. To achieve the required low intensity the beam must be reduced to almost unreadable levels by introducing sieves and by adjusting the ion source. To lower the intensity even further, we use a thin foil at the RMS target position to strip the beam from the single charge state delivered by the tandem into a distribution of charge states. Only charge states at the ends of the distribution have an intensity low enough to be usable.

There are several advantages offered by low intensity beams for calibration purposes compared to other types of ions. One advantage is that the beam energy is narrowly defined, and its value is known precisely. Another advantage is that the small emittance of the beam leads to a narrow $x$ and $y$ profile for the particles throughout the spectrometer — the discussion on quadrupoles below explores how this feature may prove to be useful. Another advantage of using beam particles for calibration is that a single stripping foil and a single beam energy setting can lead to two widely separated calibration points: a low rigidity point from a charge state at the upper end of the charge

state distribution and a high rigidity point from the lower end of the charge state distribution.

A disadvantage of using low intensity beams for calibration tests compared to $\alpha$-particles is that it is more difficult to ensure that the beam position is set properly to enter at and follow along the optic axis. A disadvantage in comparison to recoils is that because the beam particles do not fill the angular and energy acceptances of the spectrometer, they cannot be used with knobs to tune the focusing elements. Another disadvantage in comparison to recoils is that the beam particles typically have a higher electric rigidity and thus demand higher field settings from the electric dipoles. As is shown by Equation 8, which defines electric rigidity, these higher values for beam particles result from the fact that they typically have higher energies and lower charge states than the recoils they produce. (Note that electric rigidity does not depend on mass and that the lower beam charge states have the highest rigidity values.) High rigidity is a problem because the electric dipoles must be conditioned to the higher voltages than are typically used for recoils.

An example of a low intensity tandem beam we have used for commissioning tests is $^{32}$S ions at 100 MeV in the $5^+$ charge state. These ions lose 0.329 MeV in the 20 $\mu$g/cm$^2$ carbon foil used for stripping. Resulting ions in the $16^+$ charge state require electric dipole field settings in the range from 100 to 110 kV.

Beam Tuning Procedures

This section provides a brief overview of how beams are tuned and positioned for use in experiments at the RMS — both low intensity beams which are used for commissioning tests and higher intensity beams used to produce recoils. Beams are tuned visually by using the glow produced when the ions strike a "phosphor" — a small, thin slab of chromium doped alumina — placed at the target position. In order to avoid creating dead areas on the phosphor too rapidly, the beam intensity is kept much lower for tuning than the values typically used for recoil production.

GIOS simulations suggest that the spot size at the RMS target position should not extend beyond $\pm 1$ mm in $x$ and $\pm 1$ mm in $y$ (a maximum area of 4 mm$^2$). (See Report #2, August 7, 1995, of Reference [29].) The spot shape we typically use to obtain good resolution is an ellipse taller than it is wide by about a factor of four. Dead areas on the phosphor can cause confusion when the beam spot shape is being adjusted. A set of steerers for shifting the beam horizontally and vertically is

located about 2.5 meters in front of the RMS target position; these can be used to deflect the beam to a region of the phosphor free from dead areas for adjusting the spot shape.

For a properly tuned beam, the beam-line quadrupoles immediately in front of the RMS should not steer the beam. Thus, a quick way to check the quality of the beam tune is to vary the field of each quadrupole in the doublet to ensure that no "walk" occurs in the beam spot observed on the RMS phosphor. Another quick way to check the quality of the beam tune is to compare the beam intensity measured on the Faraday cup at the exit of the tandem to that measured on the cup in front of the RMS. A significant loss in intensity between the two cups (say more than 10 to 20%) indicates a problem with the tune.

Ideally, the steerers in front of the RMS should not be needed to position the beam onto the optic axis at the target location; the steerers are available, however, for making small corrections when necessary. The position of the beam can be checked by using the collimators just in front of the target which close onto the optic axis forming a vertical and a horizontal slit[1]. The procedure for checking the horizontal placement of the beam is with the horizontal slit all the way open to close the vertical slit while viewing the beam spot on the phosphor. The spot should disappear with the slit closed. The beam is positioned correctly if the response of the beam spot as observed on the phosphor is the same as first one side of the slit is opened and closed and then as the other side of the slit is opened and closed. The analogous procedure is used to check the vertical placement of the beam. Once the beam has been positioned by using the slits, they are left all the way open to prevent the scattering of beam particles from the edges of the slits into the RMS.

Once the phosphor has been removed, it is important to re-check the beam position. This point is particularly true if the beam intensity is increased by making large adjustments at the ion source because such adjustments can cause the beam position to shift at the RMS target. Proper horizontal beam positioning can be checked by observing changes in the count rate on the focal plane PSAC as the horizontal steerer in front of the RMS is used to shift the beam equal amounts to the left and right of its original position. For recoils, the count rate usually increases dramatically when the beam begins to strike the target frame which is centered about the optic axis. GIOS calculations

[1] The "vertical slit" is formed by moving the collimators in from the sides to form a tall, narrow vertical opening, while the "horizontal slit" is formed by moving the collimators in from the top and bottom to form a short, wide horizontal opening.

suggest that the mass resolution obtained for recoils is quite sensitive to correct beam positioning — that the resolution drops dramatically for shifts in beam position of more than 1 mm. (See report #7, September 2, 1997, of Reference [29].) Proper vertical positioning of the beam can be checked by steering the beam into the target frame or by looking at the response of the vertical distribution of recoils at the focal plane to changes in the vertical positioning of the beam as was discussed in conjunction with Figure 12. Also, the recoil rate is lower if the vertical positioning is not centered.

Quadrupoles

The distribution of beam particles in the focal plane PSAC is very well localized when the quadrupoles are set to their normal field values. In a test where we turned off all of the quadrupoles in the system, we noted that, although not as well localized, the beam particles at the focal plane fall well within the boundaries of the PSAC. This observation suggests that it should be possible to determine whether or not the position of the beam is coincident with the optic axis at the location of a quadrupole (and perhaps even a sextupole) by looking for shifts in the observed position of beam particles at the focal plane PSAC when the field of the element is changed dramatically. This test assumes that the quadrupole is, of course, aligned properly so that the its central axis coincides with the RMS optic axis. This test will not work if significant changes to the quadrupole field causes the distribution of recoils to extend significantly beyond the edges of the PSAC since it would then be difficult to know where the center of the distribution lies. Shadowing caused by apertures within the system may also make it difficult to tell if the distribution of beam particle has shifted. Steering effects should be more evident for beams that have lower magnetic rigidity — *i.e.*, for beams with lower masses, lower energies, and higher charge states (see Equation 4). If the distribution of beam particles in the finger focal plane at Q3 remains localized enough as quadrupoles Q1 and Q2 are varied, it should be possible to use only the count rate (normalized for fluctuations in the beam intensity) observed with the focal plane PSAC to infer steering from Q1 and Q2 based on changes in the position of the fingers needed to block the beam.

Table 10: Data used for obtaining new calibration coefficients for the momentum achromat dipoles D1 and D2 in tests with beam. The best field values determined experimentally for a low field and a high field calibration point are listed together with the corresponding theoretical values derived from GIOS calculations. To give a feel for how the range of field values covered by the two calibration points compares to typical RMS field values, the table also lists the theoretical values for a representative RMS setting used to look at $^{113}$Cs recoils.

| | Low Field Value [a] | | High Field Value [b] | | $^{113}$Cs Field Value [c] |
|---|---|---|---|---|---|
| Element | Experimental | Theoretical | Experimental | Theoretical | Theoretical |
| D1 (Gauss) | 2920.6 | 2975.63 | 6137.0 | 6199.24 | 3870.92 |
| D2 (Gauss) | 2927.0 | 2975.63 | 6143.1 | 6199.24 | 3870.92 |

[a] For an RMS central ion setting of $^{58}$Ni at 90 MeV and charge state $25^+$.
[b] For an RMS central ion setting of $^{58}$Ni at 90 MeV and charge state $12^+$.
[c] For an RMS central ion setting of $^{113}$Cs at 98 MeV and charge state $28^+$. These recoils are produced in the reaction of a 235 MeV beam of $^{58}$Ni on a 500 $\mu$g/cm$^2$ $^{58}$Ni target.

Momentum Achromat Dipole Calibration Revisited

An important advantage of using beam particles for dipole tuning is the accuracy with which their energy is known. To obtain an improved calibration of the momentum achromat dipoles we used charge states from a 90 MeV beam of $^{58}$Ni generated in a 10 to 20 $\mu$g/cm$^2$ thick $^{nat}$C stripping foil placed at the RMS target position. The trajectory of the beam particles entering the RMS was adjusted by using the steerers in front of the RMS. The setting for the steerers was determined based on (1) the response of the position of the group of beam particles observed in the focal plane PSAC with the fields of quadrupoles Q1 and Q2 turned on and off, and (2) the count rate observed in the PSAC. To optimize D1 we positioned finger 4 to intercept ions on the optic axis inside of Q3 and varied D1's field setting to find the minimum count rate on the focal plane PSAC. We found the optimum D1 fields for two beam charge states: $25^+$ and $12^+$. We optimized D2 for the same two charge states by finding the fields necessary to give the maximum count rate in the PSAC with the 1 cm aperture centered on the optic axis in place at the achromatic focus. Table 10 lists the experimentally determined optimum field values together with the corresponding theoretical values. The two calibration points from the two charge states of the beam cover a wide range of dipole settings, including the values for the representative setting, which are also listed in Table 10. This calibration was done in the diverging mode. Although not done because of the time required, the

same approach as was used with the $\alpha$-particles to tune the mass separator dipoles could also have been used with beam particles.

### Tests with Recoils

The primary advantage offered by recoils from fusion-evaporation reactions for commissioning tests is that these ions typically have sufficiently wide angular and energy spreads to fill the spectrometer acceptances. Recoils thus make it possible to use knobs for tuning the focusing elements and to use energy dispersion effects observed at the focal plane for tuning the mass separator dipoles. A disadvantage of recoils is that it is difficult to know their central energy because it is difficult to know the target thickness with any accuracy — especially since the thickness of the target can change as it is exposed to the beam. It is easy enough to switch between using recoils and using beam particles for commissioning by simply changing the beam intensity and switching between the target used for producing recoils and a thin stripping foil. In fact, it is even possible to use charge states of the beam from the reaction target; the extra thickness of the target merely causes the beam particles to be degraded more in energy and introduces a bit more angular and energy straggling.

#### Quadrupole Calibration

Procedures for using knobs to optimize the quadrupole and sextupole field settings are discussed in Reports #2 (August 7, 1995), #6 (August 28, 1996), and #7 (September 2, 1997) of Reference [29]. Once optimum field values are found by varying the knobs, the new calibration constants are those which cause the control software to request the optimum field values when the knobs are reset to zero. The rationale behind this approach is discussed in more detail in Report #3 (August 6, 1996) of Reference [29].

Optimum knob settings were found by using recoils from the reaction of a 120 MeV beam of $^{32}$S on a $^{58}$Ni target. The RMS was scaled to accept central ions of $^{86}$Zr at an energy of 38 MeV and a charge state of $16.5^{+}$. The detectors used for this exercise included the large PSAC at the final focal plane and, to monitor the count rate from $\gamma$-rays produced in the reaction, four 25% Compton-suppressed germanium detectors at the target position. First we optimized knob 2 to obtain maximum transmission through the vertical gaps in dipoles D1 and D2 as monitored by

Table 11: Data used for obtaining calibration coefficients for the RMS quadrupoles and sextupoles in tests with recoils. The best field values determined experimentally for a low field and a high field calibration point are listed together with the corresponding theoretical values derived from GIOS calculations. To give a feel for how the range of field values covered by the two calibration points compares to typical values, the table also lists the theoretical values for a representative RMS setting used to look at $^{113}$Cs recoils.

| Element | Low Field Value [a] | | High Field Value [b] | | $^{113}$Cs Field Value [c] |
|---|---|---|---|---|---|
| | Experimental (Gauss) | Theoretical (Gauss) | Experimental (Gauss) | Theoretical (Gauss) | Theoretical (Gauss) |
| Q1 | 2928 | 2405.02 | 3600 | 2973.41 | 2609.52 |
| Q2 | 1376 | 1171.52 | 1708 | 1448.39 | 1271.13 |
| S1 | 2292 | 1835.36 | 2834 | 2269.13 | 1991.42 |
| Q3 | 1432 [d] | 1250.47 | 1771 [d] | 1546.00 | 1356.80 |
| S2 | 1596 | 1315.92 | 1974 | 1626.92 | 1427.81 |
| Q4 | 860 | 719.60 | 1064 | 889.67 | 780.79 |
| Q5 | 916 | 832.15 | 1132 | 1028.81 | 902.90 |
| Q6 | 748 | 404.82 | 924 | 500.49 | 439.24 |
| Q7 | 1544 | 1205.45 | 1908 | 1490.35 | 1307.95 |

[a] For an RMS central ion setting of $^{86}$Zr at 38 MeV and charge state $16.5^+$ (diverging mode).
[b] For an RMS central ion setting of $^{114}$Te at 103 MeV and charge state $25.3^+$ (diverging mode).
[c] For an RMS central ion setting of $^{113}$Cs at 98 MeV and charge state $28^+$. These recoils are produced in the reaction of a 235 MeV beam of $^{58}$Ni on a 500 $\mu$g/cm$^2$ $^{58}$Ni target.
[d] The experimental fields listed for Q3 are those scaled from the GIOS prediction (multiplied by the factor from Table 6) after being reduced by 10% to make use of the observation that the mass resolution is optimized with Q3 set 10% low.

the count rate observed on the PSAC normalized by the $\gamma$-ray singles rate observed at the target. Next we again used the normalized PSAC count rate to optimize knob 8 for maximum transmission through the vertical gap in D3. We also found the value of knob 7 that gave the minimum vertical distribution of recoils in the PSAC. We optimized the remaining knobs by looking at the shapes and distributions of mass groups in the PSAC. Note that while we did optimize knobs 3 and 4, the ionization chamber was not in place to help with this task. The quadrupole and sextupole field values from the optimum knob settings are listed in Table 11 together with the corresponding theoretical values. (The optimum knob settings were knob 1 at -1, knob 2 at 0.5, knob 4 at -1, knob 7 at 6, and knob 8 at -5; the remaining knobs — 3, 5, and 6 — had a best setting of 0.)

We obtained field values for a second point in the calibration by using the same knob settings with the RMS scaled to accept central ions of $^{114}$Te at an energy of 103 MeV and a charge state of $25.3^+$. We confirmed that at least some of the knob settings were still optimum for these recoils

which were produced with a 220 MeV beam of $^{58}$Ni ions on a 300 $\mu$g/cm$^2$ target of $^{60}$Ni. The numbers for this calibration point are also listed in Table 11. Note that the ranges in magnetic field values resulting from the two calibration points do not cover the "typical" values given in the table for $^{113}$Cs recoils.

This focusing element calibration was performed by using knobs in an older version of the diverging mode ("mode T" — see Report #3, August 6, 1996, of Reference [29]) which has slightly different knob coefficients than those listed in Table 4. The theoretical scaling numbers listed in the table are from the current version of the diverging mode ("mode J" — see Table 4). The calibration described here was made with an initial calibration in place which was based on early, somewhat blind attempts in which recoils and $\alpha$-particles were used to optimize all focusing elements except S1, S2, and Q3 by adjusting the element fields individually. As stated earlier, the idea behind the way the knobs are designed is that they can be used to bring the quadrupoles to their proper settings if their initial settings are even only roughly correct. Thus, even if a very bad initial calibration prevents us from finding the "best" new calibration by using the knobs, the new calibration presumably will be closer to being correct and we can still recover the optimum settings by adjusting the knobs under the new calibration.

Since no knobs affect the field setting of Q3, the procedure of optimizing knob settings cannot be used to determine the Q3 calibration constants. After obtaining the optimum field settings for the other focusing elements with knobs, we noticed that we could significantly improve the mass resolution observed at the focal plane by reducing the field of Q3. It is thus possible to think of the field of Q3 as a separate knob to be adjusted with mass resolution as the observable it affects. An idea of using the horizontal distribution of recoils observed with the mini-PSAC at the achromatic focus as a guide for obtaining the optimum setting for Q3 is discussed in Report #4 (August 14, 1996) of Reference [29].

The calibration for the focusing elements was done by using the diverging mode. Since it may turn out that most RMS work will be done with the converging mode, it perhaps makes sense to re-calibrate these elements by re-normalizing knobs in the converging mode. (The current optimum knob values for the converging mode are not near zero.) If a new calibration is performed, optimum knob values should be found by using recoils from two reactions requiring significantly different

quadrupole and sextupole field settings so that two calibration points can be found that cover a wide range of RMS settings.

Mass Separator Dipole Calibration Revisited

The initial calibration of the mass separator dipoles E1–D3–E2, based on the $\alpha$-source data, was not satisfactory. Under that calibration, the central recoil would hit the PSAC to the right of the optic axis (located at the PSAC center). Our usual way to compensate for this effect was to decrease the requested central ion charge state setting to shift the mass spectrum to the left. We typically needed to decrease this setting by 10 to 20% of one unit of charge; for example, in one run to get the $28^+$ charge state of 98 MeV $^{113}$Cs recoils to hit the optic axis, we had to lower the central ion charge state setting to 27.83.

We revisited the mass separator dipole calibration by using recoils. Since we have a high degree of confidence in the calibration of the momentum achromat dipoles D1 and D2 from the tests with beam ions, we do not have to worry too much about uncertainty in the scaling of D1 and D2 confusing the results for the mass separator dipoles. The primary new tool at our disposal was the ionization chamber positioned at the focal plane behind the PSAC. This detector arrangement allowed us to make plots of the recoil energy (from the ionization chamber) vs. the recoil position ($x$ from the PSAC). A proper tune of the E1–D3–E2 setup should result in mass groups at the focal plane which do not show any energy dependence. In other words, the mass groups in the energy vs. recoil position plots should appear as vertical bars — they should not tilt to the right or left. As expected from GIOS simulations (see Report #2, August 7, 1995 of Reference [29]), these tests confirmed that the condition for no energy dispersion depends most sensitively on the field setting of E1.

We used recoils from the reaction of a 100 MeV $^{32}$S beam on a 400 $\mu$g/cm$^2$ $^{29}$Si target. The RMS was run in the converging mode and tuned[2] to accept central recoils of $^{57}$Co with a charge state of $16^+$ and an energy of 44.6 MeV. We varied the field of E1 until we obtained vertical bars in the energy vs. recoil position plot — we had to lower the field of E1 from the value given by the previous

[2] with knob settings of 1 at 0; 2 at 2; 3 at -1; 4 at 0.75; 5 at 0; 6 at 0; 7 at -3; and 8 at 2

Table 12: Data used for obtaining new calibration coefficients for the mass separator dipoles E1, D3, and E2 in tests with recoils. The best field values determined experimentally are listed together with the corresponding theoretical values derived from GIOS calculations. To give a feel for how the field values used for the calibration compare to typical RMS field values, the table also lists the theoretical values for a representative RMS setting used to look at $^{113}$Cs recoils.

| | Calibration Field Value [a] | | $^{113}$Cs Field Value [b] |
|---|---|---|---|
| Element | Experimental | Theoretical | Theoretical |
| E1 (kV) | 46.51 | 46.43 | 58.30 |
| D3 (Gauss) | 3238.8 | 3244.66 | 3870.92 |
| E2 (kV) | 46.62 | 46.43 | 58.30 |

[a] For an RMS central ion setting of $^{57}$Co at 44.6 MeV and charge state $16^+$.
[b] For an RMS central ion setting of $^{113}$Cs at 98 MeV and charge state $28^+$. These recoils are produced in the reaction of a 235 MeV beam of $^{58}$Ni on a 500 $\mu$g/cm$^2$ $^{58}$Ni target.

calibration. For lower E1 values the mass groups tilted to the left (as in "\"), while for higher E1 values they tilted to the right (as in "/"). (Note that this dependence is opposite that predicted in Figure 8 of Report #2, August 7, 1995, of Reference [29].) We then lowered the field of D3 slightly by the amount necessary to bring the appropriate mass group to the optic axis. We did not change the value of E2 from the one that resulted from the previous calibration. Table 12 summarizes the resulting field values used to obtain the new calibration for E1, D3, and E2. The table also shows a comparison with the representative RMS setting to give a feeling for how the values used for the calibration compare to typical RMS values. Since only one point was used for the calibration, we only solved for one of the calibration constants — the scaling factor $B$ from Equation 12.

Note that for the E1 value we obtained by using the ion chamber, we only explored one pair out of the range of possible D3–E2 settings that would bring the appropriate mass group to the optic axis. We confirmed that the pair we chose was the right one by using the new calibration to scale the RMS to central recoil energy settings at $\pm 5\%$ and noting that the positions of the mass groups did not shift. Given the fact that we did so little to explore the space, it is perhaps surprising that we hit upon the "right" pair of D3–E2 settings to match the E1 value. The system may not be very sensitive to the exact choice of this pair. If it is sensitive, a way to account for our luck in getting the right pair is the fact that we chose an E2 value that gave a calibration constant for E2 very similar to that for E1; to first order it seems likely that the calibrations for the two electric dipoles

should be the same since we are not aware of any major differences between the two systems.

We also confirmed the calibration by using recoils from a different reaction and by using beam ions. The different recoils were produced with the same beam and a 300 $\mu$g/cm$^2$ $^{54}$Fe target; the RMS was scaled for 33 MeV $^{83}$Y ions at a charge state of 16$^+$. Beam ions in the 16$^+$ charge state were generated by using a 20 $\mu$g/cm$^2$ $^{nat}$C stripping foil placed at the target position; the RMS was scaled for $^{32}$S ions at a charge state of 16$^+$ and 92 MeV.[3] In going from $^{83}$Y to $^{57}$Co to $^{32}$S, we spanned a range of E1 settings from 34.42 to 46.51 to 95.94 kV and a similar range of E2 settings. We spanned a range of D3 settings from 3362.2 to 3238.8 to 3485.8 Gauss. The fact that we saw a small shift (in about half centimeter steps to the left in going from $^{83}$Y to $^{57}$Co to $^{32}$S) shows that the new calibration is not completely correct. The new calibration is clearly better than the one based on the $\alpha$-particle data; in reactions run since the new calibration was implemented the requested recoil comes much closer to hitting the optic axis at the focal plane.

After obtaining the new E1–D3–E2 calibration, we also increased the scaling of Q3 by a factor of 1.2 based on observations of the mass resolution. It is not clear whether the re-optimization of Q3 was required because of the new E1–D3–E2 calibration, because of the switch to the converging mode, or because of the optimization of the knob settings for the converging mode which took place after the new calibration was made.

Although the present calibration for the mass separator dipoles is as good as it needs to be for now, we may have to make a new calibration when we regularly run the electric dipoles at the higher ends of their operating ranges (up to $\pm$250 kV). Here are some ideas for making further improvement to the calibration by using recoils. One idea is to make a two point calibration covering a wide range of dipole settings and making use of both calibration constants from Equation 12. Such a calibration can perhaps be made with a single target by scaling to mass and charge state values populated in the reaction corresponding to widely different electric and magnetic rigidities. Another idea is to search a large portion of the D3–E2 space for each calibration point by making big changes in D3–E2 pairs that are matched to an optimum E1 setting by changing their values up to several percent.

[3] We had to scale the RMS to an energy significantly lower than that of the 100 MeV $^{32}$S beam because the electric dipoles were not conditioned high enough at the time to handle the full rigidity of the beam particles. We could get away with doing this because the ions still fit within the spectrometer's energy acceptance window for the lower central energy setting.

This exercise should give us a better feel for whether or not we are choosing the best pair of D3–E2 settings for the optimum E1 setting and for how critical this adjustment is. Another check is to make sure that the method we are using to calibrate is not somehow coupled to the setting of Q3; if it is, we need to come up with a way for setting Q3 together with E1–D3–E2 to end up with the optimum overall calibration. Before taking the trouble to make a new calibration, it is also worth rechecking the alignment of the PSAC. Not only has it been several years since the alignment has been checked, in which time there has been much activity at the focal plane that could have shifted things, but also the alignment has never been checked for the forward (43 cm) PSAC position used in the converging mode.

The discussion in the remainder of this section tries to make explicit the assumptions we have used in the calibration and to show that there may be another way of understanding what is going on in the system. In future attempts to improve the calibration it is certainly worth making some simple tests to try to figure out which way of understanding the system works the best. It may well be the case that the test for discriminating between the two scenarios is inconclusive, and, thus, the differences between them do not matter. The main point of this discussion is to illustrate the kind of thinking that we have gone through as we try to better understand the RMS.

There are at least two ways of interpreting the E1–D3–E2 calibration exercise discussed here. *Possibility I:* We are matching the separator dipoles to the setting of dipoles D1 and D2. *Possibility II:* We are matching the E1–D3–E2 settings to the absolute central energy of the recoils — which is defined by the target thickness — and not to the momentum achromat settings. A test to distinguish between the two possibilities is to vary the energy scaling of the momentum achromat elements while leaving the settings of the mass separator elements unchanged. The appearance of tilting mass groups in the energy vs. recoil position spectra would support Possibility I: that in fact the mass separator dipoles (in particular, E1) were matched to the original momentum achromat settings. The mass groups remaining vertical would support Possibility II: that the E1 setting is sensitive to the energy of the recoils defined by the target thickness (and, thus, the response of the separator dipoles to the recoil energy does not depend sensitively on the energy scaling of the momentum achromat elements). A confirmation of this conclusion would be the observation of tilting mass groups in response to switching to a target of a different thickness (or in response to rotating

the original target by 45° to increase its apparent thickness).

*Possibility I.* Let us assume that the calibration matches the separator dipoles to the momentum achromat settings. The fact that we have a high degree of confidence in the scaling of the momentum achromat dipoles from the beam calibration means that we now also have a high degree of confidence in the resulting setting of the separator dipoles to a known energy: 44.6 MeV. We can therefore have full confidence in the calibration constants derived from the theoretical GIOS numbers which are based on the 44.6 MeV energy value and are listed in Table 12. The usual problem of not knowing with certainty the central energy of the recoils we are using (because of the difficulty of knowing the actual target thickness) means that the RMS central ion setting we used to obtain the calibration may not be optimized to the actual central energy of the recoils. An optimized setting can be obtained simply by scanning the RMS central energy setting based on the new calibration constants. The resulting best energy setting should indicate the actual absolute central energy of the recoils.

*Possibility II.* Let us assume that the calibration matches the separator dipoles to the central energy of the recoils. Since we cannot be sure about the target thickness, it may turn out that the central recoil energy to which we have optimized the mass separator dipoles is some value other than 44.6 MeV. If this is in fact the case, we are wrong to use the calibration constants obtained from the theoretical numbers given in Table 12 (which are based on the 44.6 MeV energy value); instead, we should be using theoretical numbers based on the actual central energy. We could perhaps find the central energy of the recoils by scanning the momentum achromat elements in energy while leaving the mass separator elements unchanged to find the setting that best matches the two halves. (Although it is not clear what the signature of the "best matching" energy setting would be, things to look for include optimum transmission, uniform mass resolution across the focal plane, a symmetric $M/Q$ acceptance about the optic axis, and maximum $M/Q$ acceptance.) Since we are confident about the absolute scaling of the momentum achromat dipoles, the best matching energy from these would indicate the correct recoil central energy to use for calculating the theoretical values listed in Table 12 which are in turn used to use for determining the calibration constants for the mass separator dipoles.

Table 13: Chronological summary of changes in the RMS calibration.

| Calibration | Date Implemented | Comments |
|---|---|---|
| first | August, 1996 | initial dipole calibration with $\alpha$-source;<br>quadrupole calibration from knob re-normalization |
| second | May, 1998 | D1–D2 calibration with beam |
| third | March, 1999 | E1–D3–E2 calibration based on recoil energy and position;<br>Q3 also adjusted |

History and Highlights

This section puts the calibration efforts discussed in the last few sections into a chronological framework. Table 13 provides a summary of the major RMS calibrations used up through the summer of 1999.

We started making regular use of the converging mode ("mode22" from Report #6, August 28, 1996, of Reference [29]) in November, 1998. Only the third calibration (see Table 13), implemented after November, 1998, was made by using the converging mode. The first and second calibrations are based on work with the diverging mode. Whether the diverging or converging mode is used for calibration, there should be no impact whatsoever on the constants obtained for the dipole elements. Calibrations for quadrupoles and sextupoles were made in the diverging mode (see the first calibration in Table 13).

Table 14 lists the constants defining the first RMS calibration; these constants are based on the data given in Table 8 for the dipole elements and on data from Table 11 for the focusing elements. Table 15 lists the constants defining the second RMS calibration; the new constants are based on the data given in Table 10 from the re-optimization of the momentum achromat dipoles. Table 16 lists the constants defining the third RMS calibration; the new constants are based on the data given in Table 12 from the re-optimization of the mass separator dipoles. (A new scaling factor for Q3 is also given in this table.)

Small differences may be obtained between the optimum values listed in Tables 8, 10, 11, and 12

Table 14: Constants (from the RMS calibration file "rmscali_02.dat") defining the first RMS calibration. These values are based on the data for the dipoles listed in Table 8 and on the data for the focusing elements listed in Table 11.

| Element | Offset [a] | Factor [b] |
|---|---|---|
| Q1 | 84.58 | 1.182287 |
| Q2 | -28.79 | 1.199119 |
| D1 | -0.21 | 0.982743 |
| S1 | -1.30 | 1.249510 |
| Q3 | -2.40 | 1.147092 |
| S2 | -3.41 | 1.215434 |
| D2 | 0.22 | 0.984641 |
| Q4 | -3.16 | 1.199506 |
| Q5 | 2.01 | 1.098342 |
| E1 | 0.05 | 1.016633 |
| D3 | -0.14 | 0.999822 |
| E2 | 0.09 | 1.002037 |
| Q6 | 3.27 | 1.839657 |
| Q7 | 3.87 | 1.277641 |

[a] Calibration constant $A$ from Equation 12.
[b] Calibration constant $B$ from Equation 12.

Table 15: Constants (from the RMS calibration file "rmscali_05.dat") defining the second RMS calibration from the re-optimization of the momentum achromat dipoles in tests with beam. The new values (listed in **bold**) are based on the data given in Table 10.

| Element | Offset [a] | Factor [b] |
|---|---|---|
| Q1 | 84.58 | 1.182287 |
| Q2 | -28.79 | 1.199119 |
| **D1** | **-48.39** | **0.997723** |
| S1 | -1.30 | 1.249510 |
| Q3 | -2.40 | 1.147092 |
| S2 | -3.41 | 1.215434 |
| **D2** | **-41.72** | **0.997630** |
| Q4 | -3.16 | 1.199506 |
| Q5 | 2.01 | 1.098342 |
| E1 | 0.05 | 1.016633 |
| D3 | -0.14 | 0.999822 |
| E2 | 0.09 | 1.002037 |
| Q6 | 3.27 | 1.839657 |
| Q7 | 3.87 | 1.277641 |

[a] Calibration constant $A$ from Equation 12.
[b] Calibration constant $B$ from Equation 12.

Table 16: Constants (from the RMS calibration file "rmscali_09.dat") defining the third RMS calibration from the re-optimization of the mass separator dipoles in tests with recoils using the ionization chamber. The new values (listed in **bold**) are based on the data given in Table 12.

| Element | Offset [a] | Factor [b] |
|---|---|---|
| Q1 | 84.58 | 1.182287 |
| Q2 | -28.79 | 1.199119 |
| D1 | -48.39 | 0.997723 |
| S1 | -1.30 | 1.249510 |
| **Q3** | -2.40 | **1.376510**[c] |
| S2 | -3.41 | 1.215434 |
| D2 | -41.72 | 0.997630 |
| Q4 | -3.16 | 1.199506 |
| Q5 | 2.01 | 1.098342 |
| **E1** | **0.00** | **1.001723** |
| **D3** | **0.00** | **0.998194** |
| **E2** | **0.00** | **1.004092** |
| Q6 | 3.27 | 1.839657 |
| Q7 | 3.87 | 1.277641 |

[a] Calibration constant $A$ from Equation 12.

[b] Calibration constant $B$ from Equation 12.

[c] The calibration factor for Q3 was increased by 1.2 based on the observation of improved mass resolution at the focal plane.

and the field values obtained if the RMS is scaled to one of the calibration point settings with the corresponding calibration in place. These differences arise from the way the control software rounds off numbers in its calculations; these differences are small enough not to be significant.

## Measured Performance

The remainder of this chapter is devoted to a discussion of the performance of the RMS and how the performance was measured. The first calibration from Table 13 was in place for all data presented here. In fact, the calibration coefficients for this first calibration were determined with the same data used to measure energy acceptance, $M/Q$ acceptance, and mass resolution. A discussion of the RMS performance can also be found in References [3] and [4].

### Energy Acceptance

As mentioned in the discussion beginning on page 27, the RMS is designed to have an energy acceptance for recoils of $\pm 9\%$ with some recoils able to make it through with energy deviations of up to $\pm 15\%$. The length of the plates on the electric dipoles, which were designed to handle recoils of high rigidity, limits the RMS energy acceptance. To test the energy acceptance, the central energy setting $E_0$ of the RMS was varied while the central mass and charge state settings $M_0$ and $Q_0$ were kept constant. This test employed recoils from the reaction of a 220 MeV beam of $^{58}$Ni on a 300 $\mu$g/cm$^2$ $^{60}$Ni target. The RMS was set to a value for $M_0$ corresponding to $^{114}$Te and to $Q_0 = 25.5$; $E_0$ was varied from 90 to 116 MeV.

The central recoil energy for this reaction was estimated to be 100.8 MeV by using stopping power calculations to account for the thickness of the target. The fact that the focal plane PSAC count rate peaked at an energy of $102 \pm 2$ MeV confirms the reliability of our calculations. The count rate dropped to 50% of the maximum value at approximately 91 and 112 MeV which confirms the designed energy acceptance.

Figure 16 shows the $x$-projections of the focal plane recoil distributions for the RMS set to central energy values of 90, 103, and 116 MeV, a range which more than spans the nominal energy acceptance. The three spectra were taken over approximately equal time periods. The number of counts in the plot for 103 MeV was higher than the numbers in the other two plots because the energy

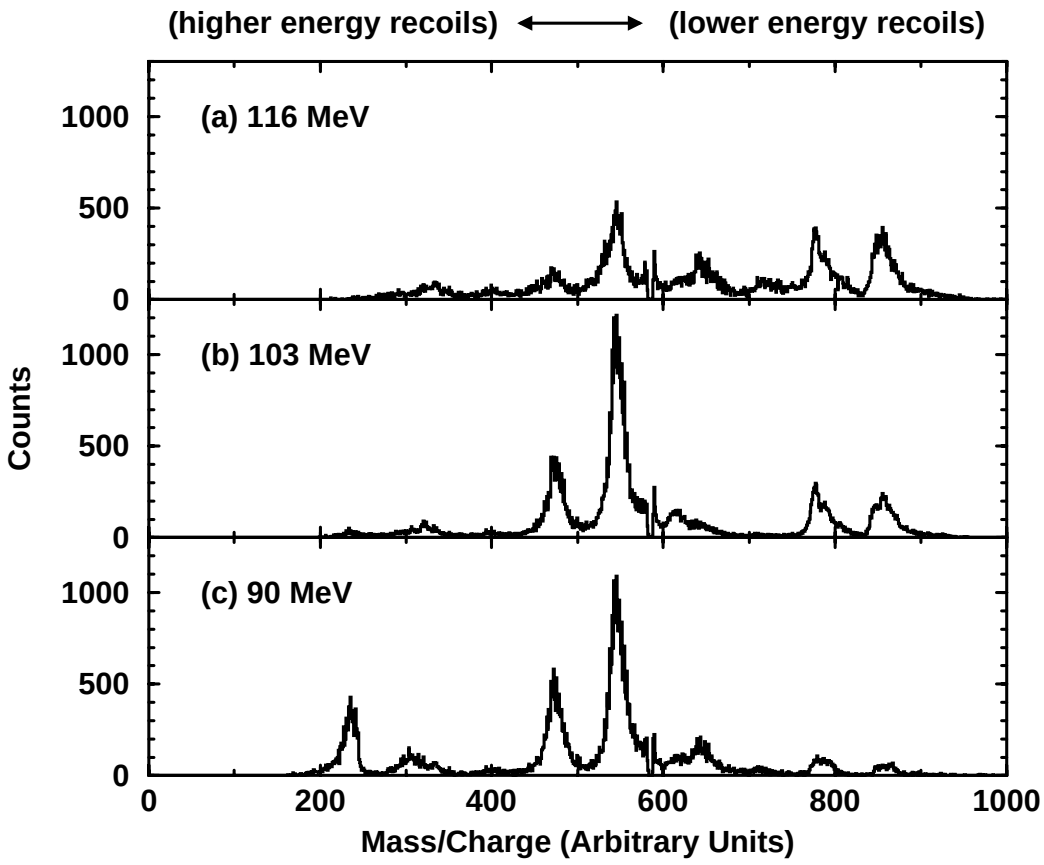


Figure 16: Horizontal projections of the distributions observed in the focal plane PSAC for recoils produced by the reaction of a 220 MeV beam of $^{58}$Ni on a 300 $\mu$g/cm$^2$ $^{60}$Ni target. The RMS was set to central ion values of $M_0 = 113.91$ (corresponding to $^{114}$Te), $Q_0 = 25.5$, and (a) $E_0 = 116$, (b) $E_0 = 103$, and (c) $E_0 = 90$ MeV. The three plots are normalized to have the same total number of counts. The different wings appearing in the plots are discussed in the text.

settings used to produce these other plots are both on the edge of the recoil energy distribution. The 90 and 116 MeV spectra shown in the figure were normalized by multiplying them by factors of 2.44 and 2.56, respectively, so that each of the three spectra have the same number of total counts. The peak centroids do not shift and the peak widths do not change over this large range of energy. The RMS does what it is supposed to do: it delivers recoils of different energies to the final focal plane without dispersing them according to their energy.

Any given RMS central ion setting $M_0$, $Q_0$, and $E_0$ also corresponds to a central value for magnetic rigidity $\frac{M_0 E_0}{Q_0^2}$ and electric rigidity $\frac{E_0}{Q_0}$ (see Equations 4 and 8). According to both of these relations, recoils appearing on the left side of the focal plane will tend to have a *higher* energy distribution than recoils appearing at the center because they typically have mass values $M < M_0$ and/or charge state values $Q > Q_0$. Conversely, recoils appearing on the right side will have a *lower* energy distribution. This discussion accounts for why mass groups appear mainly on the right side of the plot in Figure 16(a): the recoils available to fill the RMS energy acceptance generally have energies lower than the central recoil setting because the RMS is scaled to a central energy that lies above the center of the recoil energy distribution, The same kind of argument explains why mass groups appear mainly on the left side of the plot in Figure 16(c). Thus, in order to obtain maximum yield across the focal plane, the RMS central energy setting should be matched to the peak of the energy distribution of the recoils.

### $M/Q$ Acceptance

Recoils from the reaction of a 220 MeV $^{58}$Ni beam on a 300 $\mu$g/cm$^2$ $^{60}$Ni target were used to measure the $M/Q$ acceptance for the diverging mode of the RMS. The RMS was scaled for central recoils of $^{114}$Te at an energy of 103 MeV and charge state $25.3^+$. Figure 17 shows the $x$-projection of the recoil distribution observed by using the PSAC at the final focal plane.

The RMS is designed to have an $M/Q$ acceptance of $\pm 5\%$. The lower limit of recoils present in the data shown in the figure is 4.27 $M/Q$ and the upper limit is 4.70 $M/Q$. This spread of $\pm 4.8\%$ from a central value of 4.48 $M/Q$ is in excellent agreement with the design value. A comparable $M/Q$ acceptance value was obtained for the converging mode.

The RMS $M/Q$ acceptance is large enough to pass three charge states of a given mass for masses

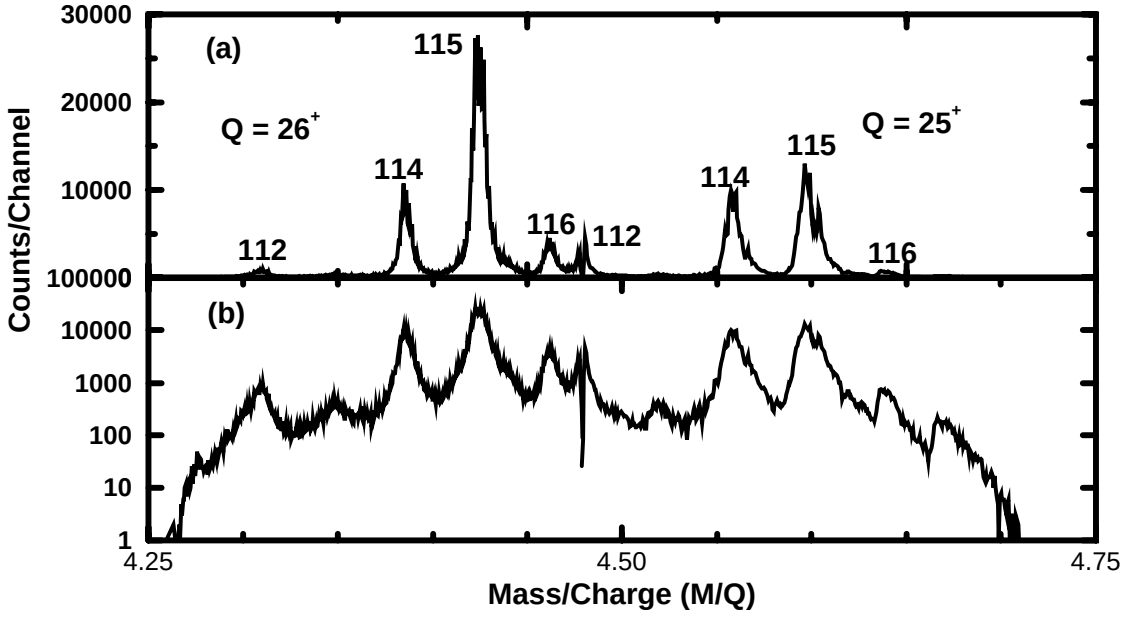


Figure 17: The horizontal projection shown on (a) a linear and (b) a logarithmic scale of the diverging mode recoil distribution at the focal plane from Figure 1. These data lead to the measured $M/Q$ acceptance of $\pm 4.8\%$ and mass resolution $M/\Delta M$ of 470. Recoils are produced in the reaction of a 220 MeV $^{58}$Ni beam on a 300 $\mu$g/cm$^2$ $^{60}$Ni target. The RMS was scaled for central ions of $^{114}$Te at an energy of 103 MeV and a charge state of $25.3^+$.

greater than around 60. (See, for example, Figure 2 where three charge states of the mass 82 recoils appear at the focal plane.) Because the transmission efficiency drops off dramatically for mass groups at the edges of the focal plane, a higher efficiency for a given mass generally results from using two charge states by bringing a charge state to the middle of each half of the focal plane rather than from using three charge states with two lying on the edges of the focal plane. This approach also avoids complications associated with the analysis of data from a mass group placed at the focal plane center related to the fact that detectors such as the ionization chamber and the PSAC are electrically segmented into two halves about the center.

### Mass Resolution

The diverging mode mass resolution for the RMS was measured with the same data from Figure 17 used to measure the $M/Q$ acceptance. The charge state $26^+$, mass 115 peak has a FWHM of 19 channels. This peak is 78 channels away from its mass 114 neighbor. The resulting mass resolution $M/\Delta M$ is 470, which approaches the design value of 540. The mass resolution predicted for the

RMS in Reference [1] exceeds 1000 with the use of an appropriate collimator at the achromatic focus and a software correction to the observed position of the recoils. We obtained the present data without making use of either of these enhancements.

There are two factors external to the RMS performance that affect mass resolution. The first is the target thickness: a thick target or a target with a thick backing will adversely affect the mass resolution because of the increased angular distribution of recoils and of reacting beam particles caused by multiple scattering in the target. The second factor is the quality of beam tune: a beam spot with a wide horizontal distribution of particles will result in correspondingly wide distributions of recoils in the mass groups which degrades the observed mass resolution.

In practice, a mass resolution of around 300 is good enough for most applications of the RMS used so far; thus, for most of the early experiments no special efforts were expended to optimize the mass resolution. The improved mass resolution of the RMS can become important for the study of the most exotic reaction products which have the lowest cross-sections.

## Sample Efficiency

As pointed out in the discussion on page 23, transmission efficiency is not a reasonable quantity to use as a figure of merit to describe a spectrometer's performance because it is influenced by too many external factors. Figure 18 shows the transmission efficiency measured for two isotopes produced simultaneously in a single reaction at the RMS. The reaction used was a 212 MeV $^{58}$Ni beam on a 400 $\mu$g/cm$^2$ $^{28}$Si target with a 900 $\mu$g/cm$^2$ tantalum backing which faced the beam. For each isotope, the efficiency was measured by comparing the counts observed in the $\gamma$-ray peaks in a projection of the $\gamma$-$\gamma$ data recorded by germanium detectors at the RMS target position to the counts in the same peaks in the $\gamma$-$\gamma$ data recorded in coincidence with recoils observed at the focal plane. It was possible to measure the efficiencies for the nuclei $^{80}$Sr and $^{83}$Y by using only a single projection of the two $\gamma$-$\gamma$ matrices because both nuclei contain a strong prompt 595 keV $\gamma$-ray transition. A transmission efficiency of 5.2% was observed for the $3p$ reaction channel ($^{83}$Y) and 4.1% was observed for the $\alpha 2p$ channel ($^{80}$Sr). Two charge states for each mass were used in these efficiency measurements.

This data set emphasizes two important points. First of all, different efficiencies were measured

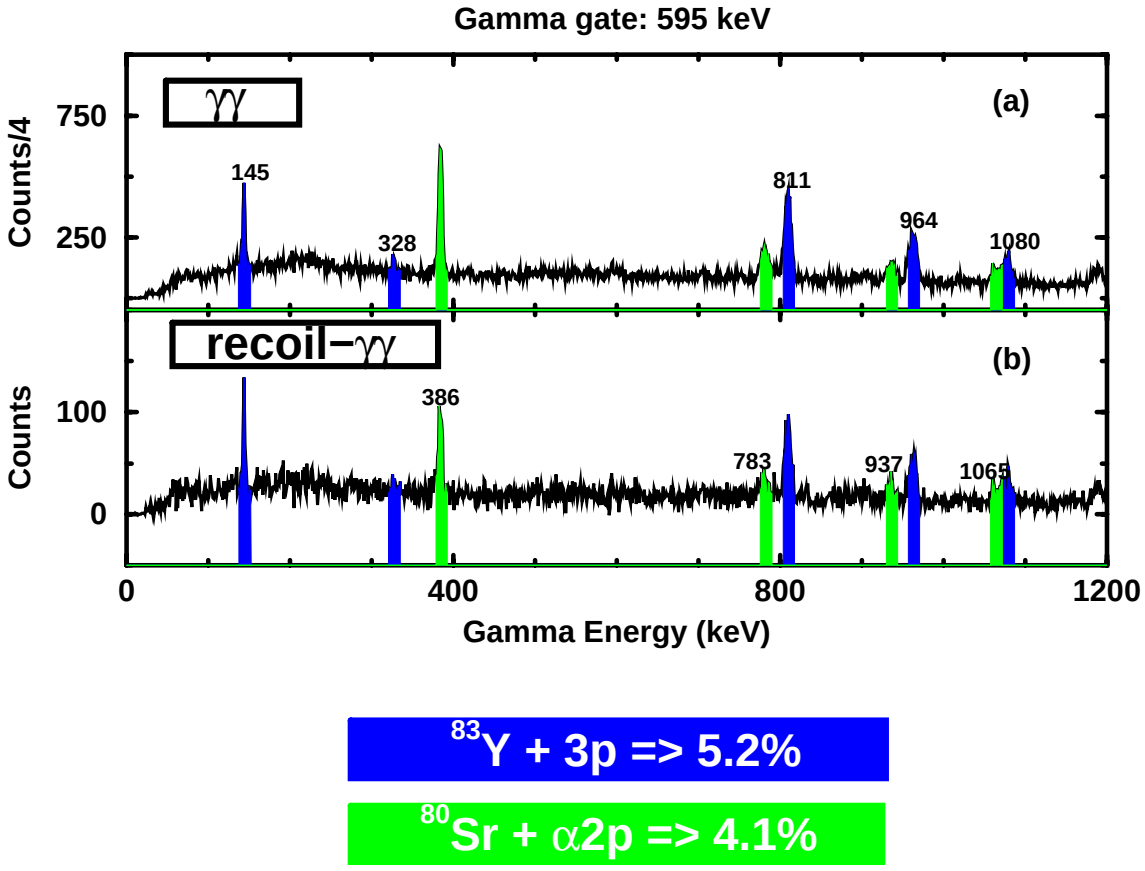


Figure 18: The RMS transmission efficiency measured in the diverging mode for the isotopes $^{80}$Sr and $^{83}$Y. Both isotopes were produced in the reaction of a 212 MeV $^{58}$Ni beam on a 400 $\mu$g/cm$^2$ $^{28}$Si target with a 900 $\mu$g/cm$^2$ tantalum backing which faced the beam. A projection of the $\gamma$-$\gamma$ data from the target position is shown in (a) while (b) shows a projection of the $\gamma$-$\gamma$ data observed in coincidence with a recoil event at the focal plane. Peaks shown in blue are from transitions in $^{83}$Y while those shown in green are from transitions in $^{80}$Sr. Note that the pure $\gamma$-$\gamma$ data was scaled down electronically by a factor of four in order to match better the recoil-$\gamma$-$\gamma$ rate to avoid the need for dead-time corrections.

for the two isotopes even though they were produced under identical conditions. The efficiency varies depending upon the reaction channel used. It does not make sense to use transmission efficiency as a figure of merit to describe a recoil mass spectrometer without specifying all details of the reaction.

The second point of note is that the RMS transmission efficiency remains high even for the $\alpha$ channel in contrast to other recoil mass spectrometers. The usually isotropic emission of an $\alpha$-particle from the compound nucleus usually gives enough of a kick to knock the recoil out of a spectrometer's angular or energy acceptance. The high RMS $\alpha$ channel efficiency results from the spectrometer's large vertical angular acceptance and from the ability to make use of an inverse reaction without flooding the focal plane with scattered beam events.

## Beam Rejection and Fingers

As described in the discussion of the RMS beam rejection capability beginning on page 28, thin metal rods, called fingers, can be positioned along the focal plane inside Q3 to reduce the amount of scattered beam reaching the final focal plane by intercepting beam charge states. The fingers have not been used in routine operation of the RMS because the beam rejection has been so good without the fingers that scattered beam at the focal plane has not been a significant issue for the reactions employed so far. Just having the momentum achromat in front of the mass separator portion of the RMS greatly reduces problems with scattering because the focal plane is roughly four times farther away from the primary beam dump than is the case for other devices and because of the presence of the 90° bend between the primary beam dump and the focal plane. This section discusses the beam rejection performance of the RMS and the results of early tests with the fingers.

### Beam Rejection Without Finger

Figure 19 is a plot taken from Reference [11] demonstrating the beam rejection performance of the Argonne National Laboratory Fragment Mass Analyzer (FMA). For the normal kinematic reaction of a 115 MeV $^{32}$S beam on a 400 $\mu$g/cm$^2$ $^{58}$Ni target, about half the events observed at the FMA focal plane are from scattered beam particles. An energy loss signal obtained from the FMA position sensitive detector was used to separate the beam events from the recoils so that the dispersion of recoils by $M/Q$ would not be obscured by the beam particles.

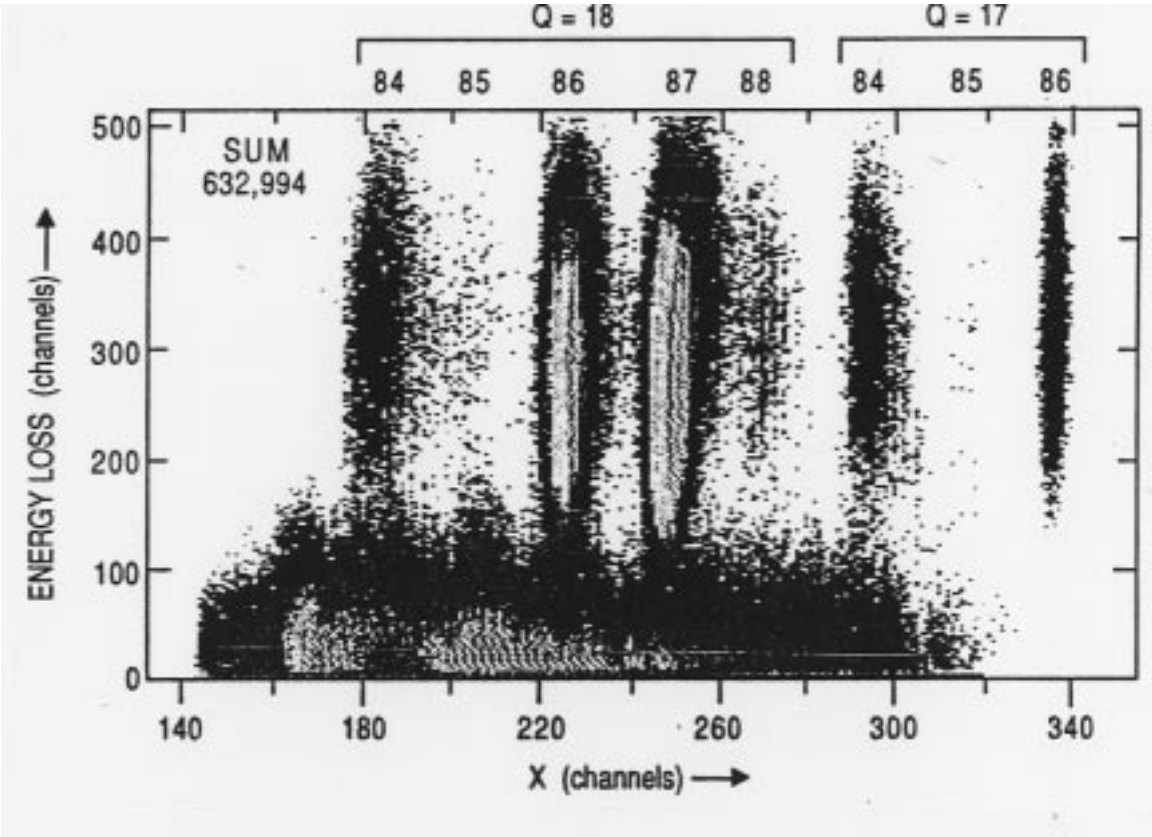


Figure 19: Beam rejection performance of the FMA at Argonne National Laboratory from Figure 7 of Reference [11]. The number of focal plane events are plotted as a function of horizontal position ($x$-axis) and energy loss ($y$-axis) as observed using a position sensitive detector very similar to the RMS PSAC. The recoils occupy the upper groups at higher energy loss, while the lower area represents scattered beam components. The recoil groups are labeled by mass and charge. The total number of counts given for Figure 8 from the same reference, which is an $x$-projection of the recoil events from this plot, shows that about half of the events here are from scattered beam particles.

Figure 1 shows the beam suppression performance of the RMS for the much more demanding case of a symmetric reaction (a 220 MeV $^{58}$Ni beam on a 300 $\mu$g/cm$^2$ $^{60}$Ni target). The $M/Q$ dispersion of recoils in the RMS is not swamped by the presence of scattered beam events; indeed very few of the events can be attributed to scattered beam particles. No gating condition other than the requirement that four position signals be present (one signal from each end of the horizontal and vertical delay lines in the PSAC which generate the event's position) was used to block the appearance of beam events in the position spectrum. In Figure 1 there is no need to employ the energy loss technique of Figure 19 to separate the recoils from the scattered beam events.

Another check of the RMS beam rejection capability is given by the use of an empty target frame at the target position. By using the same beam (220 MeV $^{58}$Ni with a charge state of $12^+$) and the same RMS setting as in the case of Figure 1, no measurable count rate was observed at the PSAC. The beam current of 200 nA or about 17 particle nA (measured at the exit of the tandem accelerator) used for this test corresponds to $1 \times 10^{11}$ ions per second. For a measuring time that lasted more than 100 seconds, this observation at least matches the beam rejection factor quoted for the Rochester RMS of $1 \times 10^{-13}$ [7]. Note that this measurement of performance was made for the more demanding case of setting the spectrometer to accept recoils from a symmetric reaction whereas the Rochester RMS measurements were made only for normal reaction cases.

A sampling of the RMS beam suppression performance was also made with the inverse reaction shown in Figure 2. (The recoils were produced by using the reaction of a 208 MeV beam of $^{58}$Ni on a 400$\mu$g/cm$^2$ $^{28}$Si target with a 900$\mu$g/cm$^2$ Ta backing oriented facing the beam. The RMS was run in the diverging mode and was scaled to accept central ions of $^{84}$Mo at an energy of 113.5 MeV and a charge state setting of $25.5^+$.) The ionization chamber, placed behind the PSAC, was used to measure the energy loss of particles reaching focal plane. Figure 20 shows the energy loss measured for particles on the right side of focal plane. The only difference in the setup for the data shown in Figures 2 and 20 is that for Figure 20 the RMS was scaled to accept central ions of 117.5 MeV instead of the 113.5 MeV setting used for Figure 2.

The events in the lower of the two peaks in the energy loss spectra correspond to scattered beam particles while the events in the upper peaks are from recoils. The beam particles show up in the ionization chamber as having *less* energy than the recoils because the gas pressure in the

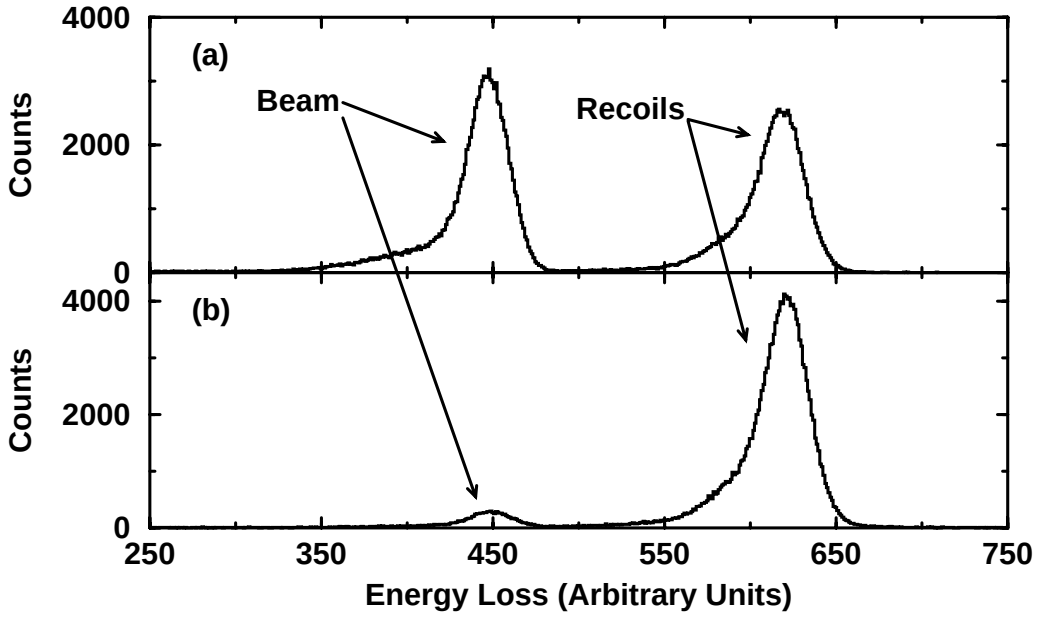


Figure 20: Scattered beam events from an inverse reaction as observed on the right side of the focal plane by using the ionization chamber. (a) A singles spectra of focal plane events. (b) The suppression of beam events obtained by requiring that the focal plane events be observed in coincidence with a $\gamma$-ray at the target.

ionization chamber was optimized for the recoils and, thus, was not high enough to slow the beam particles effectively and to absorb as much of their energy. Figure 20(a) shows the events observed in the ionization chamber when the trigger for the data acquisition is events seen in the PSAC. Figure 20(b) shows the events observed in the ionization chamber when the requirement for the data acquisition trigger is that events in the PSAC have a corresponding $\gamma$-ray event observed with the array of germanium detectors at the target position. By requiring the coincidence between the target and focal plane detectors (effectively, a time-of-flight condition), it is possible to enhance the beam suppression provided by the spectrometer alone because the reactions that produce recoils also generate $\gamma$-rays as the newly produced nuclei de-excite. Some scattered beam events remain in the ion chamber data because of (1) Coulomb excitation, which also produces $\gamma$-rays at the target and (2) random coincidences.

For this inverse reaction, the beam rejection provided by the RMS alone is not at all bad: only 83,000 out of the roughly 172,000 events or 48% entering the data acquisition system from the right side of the focal plane are scattered beam events. (For both sides of the focal plane together, the numbers are 191,000 beam events out of 339,000 total events or 56%.) The fingers were not used

for this reaction because the momentum spread produced by the thick target fronting makes them ineffective. By making use of the coincidence requirement of Figure 20(b), the fraction of scattered beam events entering the data acquisition drops to 5% (7,000 out of 140,000 events) for the right side of the focal plane and to 7% (17,000 out of 256,000 events) for the focal plane as a whole.

Figure 21 shows the horizontal distribution of scattered beam events in the focal plane by plotting the number of projectiles observed as a function of energy and position. This plot was made from the same data set used to generate Figure 2. Scattered beam events account for roughly 10% of the data in this set.

Initial Test of Fingers

The fingers are seven 2 mm diameter rods that can be moved independently to any position across the momentum focal plane in the middle of Q3. For inverse reactions the fingers can be used to prevent beam particles from reaching the final focal plane. For very inverse reactions, in which high charge states of the beam fall directly within the RMS acceptance for recoils, the fingers are very important.

An initial test of the fingers was carried out by using the inverse reaction $^{12}$C($^{58}$Ni,$xpyn$) with a beam energy of 220 MeV and a target thickness of 150 $\mu$g/cm$^2$. The RMS was scaled for central ions of $^{64}$Zn at a charge state of 22.3 and an energy of 176 MeV. A silicon detector at the target position provided a monitor of the beam count rate. The test involved only the RMS elements in front of the achromatic focus where the mini-PSAC was placed to detect the profile of recoils and scattered beam particles. As illustrated in Figure 22 two groups of particles corresponding to two beam charge states were observed at the achromatic focus. The beam events completely dominated the few recoil events produced.

Figure 22(b) shows the count rate observed at the mini-PSAC (divided by the beam monitor count rate to normalize for beam intensity fluctuations) as a function of the position of a single finger along the momentum focal plane. (The finger moves from right to left across the focal plane as the distance units on the plot increase.) The two dips in the count rate indicate the positions of the focused $24^+$ and $23^+$ beam charge states.

Figure 22(a) shows two $x$-projections of beam particle positions as observed in the mini-PSAC.

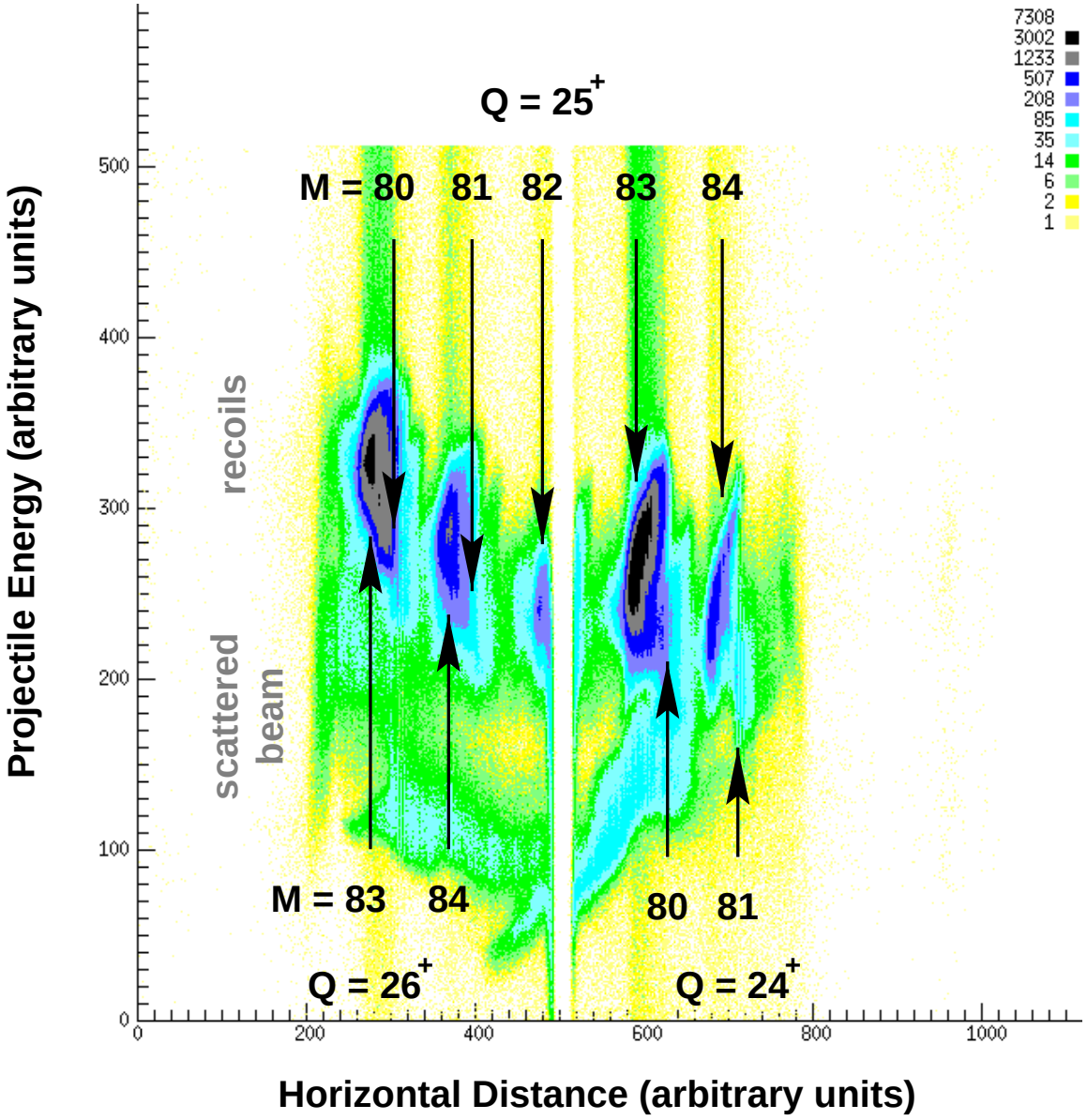


Figure 21: Distribution of projectile events at the focal plane as a function of energy (measured using the ionization chamber) and horizontal position (measured using the PSAC) for the data shown in Figure 2. The color code at the upper right corner of the plot gives the number of events observed at each point. Note that the scattered beam particles appear as lower energy events at the bottom of the plot and are not localized in $x$-position. Scattered beam events account for roughly 10% of the data in the set. This plot somewhat helps to resolve the mass ambiguities from Figure 2. The gap in the center of the figure is an artifact of the data display and does not represent a blind spot in the detector.

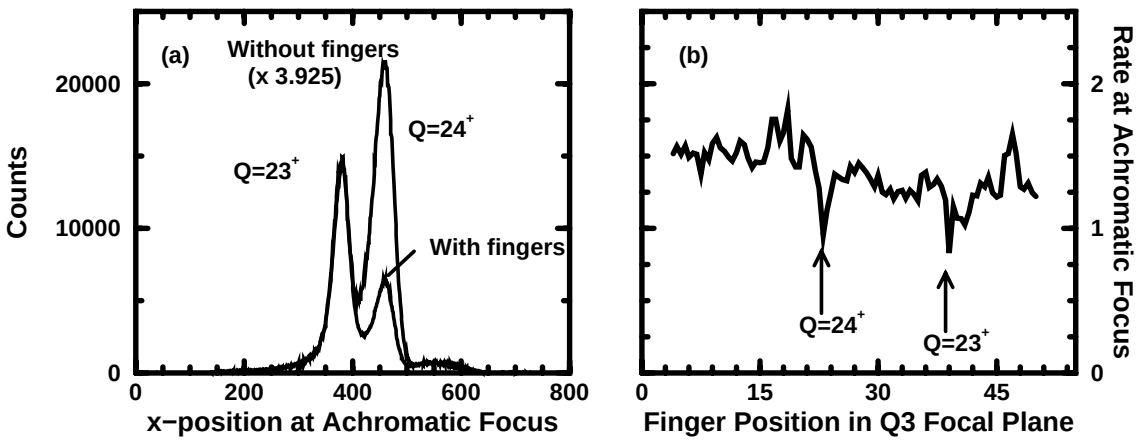


Figure 22: (a) Horizontal projections of particle positions observed at the achromatic focus with the mini-PSAC from the reaction of a 220 MeV $^{58}$Ni beam on a 150 $\mu$g/cm$^2$ $^{nat}$C target. The peaks in each of the projections are from the $23^+$ and $24^+$ charge states of the beam. The use of two fingers to block the $24^+$ charge state reduces the counts in the corresponding peak by a factor of three. (b) The response of the count rate (normalized with respect to beam intensity) observed with the mini-PSAC at the achromatic focus as a finger is moved across the momentum focal plane. (One inch equals 6.4 units on the $x$-axis.)

The peaks on the right are from the $24^+$ charge state and the peaks on the left are from the $23^+$ charge state. The spectra are normalized to the counts in the peak from the $23^+$ charge state. By using two fingers to block the $24^+$ charge state, we have reduced the number of counts in the corresponding peak by a factor of three. Use of a thick target will introduce enough of a spread in the momentum of the scattered beam particles to reduce the effectiveness of the fingers.

# CHAPTER IV

## RESEARCH WITH THE RMS

We have examined the important role played by recoil mass spectrometers in nuclear structure research both for in-beam and decay studies. We examined one new device in particular — the HRIBF RMS — looking in detail at how it works and how it was commissioned. In this chapter we direct our attention to some of the science performed with the RMS that illustrates its power and success as a research tool. We begin with a summary of the detector systems in use at the RMS. We then look at selected results presented in the context of the detection strategies used. We next examine more closely one of the most active areas of RMS research: proton emission studies. We conclude with a detailed consideration of two particular proton emitters: $^{150}$Lu and $^{146}$Tm.

### RMS Detector Systems

The RMS $M/Q$ separation and beam suppression alone cannot provide the high channel selectivity necessary for studying nuclei far from stability. The high sensitivity comes from the detector systems used together with the RMS. Much of the discussion contained in this and the following section was also presented in Reference [30].

Presently detectors are placed at two RMS locations. The first is the target position to detect prompt radiation as the nuclei are being produced. The second location is the focal plane where the mass separated nuclei are detected by energy loss or radioactive decay.

An array of germanium detectors, CLARION (CLover Array for Radio-active ION beams), consisting of 11 anti-Compton-shielded clover detectors, is currently in place around the target position for in-beam $\gamma$-ray spectroscopic studies. Each clover consists of four germanium crystals; each crystal has a relative efficiency[1] of about 25%. The total relative efficiency for a clover is greater than 150% when the add-back option is used. The absolute photo-peak efficiency of a clover in the array for 1.33 MeV $\gamma$-rays is about 0.2%. Ten of the clovers have segmented electrodes to provide additional

[1] This efficiency is stated relative to that of a standard 3 inch $\times$ 3 inch cylindrical NaI(Tl) crystal, assuming a source of 1.333 MeV $\gamma$-rays placed at a distance of 25 cm.

position resolution to help reduce the effects of Doppler broadening.

The electronics to process the signals for each clover detector and its BGO anti-Compton shield is housed in a 4-slot wide CAMAC module equipped with FERA readout. This module includes amplifiers, constant fraction discriminators, four high resolution 14-bit ADCs for the energy from each clover crystal, four low resolution 12-bit ADCs for energies from the three segmented electrodes and the BGO sum energy, and five 12-bit TDCs. The modules feature computer control of functions such as pole-zero adjustment and threshold settings, and multiplexed output of timing and energy signals for inspection with an oscilloscope.

Early work was done with six clovers from the array without the anti-Compton shields. These experiments were run with electronics from the old Oak Ridge CSS germanium array.

HYBALL, an array of charged particle detectors similar to the Microball system [31] used with GAMMASPHERE, is nearing completion for use at the RMS target position. More details about HYBALL can be found in Reference [4].

The detector configurations used at the focal plane usually employ a position sensitive avalanche counter (PSAC), which detects the spatial separation of nuclei by $M/Q$ produced by the RMS. The PSAC covers an active focal plane area of 36 cm (horizontal) by 10 cm (vertical). Details on the PSAC design and construction can be found in References [2, 3, 4, 32, 33]. Details on the mini-PSAC (a smaller version of the PSAC which has been used at the Q3 momentum focal plane, the achromatic focus, and the final focal plane and which has an active area of 6 cm $\times$ 6 cm) can be found in Reference [34].

An ionization chamber may be placed behind the PSAC to provide $Z$-identification of the recoils within a mass group based on their energy loss. The ionization chamber is placed about 10 cm downstream from the PSAC. It is large enough to accept most of the mass groups entering the PSAC when the RMS is run in the diverging mode (compare Figures 2 and 21) and all of the mass groups when the RMS is run in the converging mode. Details about the ionization chamber can be found in Reference [4].

Another detector which may be placed behind the PSAC at the focal plane is the double-sided silicon strip detector (DSSD) which is used to study the decay of implanted recoils by $\alpha$ or proton emission. The DSSD covers an area 4 cm $\times$ 4 cm centered on the optic axis. When the RMS is run

in the diverging mode this detector is placed some 30 cm downstream from the PSAC and accepts one or two mass groups. When the RMS is run in the converging mode the DSSD is placed some 80 cm downstream of the PSAC at a position where the recoils are not distributed in $M/Q$; at this position it accepts most of the recoils passing through the PSAC.

A moving tape collector may also be placed behind the PSAC to accept one of the mass groups. Movements of the tape are used either to transport the activity of the implanted recoils to a detector station away from the focal plane or to prevent long-lived activity from building up in front of a detector station placed at the point where ions are implanted onto the tape. More details about the moving tape collector system and the detector systems that can be used with it are given in Reference [35].

## Selected Results Illustrating Experimental Techniques Employed at the RMS

The challenge presented by the study of nuclei far from stability is the extremely low cross-section with which they are produced compared to other reaction channels. This section describes some of the research results to illustrate the experimental techniques used to combine the RMS with its detector systems to study exotic nuclei.

### Recoil-$\gamma$ with Ionization Chamber $Z$-Identification

One technique involves the use of the germanium array at the target position together with the PSAC and ionization chamber at the focal plane. The PSAC and ionization chamber provide $M/Q$ and $Z$ identification of recoils for tagging the gamma rays observed at the target.

This technique was used to provide the identification of prompt $\gamma$-rays in the $N = Z + 1$ nucleus $^{79}_{39}Y_{40}$ [36]. This nucleus was produced using the reaction $^{28}$Si($^{54}$Fe,$p2n$)$^{79}$Y. Figure 23(a) contains a plot illustrating the ionization chamber performance. Gating on the energy loss observed in the ionization chamber for the mass 79 recoils allows one to obtain spectra with the enhanced presence of $\gamma$-rays from the different mass 79 isotopes. It is then possible to obtain a "clean" gamma spectrum for each of the isotopes by doing an appropriate background subtraction. The new level scheme for $^{79}$Y, shown in Figure 23(b), was constructed based on the RMS data together with data from an earlier GAMMASPHERE experiment that did not employ a mass separator. The transitions

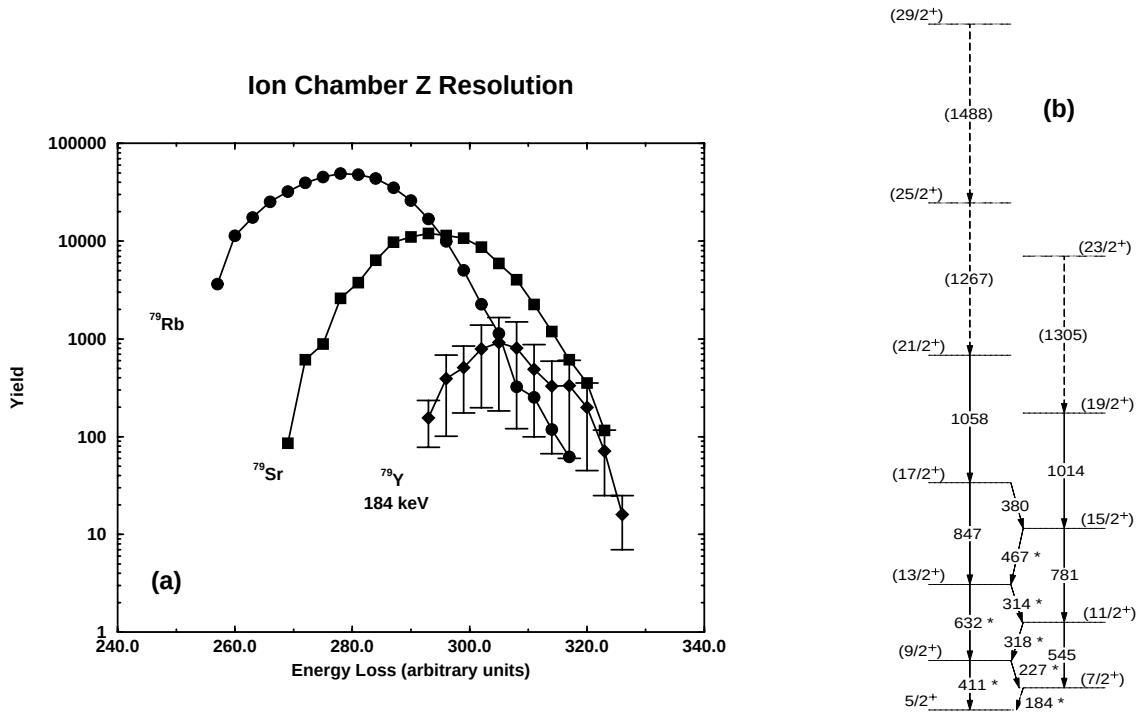


Figure 23: Identification of prompt $\gamma$-rays in $^{79}$Y. These results are from Reference [36]. (a) Ionization chamber energy loss spectrum for mass 79 recoils obtained by gating on known $\gamma$-rays in $^{79}$Rb and $^{79}$Sr and on the newly identified 184 keV $\gamma$-ray in $^{79}$Y. (b) New level scheme for $^{79}$Y from the RMS experiment together with an earlier GAMMASPHERE experiment. The transitions marked by "*" were observed in the RMS experiment.

marked by "*" were observed in the RMS experiment and could be uniquely assigned to $^{79}$Y. From the GAMMASPHERE experiment alone, it would have been difficult to extract this level scheme out of the data and impossible to assign the $\gamma$-transitions unambiguously to $^{79}$Y. The main result of the $^{79}$Y study is that proton-neutron correlations, which are expected to be important for $N \sim Z$ nuclei in this region, did not need to be invoked explicitly in theoretical models to adequately describe the data.

### Charged Particle Decay Studies Using a DSSD

Another class of experiments involves using the DSSD placed behind the PSAC for proton emission studies. The DSSD consists of 40 horizontal strips positioned in front of 40 vertical strips to provide 1600 individual pixels for detecting recoil implantation events and their subsequent decay by $\alpha$ or proton emission. The large number of pixels means that it is possible to look for the decay of an implanted ion on a comparatively long time scale before a new ion gets implanted into the same pixel. (This time scale, of course, depends on the overall rate at which recoils are implanted into the DSSD.) Results of research to study the decay of nuclei by proton emission using the strip detector are discussed later in this chapter.

### Recoil Decay Tagging

The DSSD (behind the PSAC) can also be coupled to the germanium array at the target. This arrangement makes it possible to use the known $\alpha$ or proton decay of an exotic nucleus observed at the focal plane to correlate with prompt $\gamma$-rays observed at the target. This technique is known as recoil decay tagging (RDT). Even though the nuclei studied using the RDT technique are particle unstable, they have many high energy excited states.

The DSSD-germanium array setup was used to identify $\gamma$-rays in $^{151}$Lu by tagging on its 80 ms proton radioactivity [37]. This nucleus was produced using the reaction $^{96}$Ru($^{58}$Ni, $p2n$)$^{151}$Lu with a beam energy of 266 MeV. Figure 24(a) shows the $\gamma$-rays observed in coincidence with the mass 151 recoils at the focal plane. Figure 24(b), obtained by the further requirement that a proton from the decay of $^{151}$Lu be present (with a background subtraction to eliminate randomly correlated events), shows the $\gamma$-ray spectrum belonging to $^{151}$Lu. This is the first time that $\gamma$-rays from this nucleus

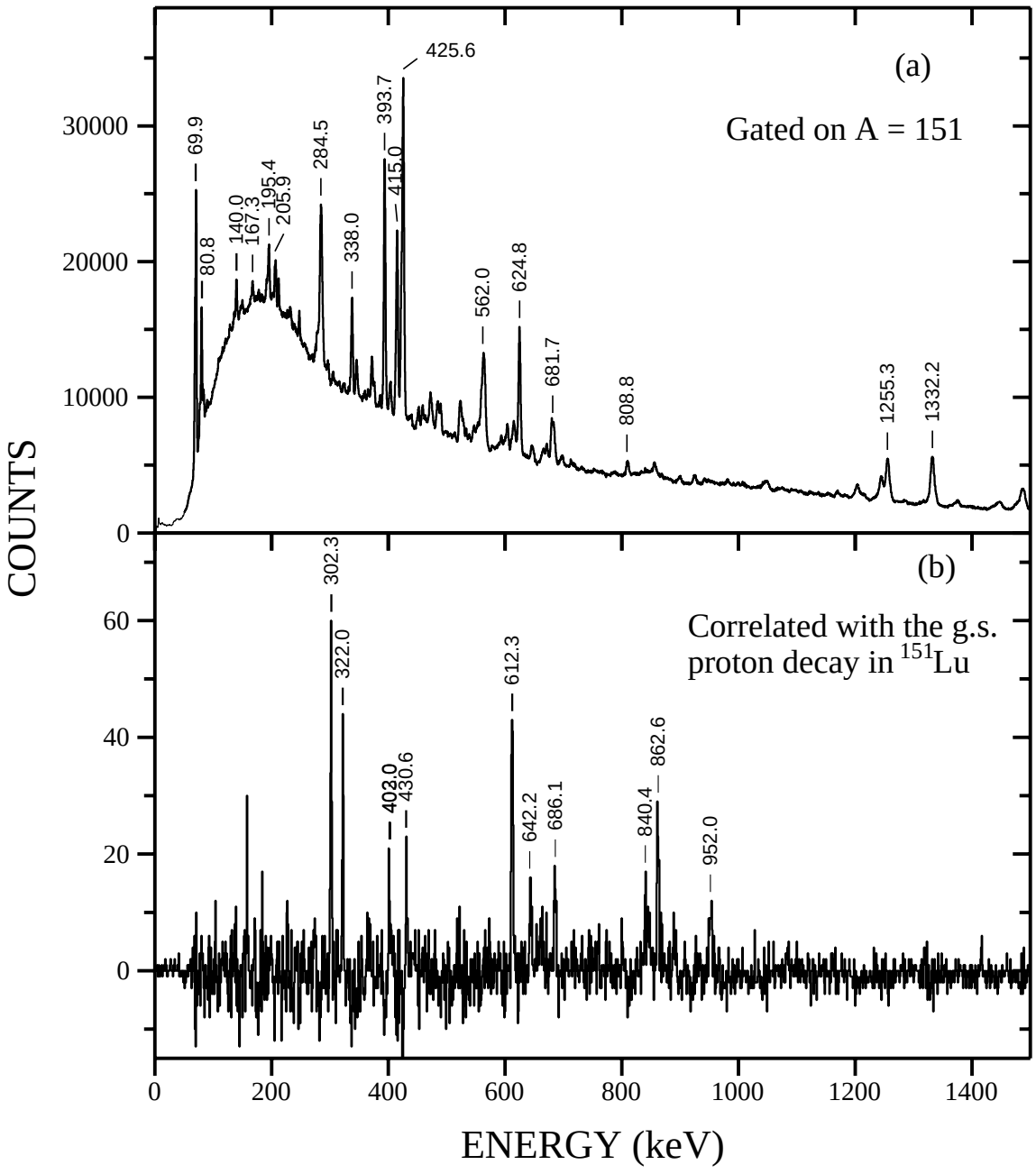


Figure 24: Data from Reference [37] showing the results from the $^{151}$Lu RDT experiment performed at the RMS. (a) Prompt $\gamma$-rays correlated to mass 151 recoils reaching the focal plane. (b) Prompt $\gamma$-rays correlated to the ground state proton emission of $^{151}$Lu observed at the focal plane.

have been observed. An open question left by the experiment is whether the observed prompt transitions feed the ground state or an isomeric state which may be expected on the basis of energy level systematics in neighboring nuclei.

The RDT technique was also used at the RMS to obtain the first identification of prompt $\gamma$-rays in $^{113}$Cs [38]. This nucleus decays by emitting a 0.959 MeV proton with a half-life of $18.3 \pm 3$ $\mu$s.

### Microsecond Isomer Spectroscopy

Another way to extract information about exotic nuclei is to use $\gamma$-decaying microsecond isomers observed with clover detectors placed behind the PSAC at the focal plane. These isomers live long enough to survive the flight time (typically a couple of microseconds) through the RMS. A variety of detector setups can be used depending upon the exact nature of the experiment. The choice between using the moving tape collector or a simple catcher chamber is dictated by the trade-off between the need to remove long-lived activity and the need to maximize detection efficiency by packing more detectors closer to the collection point. The kinds of detectors we have used around the collection point include clover detectors with and without their anti-Compton shields and X-ray detectors.

One option is to perform spectroscopy on the decay of these isomers. A clean spectrum of the isomeric decay is obtained by recording the $\gamma$-rays occurring within a time window of a few tens of microseconds after the arrival of the recoil at the focal plane. The case of the $N = Z$ nucleus $^{66}_{33}\mathrm{As}_{33}$ is an example that illustrates the power of isomer spectroscopy at the RMS. This isotope has two isomers with half-lives of 17 and 1.9 $\mu$s. They were first identified and studied in a fragmentation experiment at GANIL [39]. Fragmentation experiments have the advantage that the isomeric $\gamma$-rays observed can be assigned unambiguously to a given isotope. However, because $^{66}$As is the only nucleus with any microsecond isomers in the $M = 66$ mass chain, the RMS mass separation provides completely clean conditions for studying these isomers as is illustrated in Figure 25. In this instance the overall count rate obtained with fusion-evaporation at the RMS is about a factor of ten higher than with fragmentation.

In cases where the $\beta$-decay of an isotope feeds a known microsecond $\gamma$-decaying isomer, the $\gamma$-rays can be used as a unique tag to study the $\beta$-decay. This technique was applied at the RMS to obtain the first half-life measurement of the important astrophysical rp-process waiting point

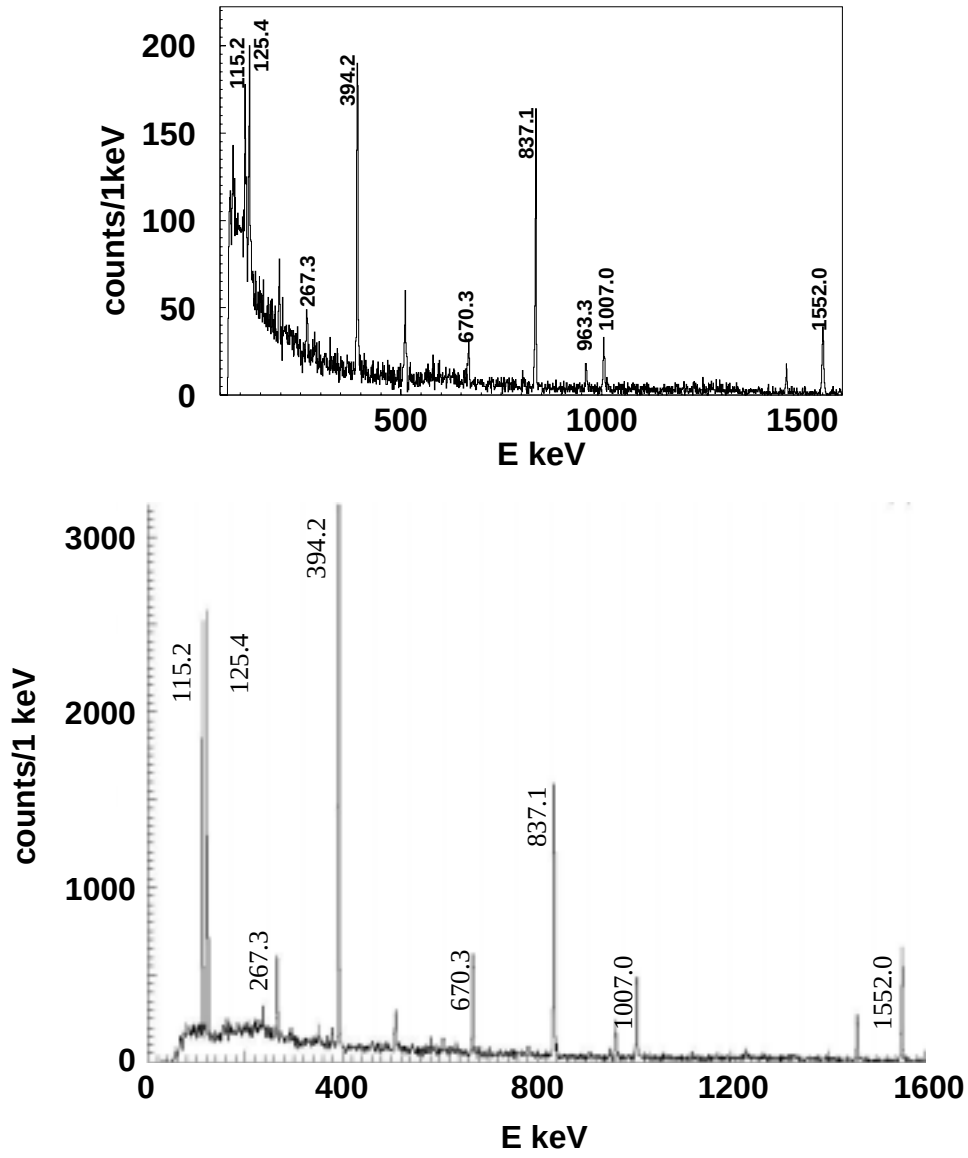


Figure 25: Top: The $\gamma$-ray energy spectrum observed within $\sim$40 $\mu$s of implantation of $^{66}$As fragments during a 96 hour run at GANIL. Bottom: The $\gamma$-ray energy spectrum observed within $\sim$20 $\mu$s of implantation of mass 66 recoils during a 10 hour run at the RMS. Labeled peaks are known $^{66}$As transitions.

nucleus $^{80}$Zr [40].

Another way to make use of a known $\gamma$-decaying isomer is to tag prompt $\gamma$-rays feeding the isomer observed at the target position as in RDT. This technique was applied to the case of $^{66}$As in a very recent experiment at the RMS. The experiment provided the first successful identification of the long-sought prompt $\gamma$-rays from this $N = Z$ nucleus [41].

## Proton Emission Studies

This section provides an overview of some of the insights that studies of direct proton emission have to offer. It focuses on the general proton radioactivity work performed at the HRIBF RMS: the study of short-lived spherical and deformed proton emitters.

### What Can Be Learned

The study of direct proton emission leads to three levels of insight into nuclear matter depending on the quality of the measurements that can be performed. The first level of insight comes by simply measuring the energy of the emitted proton. These energy values make it possible to measure relative isotopic masses in a very remote region of nuclei. These energy measurements are obtained with "trap precision" for nuclei which are too short-lived and which are produced in quantities too small to be measured with current ion trap techniques.

The second level of insight comes with at least a rough measurement of the partial half-life for the emitted proton. For spherical proton emitters, the comparison of such measurements to calculated values makes it possible to tell from which proton orbital the proton is emitted. In this way it is possible to use proton emitters to track the evolution of shell structure and nuclear shapes.

The third level of insight comes with a precise measurement of the proton partial half-life. These measurements make it possible to extract information on the wave function composition of both spherical and deformed unbound neutron deficient nuclei. This point is illustrated for the case of spherical proton emitters where the ratio of the proton partial half-life predicted by theory to that observed experimentally gives the spectroscopic factor $S_p$. The spectroscopic factor is the probability that the corresponding proton orbital in the daughter nucleus is vacant. As illustrated in Figure 26,

a spectroscopic factor near zero indicates that the orbital is full, while a spectroscopic factor near one indicates that the orbital is empty.

## Studies at the HRIBF RMS

As explained in a recent review article on proton emission studies [42], the combination of two new research tools have fueled the explosion in this work that has taken place in the 1990's. The work in the past eight years follows a gap of seven years, beginning in 1984, in which no new proton emitters were identified. One advance was the development of new recoil separators such as the Recoil Separator at Daresbury, the FMA at Argonne, and the HRIBF RMS. These devices bring together good mass resolution and reasonable efficiency. The other advance was the introduction of double-sided silicon strip detectors (DSSD's) into nuclear research. The high pixelization offered by these detectors leads to longer correlation times even in the environment of higher production rates. New developments in the detector technology and electronics made it possible to extract spectroscopic information for the first time from these types of detectors. The combination of DSSD's and recoil mass spectrometers led to an unprecedented level of sensitivity and background rejection for proton studies. This work began in Daresbury at the Recoil Separator; the FMA took over in 1996 after the work at Daresbury stopped. The RMS contributions began in 1997. As a next generation separator, the RMS with its very good beam rejection provides an even more hospitable environment for these studies.

The proton emitters studied so far at Oak Ridge lie in the region just below the $N = 82$ shell closure on the chart of isotopes as is illustrated in Figure 27. The proton (and neutron) shell model orbitals active for this region of nuclei are $s_{1/2}$, $d_{3/2}$, and $h_{11/2}$ as is illustrated for the case of $^{146}$Gd in Figure 28. In this region of nuclei the decay modes that compete with proton emission are electron capture and positron emission. In contrast to the case for isotopes above the $N = 82$ shell closure, decay by $\alpha$-emission does not compete with proton emission.

Obtaining an accurate determination of the proton partial half-life requires a measurement of the branching ratio for proton emission compared to the other decay modes. Unfortunately, the branching ratio for $\beta^+/EC$ decay is difficult to measure. This problem is avoided, however, if the half-life of the decaying state is short enough — on the order of microseconds — so that these other

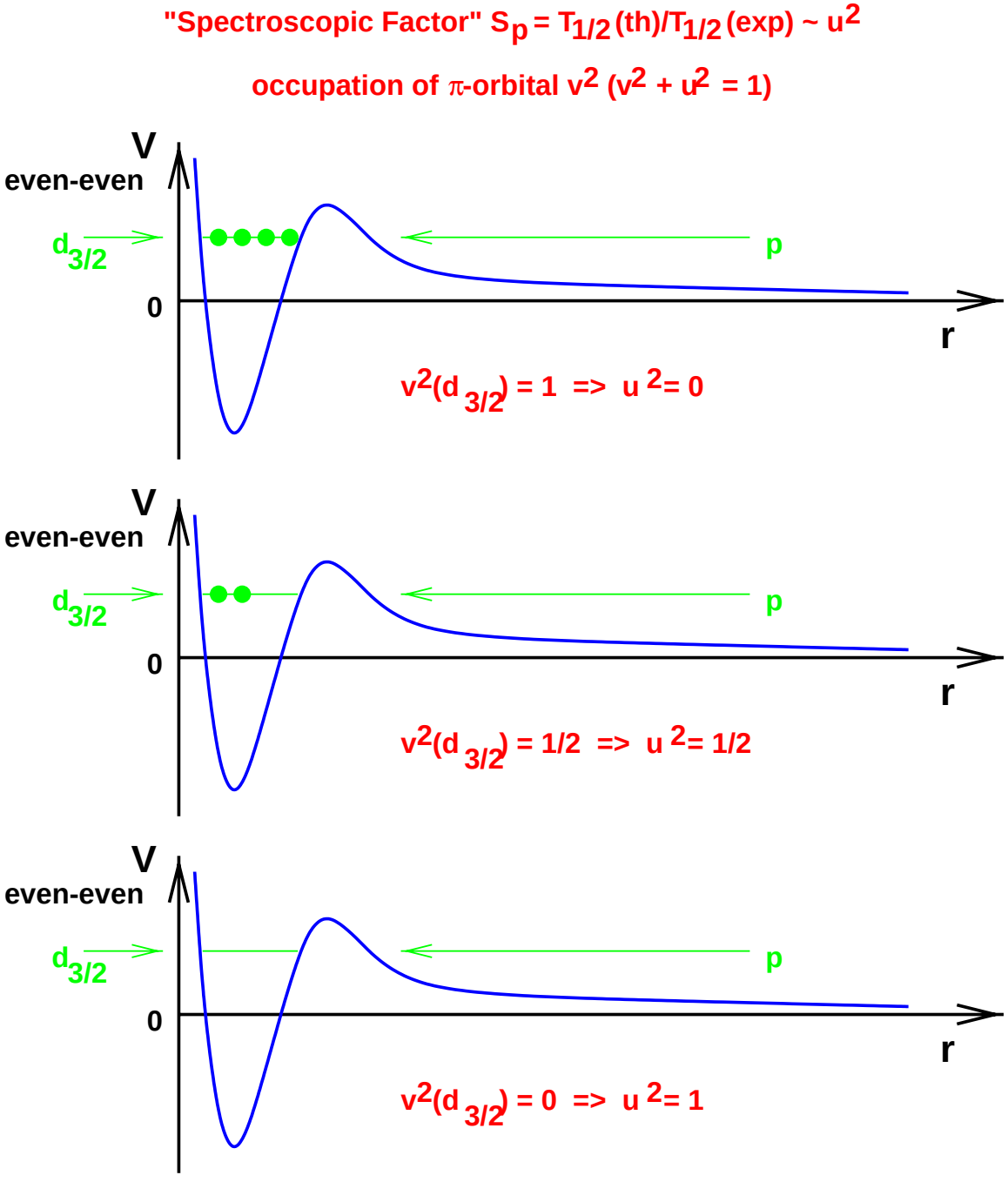


Figure 26: The occupancy of a proton orbital in the even-even daughter of an odd-$Z$, even-$N$ proton emitter illustrated for the case of a $d_{3/2}$ proton orbital with $S_p$ values of 0, 1/2, and 1. A typical depth for the potential shown is ~50 MeV, and the radius range shown is on the order of ~100 fm. Capture of the incoming proton wave is equivalent to proton emission from the odd-$Z$ nucleus.

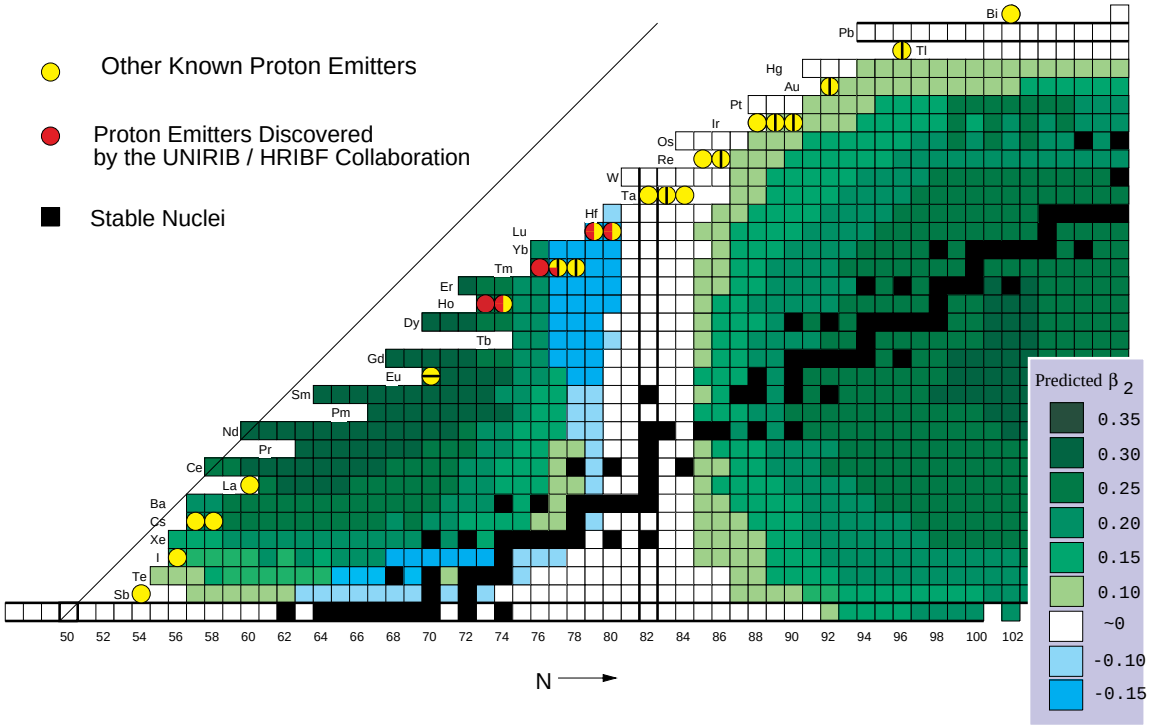


Figure 27: A display of the chart of nuclides which shows the quadrupole deformation parameter [43] together with all of the presently known proton emitters (except $^{53m}$Co). The five proton emitting states discovered so far at Oak Ridge lie in the region of nuclei just below the $N = 82$ shell closure.

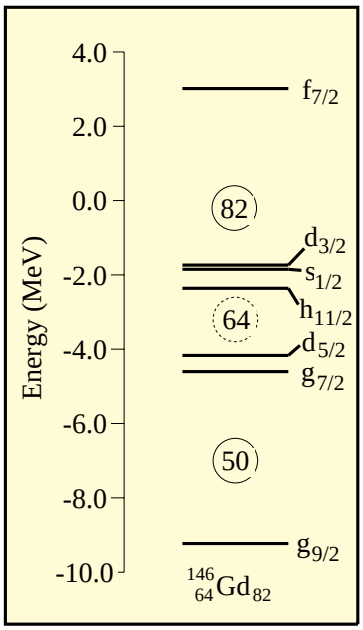


Figure 28: Proton single-particle orbitals in $^{146}$Gd as calculated using the approach presented in Reference [44]. The orbitals active for the nuclei below the $N = 82$ shell closure shown in Figure 27 are $s_{1/2}$, $d_{3/2}$, and $h_{11/2}$.

decay modes do not compete with proton emission. Thus, the observed half-life is essentially the proton partial half-life.

A specialty of the proton emission work at Oak Ridge is the study of short-lived transitions — with half-lives below $\sim$50 $\mu$s. The Oak Ridge collaboration broke new ground in the ability to measure microsecond half-lives by optimizing the data acquisition techniques applied. The group holds the world record for the shortest ground state proton emission yet observed — from $^{145}$Tm with a half-life of $3.5 \pm 1$ $\mu$s [45].

The data readout in the acquisition systems currently being used for DSSD-based proton emission studies can typically take on the order of a hundred microseconds. Therefore, the only way of using these systems to observe a decay occurring just after (down to several microseconds after) the arrival of a recoil is to record the decay in the same data event as recoil implantation. In the readout of the "recoil" ADC's used to record the low gain signals from the higher amplitude implantation events, the data acquisition system generates noise. This noise can trigger false events in the high gain signals which feed the "decay" ADC's used to record the lower amplitude decay events. The Oak Ridge contribution to the study of proton emission was to work out a way of delaying the readout of the recoil ADC's so that only real events would be digitized in the decay ADC's. Recording the implantation and decay data in the same event also required implementing a way of recording two separate signals from the clock corresponding to the recoil and decay parts of the event.

Figure 29 illustrates another issue to be confronted in dealing with decay events which occur within a few tens of microseconds following the implantation of a recoil into the DSSD. The high-gain amplifiers used for feeding the small amplitude decay signal into the decay ADC's become saturated when they encounter the large amplitude signals from the implantation event. These amplifiers can take many microseconds to recover fully. If the decay event occurs before the amplifier recovers, then the energy of the decay (which is given by the amplitude of the decay pulse) is shifted by an amount dependent on the time that the decay follows the implant. A good adjustment of each amplifier's pole-zero setting is important for getting consistent behavior resulting from this effect from one channel to another. Figure 30 shows the dependence of the observed decay energy on time for the fastest decay events in the case of $^{113}$Cs ions implanted into the DSSD with an energy of about 40 MeV. It is possible to correct for this effect by using a pulser or a fast known proton

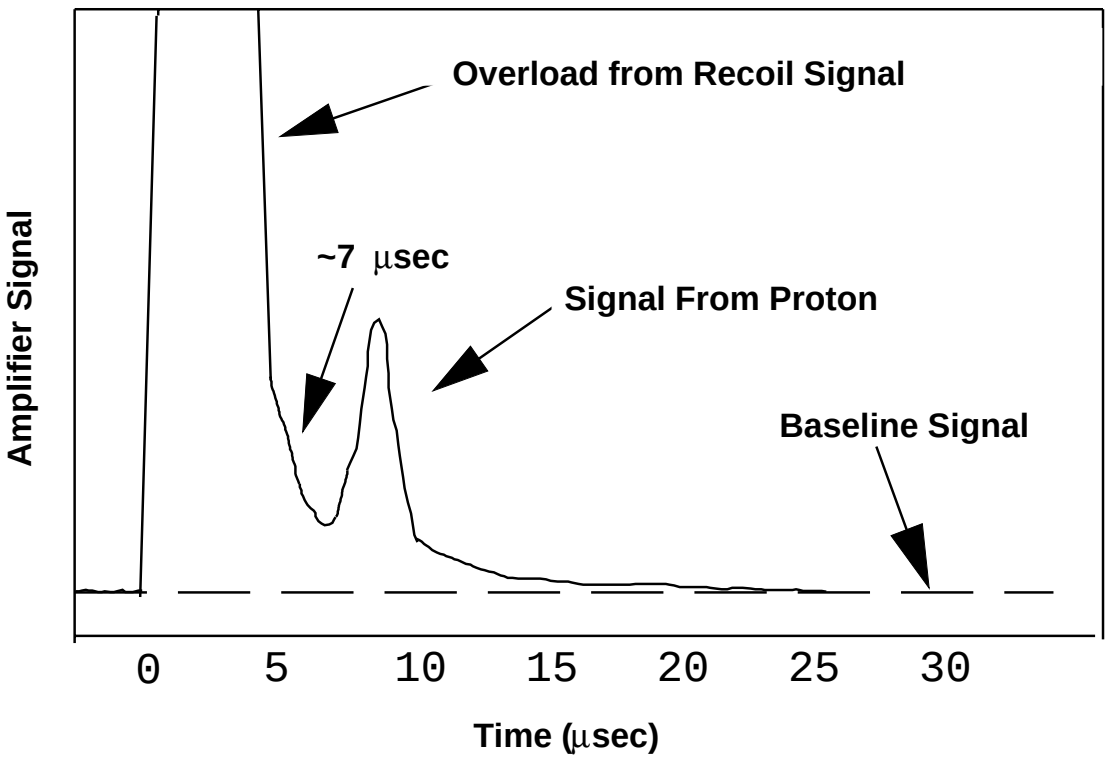


Figure 29: The response of a high-gain amplifier used for measuring decays in the DSSD system to an implantation signal promptly followed by a decay signal.

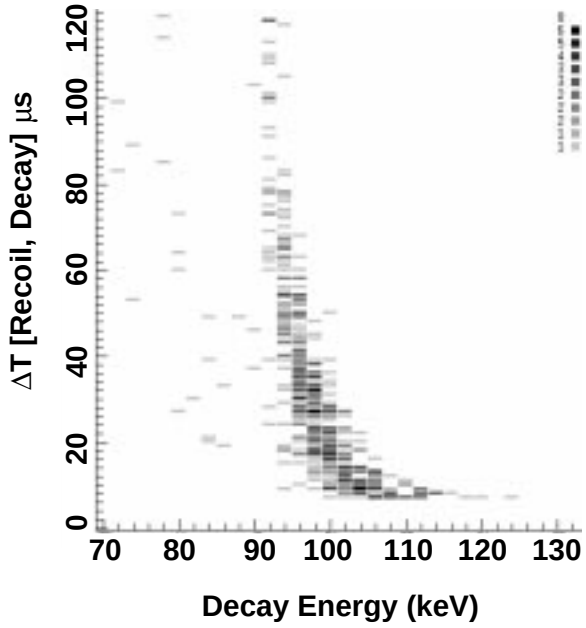


Figure 30: Shift in the observed energy of $^{113}$Cs protons within the first 120 $\mu$s after ions are implanted into the DSSD with an energy of 40 MeV. This data set was used to correct the $^{150}$Lu proton emission data discussed in the section beginning on page 112 and presented in Figure 33(b).

emitter[2] to track the channel by channel response of the system. The extent of the effect in time depends on the amplitude of the recoil signal, which in turn depends on the energy with which the recoils are being implanted.

The first proton work completed at the RMS was the identification of the new isotope $^{145}$Tm via its proton decay ($t_{1/2} = 3.5 \pm 1$ $\mu$s). The next proton study completed at the RMS identified the new isotope $^{140}$Ho [46] via its proton emission with a half-life of $6 \pm 3$ ms. This experiment was the first to employ a $p5n$ reaction channel (with a cross section of only 13 nanobarns) to study proton activity. The same experiment also resulted in the discovery of a proton emitting isomeric state in $^{141}$Ho with a half-life of $8 \pm 3$ $\mu$s. Both of these isotopes are deformed proton emitters. In addition to the RDT study [37] already described for the spherical proton emitter $^{151}$Lu, the same experiment resulted in the identification of a proton emitting isomeric state for the isotope with a $16 \pm 1$ $\mu$s half-life [47]. The remaining sections of this chapter are devoted to the story of the two most recent additions to the Oak Ridge family of proton transitions: one in $^{150}$Lu and at least one $^{146}$Tm.

There are two general results that have come out of the work on proton emitters at Oak Ridge. One result deals with deformed proton emitters. Our research showed that the properties of the proton emitting states in $^{141}$Ho could be understood in terms of the superposition of spherical single-particle wave functions. For $^{141gs}$Ho and $^{141m}$Ho, these states are predominately composed of wave functions from higher $l$ orbitals, but the decay width is dominated by the small admixture of the lowest $l$ component [46].

The other general result deals with the spherical proton emitters. Our work revealed trends in the data for protons emitted from the $d_{3/2}$ and $h_{11/2}$ orbitals: the experimentally deduced spectroscopic factors for the $h_{11/2}$ emitters match the values expected from theory while the spectroscopic factors for the $d_{3/2}$ emitters are consistently below the theoretically predicted values. This result suggests that the $d_{3/2}$ emitting states are mixed (perhaps with the $2^+$ phonon state of the daughter core nucleus coupled to the $s_{1/2}$ proton) while the $h_{11/2}$ emitting states are rather pure.

[2] We frequently use the proton emission from $^{113}$Cs.

The Oak Ridge group will continue its pursuit of short-lived proton emitters with state-of-the-art digital signal processing electronics. The group currently has forty channels of electronics manufactured by X-Ray Instruments Associates which are housed in ten of their single-width DGF-4C CAMAC modules [48]. Signals are fed directly from the DSSD preamplifiers into these modules which are then read into the data acquisition via fast CAMAC readout. The much smaller size and much simpler wiring layout means that the new system should be less susceptible to noise; the resulting lower threshold settings ($\sim$100 keV) should thus enhance the observation of lower energy proton transitions. Presently, the DGF modules can be run in two modes. In one mode, which can be used for decays occurring more than 2 $\mu$s after an ion is implanted, programs running inside the modules extract the small amplitude of the fast decay events riding on the tail of the large implantation signal as well as provide the amplitude of the implantation signal along with the times of the implantation and decay. In the other mode, which can be used for decays occurring in the time range from 100 ns to 25 $\mu$s, the module can be programmed to dump the trace of the signal from the preamplifier out to the data acquisition for later analysis for the interesting events in which a decay promptly follows the implantation of a recoil.

The lower limit on the proton activity half-life observable with the present experimental arrangement is determined by the RMS time-of-flight which is typically on the order of a couple of microseconds because of its 25 m flight path. One idea for getting around this limit is to use the strip detector at the RMS achromatic focus to reduce the time-of-flight by almost a factor of two. Although the recoils are not separated by mass at the achromatic focus, this position should still feature good beam rejection and perhaps an even higher transmission efficiency. Because long correlation times are not required for studying short-lived decays, the added selectivity provided by mass identification becomes less critical in this application. Another idea for getting around the time-of-flight limit is to run experiments at the HRIBF's split-pole spectrograph [49] which can be run in a gas-filled mode to collect all recoil charge states and which has a flight path of only a few meters corresponding to a time-of-flight on the order of 250 ns.

## Proton Emission from $^{150}$Lu

The material contained in this section is taken from a paper [50] accepted for publication. It describes the results of an RMS experiment performed in June, 1998. Proton emission from $^{150}$Lu was studied with a double-sided silicon strip detector placed at the focal plane of the Holifield Radioactive Ion Beam Facility's Recoil Mass Spectrometer. The $^{150}$Lu nuclei were produced in the $^{96}$Ru($^{58}$Ni,$p3n$) reaction at a beam energy of 292 MeV. The half-life of the previously observed proton emitting state at 1.261 MeV was re-measured to be $49 \pm 5$ ms. A new proton emitting state in $^{150}$Lu was observed with a transition energy of $1.295 \pm 0.015$ MeV and a half-life of $30^{+95}_{-15}$ $\mu$s. These values are consistent with an $l = 2$ character for the new proton transition.

### Motivation

Proton emission can serve as a probe for studying the nuclear structure of nuclei beyond the proton drip line. Since an emitted proton must tunnel through a combined Coulomb and orbital angular momentum barrier, the proton emission rate depends sensitively on the energy and angular momentum of the proton. Thus the energy and half-life observed for proton emission can provide information on low-lying single-particle states. Emitted protons serve as a much more sensitive orbital angular momentum probe than emitted $\alpha$-particles because the Coulomb barrier for the proton is lower than for the $\alpha$-particle while the orbital angular momentum barrier is higher (because of the higher reduced mass for the $\alpha$-particle).

The spherical nucleus $^{150}_{71}$Lu$_{79}$ lies just below the $N = 82$ shell closure. It was the first proton emitter to be identified through the $1p3n$ reaction channel [51]. This nucleus was observed to decay with a half-life of $t_{1/2} = 35 \pm 10$ ms by emitting a proton with energy $E_p = 1.261 \pm 0.004$ MeV [52]. By comparing its half-life to values predicted using WKB calculations, the proton is interpreted to carry an angular momentum of $l = 5$ [51, 52]. The recent observation of a second proton transition from $^{151}_{71}$Lu$_{80}$ [47] motivated this search for a second proton emitting state in $^{150}_{71}$Lu$_{79}$. Two states which emit protons have also been observed in both of the nearby odd-odd nuclei $^{146}_{69}$Tm$_{77}$ [53] and $^{156}_{73}$Ta$_{83}$ [54, 55]. The setup at the focal plane of the Recoil Mass Spectrometer (RMS) at the Holifield Radioactive Ion Beam Facility of Oak Ridge National Laboratory is sensitive to proton activities down to the microsecond time scale. See, for example, the cases of $^{145}$Tm ($t_{1/2} = 3.5 \pm 1$ $\mu$s) [45],

$^{151m}$Lu ($t_{1/2} = 16 \pm 1$ $\mu$s) [47], and $^{141m}$Ho ($t_{1/2} = 8 \pm 3$ $\mu$s) [46]. An important feature of proton emitting states with microsecond half-lives is that since the competition from EC/$\beta^+$-decay is negligible, experimental spectroscopic factors can be calculated for these states assuming 100% proton decay branching ratios.

## Experimental Setup

Ions of $^{150}$Lu were produced in the reaction $^{96}$Ru($^{58}$Ni,$p3n$). The 315 MeV $^{58}$Ni beam was supplied by the 25 MV tandem accelerator with an intensity of just under 5 particle nA. The target consisted of 0.54 mg/cm$^2$ of $^{96}$Ru (98% enrichment) on a 2 mg/cm$^2$ gold foil which faced the beam. The energy of the beam entering the Ru layer was about 292 MeV. The total beam-on-target time for the experiment was 50 hours.

Reaction products recoiling from the target were separated into groups at the RMS [1, 3] focal plane according to their mass-to-charge ratio $M/Q$. A multi-wire, gas-filled position sensitive avalanche counter (PSAC) was used to observe the distribution of the mass groups at the focal plane. The RMS was tuned for central recoils of mass $M = 150$, energy 99 MeV, and charge state $Q = 26^+$. After exiting the PSAC, recoils primarily from the $26^+$ mass 150 group were implanted into a double-sided silicon strip detector (DSSD). Some recoils from the neighboring $26^+$ masses 149 and 151 also entered the edge strips of the DSSD. The DSSD had a thickness of 60 $\mu$m and an active area of 40 mm by 40 mm. Forty 1-mm wide vertical strips on one face and forty horizontal strips on the other face provided 1600 independent pixels for detecting the implantation of recoils and their subsequent decays. An event observed in the DSSD was classified as an implantation or decay by whether or not the event was in coincidence with the PSAC. Decays occurring in a time window of 7 to 250 $\mu$s after an implant were recorded in the same event as the implant; decays occurring later than about 350 $\mu$s after an implant were recorded as separate events. More details concerning the use of DSSD's for proton and $\alpha$-particle emission studies can be found in References [18, 45, 47]. A 900 $\mu$g/cm$^2$ aluminum foil placed between the PSAC and DSSD was used to degrade the energy of the recoils entering the DSSD to around 40 MeV.

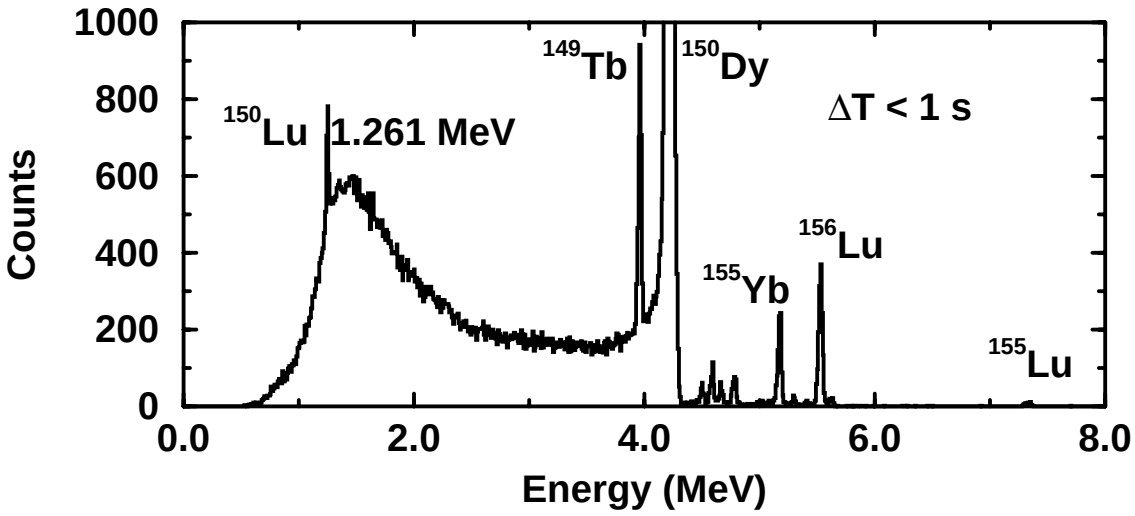


Figure 31: Decays occurring within 1 second after the arrival of a recoil at the DSSD. The peak from the previously observed 1.261 MeV proton transition in $^{150}$Lu is clearly visible.

Results

Figure 31 shows the decay activity observed in the DSSD occurring within one second after an implant; a mass gate has been placed on the recoils observed in the DSSD to reduce the events in the plot originating from masses other than 150. The $\alpha$-particle peaks from $^{155}$Yb and $^{155,156}$Lu arise from isotopic contaminants in the target and appear in the plot because of the $Q = 27^+$ $M/Q$ ambiguity. The peak from the previously observed 1.261 MeV proton emission from $^{150}$Lu is clearly visible in Fig. 31. This peak, together with the 4.233 MeV line from the $^{150}$Dy $\alpha$-decay, was used to provide an energy calibration for the DSSD.

Figure 32 shows the counts observed in the 1.261 MeV proton transition vs. the time between implantation and decay together with a weighted least-squares fit to the data. The data points include a background subtraction (based on the number of events observed within the same time intervals in nearby energy bins) to account for random correlations between implant and decay events. Because of the excellent primary beam rejection of the RMS, the average implant rate per pixel for the experiment was below one event per ten seconds. The previously observed half-life of $35 \pm 10$ ms [52] is consistent with our more accurately measured value of$49 \pm 5$ ms; the new half-life value is based on the observation of 430 proton events compared to about 40 events recorded in the previous measurement.

The preamplified signal from each strip in the DSSD were split and passed to a low gain amplifier

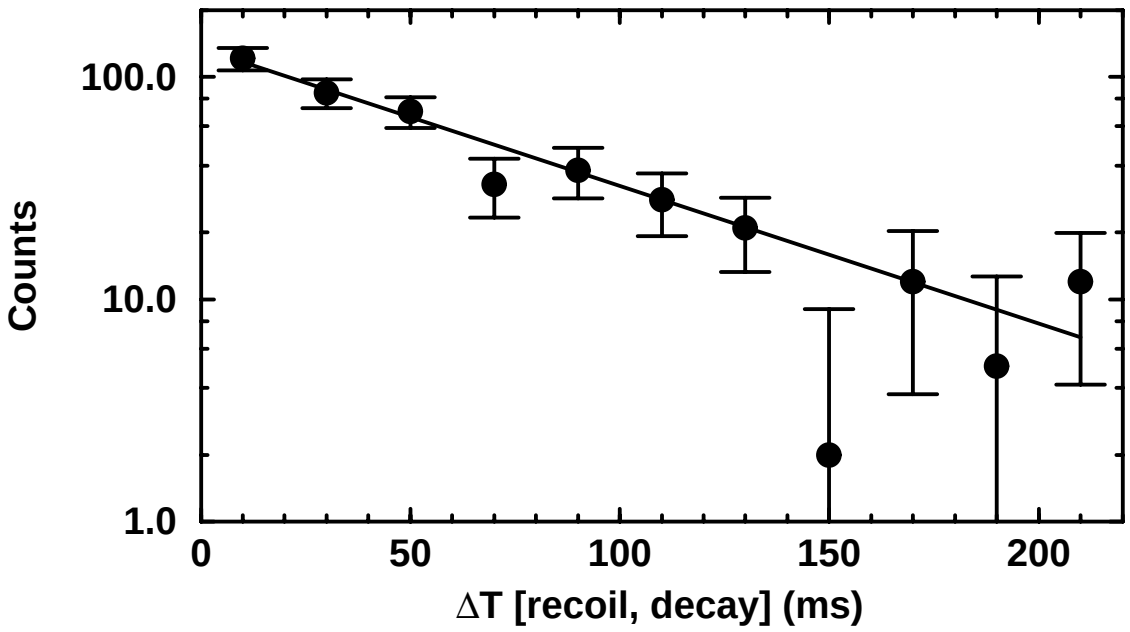


Figure 32: Plot of counts in the 1.261 MeV proton transition of $^{150}$Lu vs. the time between implantation and decay. Also shown is the least-squares fit to the data leading to a half-life value of $49 \pm 5$ ms.

for processing the recoil implantation events and to a high gain amplifier for processing the decay events. References [18] and [56] provide details about the electronics and measuring techniques. The decay amplifiers become saturated when they encounter the large signal from an implantation event (~40 MeV in the present experiment) and can take even up to a few hundred microseconds to recover fully to baseline.[3] For decays occurring within a few tens of microseconds after the implant, the observed decay energy is typically shifted to higher values — the more prompt the decay, the larger the shift — although the exact response with time varies from strip to strip because of the amplifier pole-zero setting. A strip-by-strip software correction for this effect has been applied to the present data for decays following the implantation of recoils up to a time of 100 $\mu$s. This correction is based on the response of the system to the proton emission from $^{113}$Cs ($t_{1/2} = 18.3 \pm 0.3$ $\mu$s [38], $E_p = 0.959$ MeV [57]) obtained from a 7 hour calibration run. (See Figure 30.) The $^{113}$Cs recoils, produced in the $^{58}$Ni($^{58}$Ni,$p2n$) reaction, were implanted into the DSSD with the same energy (~40 MeV) as the $^{150}$Lu recoils. The energy observed in a given strip was shifted by the amount necessary to bring the $^{113}$Cs proton events occuring at similar time intervals after implantation to

[3] Note in Reference [47] that decay events which follow implantation events on a time scale of a hundred microseconds are shifted down slightly in energy compared to decay events occurring at later times — compare the position of the peak in Fig. 1(a) of Reference [47] to that of the lower peak in Fig. 1(c).

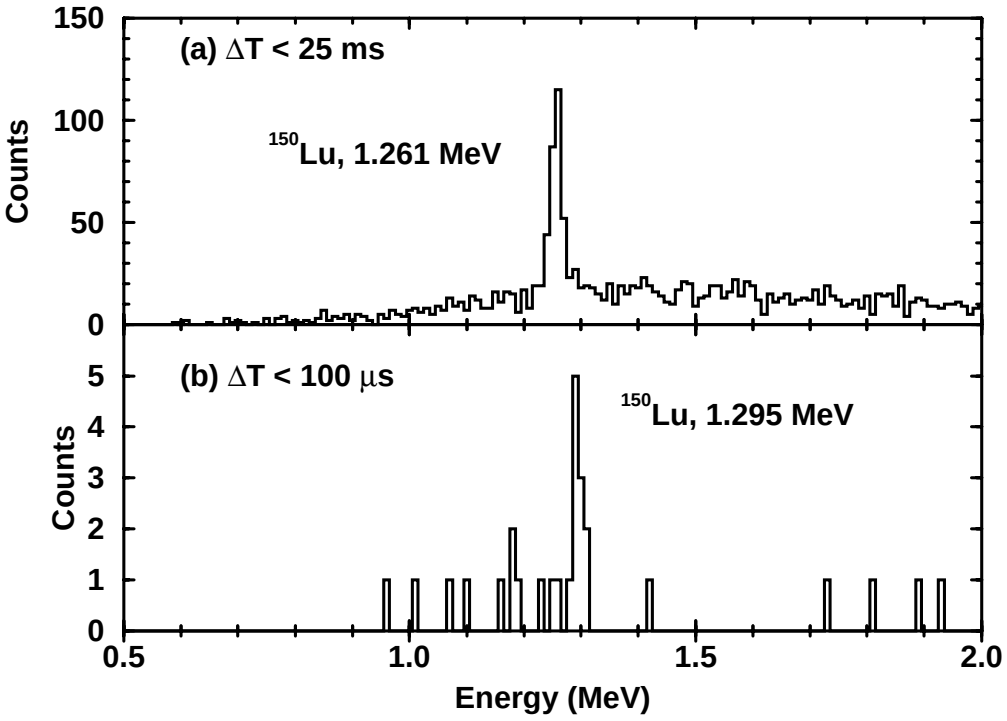


Figure 33: Decays following the implantation of mass 150 recoils into the DSSD within (a) 25 ms and (b) 100 $\mu$s.

their proper energy value. Insufficient $^{113}$Cs calibration data were available to extend the strip-by-strip correction for decay events occuring beyond 100 $\mu$s; however, the observed energy shift is generally small at times greater than 100 $\mu$s.

Figure 33 shows the decay events following the implantation of mass 150 recoils within (a) 25 ms and (b) 100 $\mu$s. Figure 33(a) shows the previously observed proton transition at 1.261 MeV. Figure 33(b) reveals a new short-lived proton transition at an energy of $1.295 \pm 0.015$ MeV. The error bar on this energy measurement has been kept relatively large in view of the low statistics and the difficulties associated with the energy shift of prompt decay events just discussed. Only the decay events following implantation within 80 $\mu$s were used in the energy determination in order to minimize the influence of background events and because of the low statistics at later times of the $^{113}$Cs calibration used to correct the energies. The new decay peak is interpreted as originating

from $^{150}$Lu proton emission since no other $A = 150$ nucleus (or contaminant product) originating in the reaction is expected to be proton unbound [58]. The $Q$-value determined for the new transition is $1.317 \pm 0.015$ MeV.

A half-life of $30^{+95}_{-15}$ $\mu$s was obtained for the 1.295 MeV proton activity by using the method of maximum likelihood (see, *e.g.*, Reference [59]) based on events following implantation within 80 $\mu$s. The large error bars on this measurement reflect the low statistics associated with the new peak.

For the 1.261 MeV proton peak 430 counts were observed, and for the 1.295 MeV peak about 10 counts were observed. Assuming an RMS efficiency of $\sim$3%, these numbers imply a cross section for the 1.261 MeV transition of about 3 $\mu$b and for the 1.295 MeV transition of about 50 nb. These numbers are consistent with the predicted cross section of about 5 $\mu$b for the $p3n$ channel from the HIVAP [16] fusion-evaporation code.

## Discussion

The shell model proton (and neutron) orbitals active in the neutron deficient, $A = 150$ region of nuclei are the $s_{1/2}$, $d_{3/2}$, and $h_{11/2}$ orbitals. Two factors make it difficult to interpret proton emitting states from odd-odd shell model nuclei compared to the case of odd-even nuclei. (1) The odd proton and odd neutron couple to create a state in the parent nucleus with a range of possible spins $I_{pn}$: $I_p + I_n \geq I_{pn} \geq |I_p - I_n|$. (2) The state populated in the odd-even daughter nucleus is one of the neutron single-particle spectator states $s_{1/2}$, $d_{3/2}$, or $h_{11/2}$. It is not a $0^+$ ground state that lies far below any of the excited states, as is the case for the even-even daughters of the odd-even proton emitters. Therefore a determination of the angular momentum carried by a proton emitted from an odd-odd nucleus does not lead to a firm assignment for the spin and parity of the emitting state without additional knowledge about the final state in the daughter nucleus.

By comparing the experimentally deduced partial proton half-lives to values calculated from various models based on the observed proton energy, it is possible to obtain nuclear structure information from the proton emission data. Half-life predictions for the 1.261 MeV transition are given, for example, in References [51, 52, 60, 61, 62]. Following the usual treatment of odd-odd proton emitting states in shell model nuclei (see, e.g., [52, 53, 54, 55]), Table 17 presents the deduced proton partial half-lives for the $^{150}$Lu proton transitions compared to the values calculated by assuming the

Table 17: Comparison of the experimentally determined partial proton half-life values for the transitions in $^{150}$Lu to values calculated using the consistent WKB and the TPA methods [60].

| Observed | | Calculated $t_{1/2,p}$ | | | |
|---|---|---|---|---|---|
| $E_p$ (MeV) | $t_{1/2,p}$ | $0h_{11/2}$ ($\Delta l = 5$) | $1d_{3/2}$ ($\Delta l = 2$) | $2s_{1/2}$ ($\Delta l = 0$) | |
| $1.261 \pm 0.004$ | $72 \pm 7$ **ms** [a] | $33 \pm 3$ **ms** | $17 \pm 2$ $\mu$s | $2.1 \pm 0.2$ $\mu$s | (WKB) |
| | | $30 \pm 3$ **ms** | $17 \pm 2$ $\mu$s | $2.2 \pm 0.1$ $\mu$s | (TPA) |
| $1.295 \pm 0.015$ | $30^{+95}_{-15}$ $\mu$**s** | $15^{+6}_{-5}$ ms | $8^{+3}_{-2}$ $\mu$**s** | $0.9^{+0.4}_{-0.2}$ $\mu$s | (WKB) |
| | | $13^{+6}_{-4}$ ms | $8^{+3}_{-2}$ $\mu$**s** | $1.0^{+0.4}_{-0.3}$ $\mu$s | (TPA) |

[a] See text for a discussion of the quoted error.

protons originate from the $s_{1/2}$, $d_{3/2}$, and $h_{11/2}$ proton orbitals. The deduced partial proton half-life for the 1.261 MeV transition of $72 \pm 7$ ms was calculated from the observed half-life of $49 \pm 5$ ms by assuming a $\beta$-decay partial half-life of 155 ms predicted in Reference [63]; the error on this value was taken simply by scaling the error on the observed half-life. For the 1.295 MeV transition the partial proton half-life is taken to be the observed transition half-life since this value is small enough that the competition from EC/$\beta^+$-decay should be negligible.

Table 17 lists calculated partial proton half-lives obtained from a semiclassical WKB estimate and from the Two Potential Approach (TPA). Note that the WKB estimate used here is slightly different from the formulation presented in the review by Hofmann [64]. The first main difference is that Hofmann's frequency factor $\nu$ assumes a simple square well for the total potential inside the classically allowed region, while our method uses the same combined nuclear plus Coulomb potential in both the classically allowed region and the forbidden (barrier) region. The second main difference is that in Hofmann's approach the parameters of the potential are all taken from the values given by Becchetti and Greenlees [65] without any quantization condition imposed on the WKB wavefunction inside the allowed region. In our approach, the strength parameter of the

spherical Woods-Saxon potential, $V_0$, is taken from the TPA eigenvalue problem. The half-lives calculated in these two different WKB methods sometimes differ by as much as 30% . Details of our "consistent" WKB method and of the two potential approach are given in Reference [60], and the corresponding calculated half-lives are denoted "WKB" and "TPA" in the table. Note that the "consistent" WKB calculations give half-lives that are in very good agreement with the TPA results.

For the 1.261 MeV transition, the experimentally deduced partial proton half-life of $72 \pm 7$ ms is most consistent with the values calculated for an $l = 5$ character. This result implies that the proton is emitted from the $h_{11/2}$ orbital and confirms the previous assignment [52]. For the 1.295 MeV transition, the observed half-life of $30^{+95}_{-15}$ $\mu$s is most consistent with the values calculated assuming an $l = 2$ character implying that the proton is emitted from the $d_{3/2}$ orbital.

If, as suggested in Reference [52], the 1.261 MeV transition originates from the ground state of $^{150}$Lu, and if both proton transitions populate the same state (presumably the ground state) in $^{149}$Yb, then the 1.295 MeV transition originates from a state with an excitation energy of $34 \pm 16$ keV in $^{150}$Lu. Calculations following a spherical macroscopic-microscopic model [44] are consistent with this picture. These calculations indicate that the ground state in $^{150}$Lu results from the coupling of $d_{3/2}$ neutrons to $h_{11/2}$ protons while the excited state results from the coupling of $d_{3/2}$ neutrons to $d_{3/2}$ protons. These calculations also indicate that the ground state in $^{149}$Yb is a $d_{3/2}$ neutron single-particle state.

The TPA half-life calculated for the state from which the 1.261 MeV transition originates, by assuming an $h_{11/2}$ assignment, is $30 \pm 3$ ms. This result leads to an experimental spectroscopic factor $S_p^{exp} = t_{1/2,p}^{th}/t_{1/2,p}^{exp}$ (see [60]) of about 0.42. The uncertainties in the energy and half-life contribute to an error of about $\pm 15\%$. Since the $\beta$-decay branching ratio was not measured, however, this $S_p^{exp}$ value can in principle change substantially. The 0.42 result is close to the expected value of $S_p^{th} = 0.54$ from Reference [60].

Similarly, the TPA half-life calculated for the new state for a $d_{3/2}$ assignment is $8^{+3}_{-2}$ $\mu$s. The calculated half-life leads to an experimental spectroscopic factor $S_p^{exp} = 0.27^{+0.46}_{-0.22}$. Although not at all precise because of the large error bars on the energy and half-life measurements, this result is

less than the theoretical value[4] of 0.73. The reduction of the experimental spectroscopic factor in comparison to the theoretical value is consistent with a general trend observed for the $d_{3/2}$ transitions in odd-even proton emitters and discussed in Reference [47].

A new measurement with higher statistics is needed to obtain more accurate values for the energy and half-life of the the new proton emitting state in $^{150}$Lu. Another motivation for repeating the measurement is the possibility of observing proton transitions to excited neutron single-particle states in the daughter $^{149}_{70}\mathrm{Yb}_{79}$. The experimentally observed level systematics shown in Reference [67] for the $N = 79$ neutron states $s_{1/2}$, $d_{3/2}$, and $h_{11/2}$ suggest that these states, one of which is the ground state, lie within about 200 keV. Given the fact that the proton emitting states in $^{150}$Lu have a range of possible spins from the coupling of the odd proton and neutron, transitions to excited neutron states in the daughter cannot be ruled out. A WKB calculation [60] shows that the branching ratio for a proton transition populating a state 100 keV above the ground state (and of the same configuration as the ground state) would be large — on the order of 10%.

## Summary

In summary, the half-life of the previously observed 1.261 MeV proton transition in $^{150}$Lu ($t_{1/2} = 35 \pm 10$ ms) was more accurately measured to be $49 \pm 5$ ms. Also, a new proton emitting state in $^{150}$Lu was observed with a transition energy of $1.295 \pm 0.015$ MeV and a half-life of $30^{+95}_{-15}$ $\mu$s. These values are consistent with an $l = 2$ character for the new transition suggesting the properties of proton emission from $^{150}$Lu are very similar to those of neighboring $^{151}$Lu [47].

## A Search for Single-Particle States in $^{149}$Yb and $^{145}$Er

The material contained in this section is taken from a proposal [68] submitted to the HRIBF Program Advisory Committee in March, 1999 requesting beam time for an experiment. The request was approved and the results of the experiment are discussed in the next section (which begins on page 128).

We propose to re-investigate the decay of the odd-odd nuclei $^{150}$Lu and $^{146}$Tm to search for

[4] The theoretical spectroscopic factor is given by $u_j^2$, which is the probability that the spherical orbital $(nlj)$ is empty in the daughter nucleus. The theoretical $u_j^2$ value here was obtained following the calculations presented in *e.g.* References [44, 60, 66].

fine structure in the proton emission. The primary aim of this study is to observe the neutron single-particle levels for very exotic even-$Z$, odd-$N$ daughter nuclei populated via proton emission. The proposed experiment represents the first attempt to find fine structure in the proton decay of spherical nuclei. In the first experiments, these known emitters will be produced via the $p3n$ fusion-evaporation channel by using $^{92}$Mo and $^{96}$Ru targets and a stable $^{58}$Ni beam. The HRIBF Recoil Mass Spectrometer (RMS) together with the Position Sensitive Avalanche Counter (PSAC) and a DSSD-silicon particle telescope surrounded by a solar cell veto detector will be used to separate and identify the products and to measure their decay properties. We foresee a continuation of this experimental program with the radioactive $^{56}$Ni beam, which will allow us to use the $pn$ instead of the $p3n$ reaction channel to provide enhanced selectivity for the study of the odd-odd proton emitters.

## Physics Motivation

The decay of odd-$Z$, even-$N$ proton emitters near the magic $N = 82$ gap is well understood in terms of a proton tunneling through the Coulomb and centrifugal spherical potential [60]. The properties of the states involved in the decay process can be deduced from the measured energies and half-lives of proton radioactivities. The observed rates indicate a rather pure $\pi h_{11/2}$ configuration for the $l = 5$ emitters, while the $l = 2$ emitters have a mixed configuration of the $\pi d_{3/2}$ wave function with the proton in the $s_{1/2}$ orbital coupled to the $2^+$ phonon [47, 69]. The latter part of the $I^\pi = 3/2^+$ wave function would dominate the proton decay to the $2^+$ excited state of the even-even daughter nuclei. However, because of the high excitation energy of the $2^+$ state in the daughter nuclei (about 600 keV for the $A \sim 150$ spherical region), this $l = 0$ transition width is dramatically reduced in comparison to the $l = 2$ transition to the ground-state. With the presently available experimental production rates, fine structure in the proton emission from these exotic nuclei is therefore unobservable. The information on the even-even daughter nuclei gained from the proton emission studies is limited to the relative energy of the $0^+$ ground-state and its proton occupancy factor.

In principle, the study of the proton-decaying odd-odd nucleus can offer more information on the

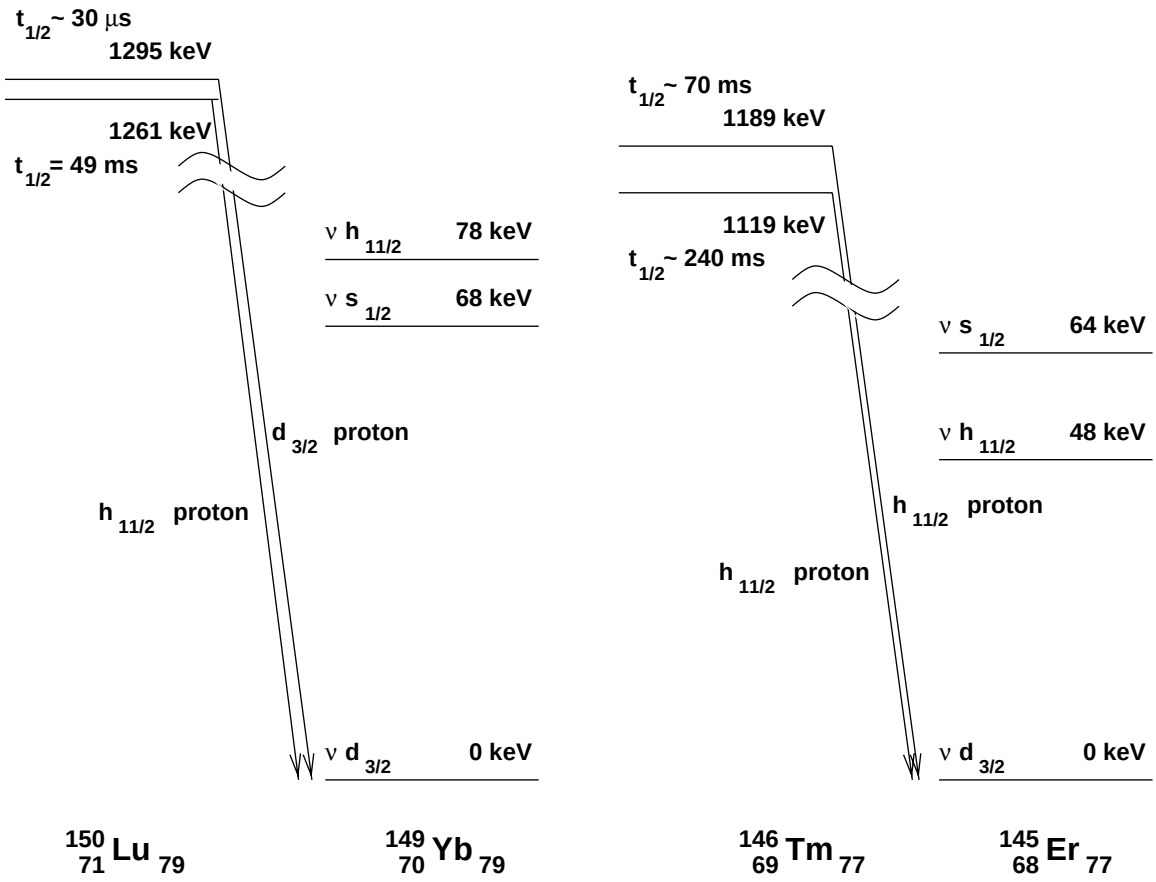


Figure 34: States available for the observation of fine structure in the proton emission from from $^{150}$Lu and $^{146}$Tm. The ordering and excitation energies of the neutron single-particle states in $^{149}$Yb and $^{145}$Er were calculated using a spherical macroscopic-microscopic model [44]. The proton transitions are from experimental observations [50, 52, 53, 70].

states in the daughter system. The final state, presumably a ground-state, should have one neutron-quasiparticle configuration corresponding to a neutron spectator for the initial $\pi$-$\nu$ state. However, one can also consider a proton transition to an excited neutron state. As with the proton orbitals, the neutron states $\nu s_{1/2}$, $\nu d_{3/2}$ and $\nu h_{11/2}$ are expected to be close to each other for the region of nuclei under consideration. The resulting neutron band-heads are at low excitation energies in the even-$Z$, odd-$N$ daughter nuclei. As illustrated in Figure 34, these three neutron states are calculated (by using a macroscopic-microscopic model — see Reference [44] and earlier references therein) to be within $\sim$ 80 keV for both $^{149}$Yb and $^{145}$Er. *Therefore, the energy factor alone does not exclude the possibility of observing fine structure in the proton emission.* For example, we calculated a relative branching ratio of 85 : 15 for the decay of $^{150gs}$Lu to the ground state and to a 70 keV excited state in $^{149}$Yb, and of 90 : 10 for the decay of $^{146}$Tm to corresponding states in $^{145}$Er. See also the next

section.

There may indeed be nuclear structure effects present that would act to suppress transitions to excited low lying states in the daughter. For example, there might be a proton rate truncation related to the change of the initial configuration of the neutron spectator. Within the very simple picture we have discussed, the only mechanism for such a process is an energy change and is already accounted for in the treatment given above. For the $\nu s_{1/2}$ and $\nu d_{3/2}$ orbitals, the low-lying levels might have mixed configurations which could help in the observation of fine structure in the proton decay of the odd-odd nuclei under consideration.

Proton Emission from $^{150}$Lu

For the odd-odd nucleus $^{150}$Lu two proton decaying states [50, 52, 70] have been reported (see Figure 35). The $\pi d_{3/2}$ and $\pi h_{11/2}$ orbitals are responsible for the $l = 2$ and $l = 5$ transitions, respectively. The existence of these two proton-emitting orbitals facilitates the search for fine structure by allowing a broader range of possible final states. Additionally, an experiment on the $^{150}$Lu activity should allow us to confirm the evidence for $^{150m}$Lu [50, 70] and measure its decay properties more precisely. The top plot in Figure 35 shows the low energy particle spectrum from the previous work [50, 70] which contains the peak from the $h_{11/2}$ protons emitted with a 49 ms half-life. Figure 36 shows the branching ratio calculated for an $l = 5$ transition to an excited state in $^{149}$Yb as a function of the excitation energy — the "fine structure" branching ratio for the 49 ms decay. Also shown in the figure is the observation limit reached in the previous work [50, 70]. As discussed in the section below beginning on page 127, the experiment we propose will provide up to a factor of 20 enhancement in sensitivity. This gain will put us in a strong position to observe fine structure in the proton decay in spite of hindrances from nuclear structure effects which are not accounted for in the simple calculations used to estimate upper limits for these branching ratios.

Proton Emission from $^{146}$Tm

For odd-odd $^{146}$Tm both known proton-emitting states are interpreted in terms of $l = 5$ emission. The $h_{11/2}$ proton is probably either coupled to two different neutron states or coupled in two different ways to the same neutron state. The nucleus $^{146}$Tm is the only spherical proton emitter yet observed

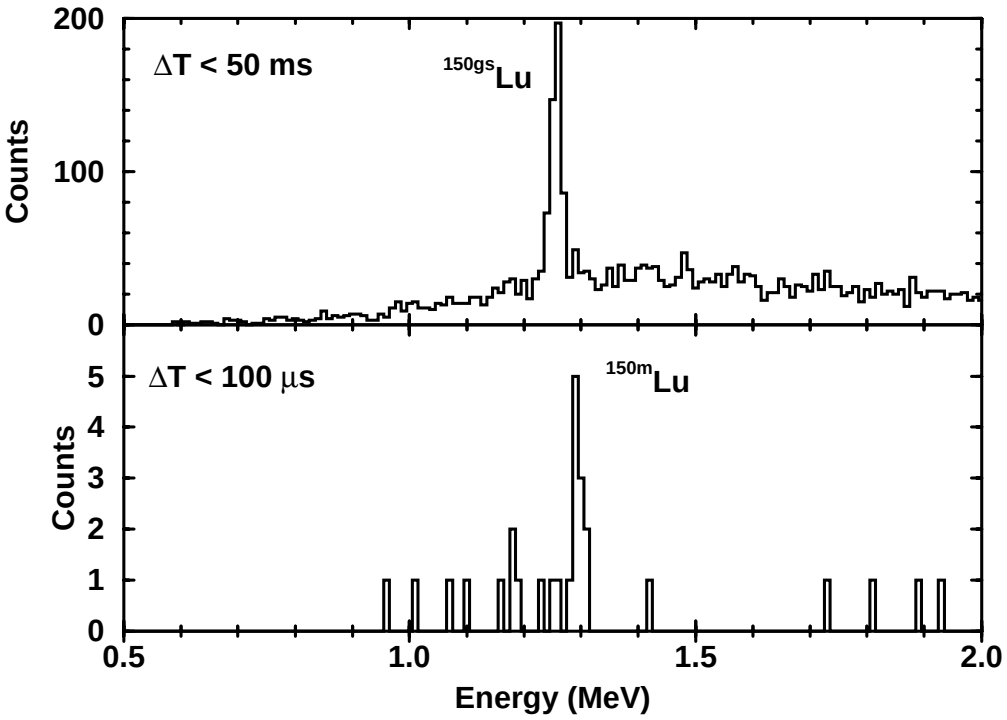


Figure 35: Top: Low energy particle spectrum showing $^{150gs}$Lu decay events occurring within the first 50 ms after recoils are implanted into the DSSD. The background results primarily from higher energy $\alpha$-decay events in which the $\alpha$-particles escape from the front of the DSSD thus depositing only part of their energy into the detector. Bottom: The low energy particle spectrum showing the $^{150m}$Lu decay events occurring within the first 100 $\mu$s after recoils are implanted into the DSSD (final analysis with overload corrections [47] included).

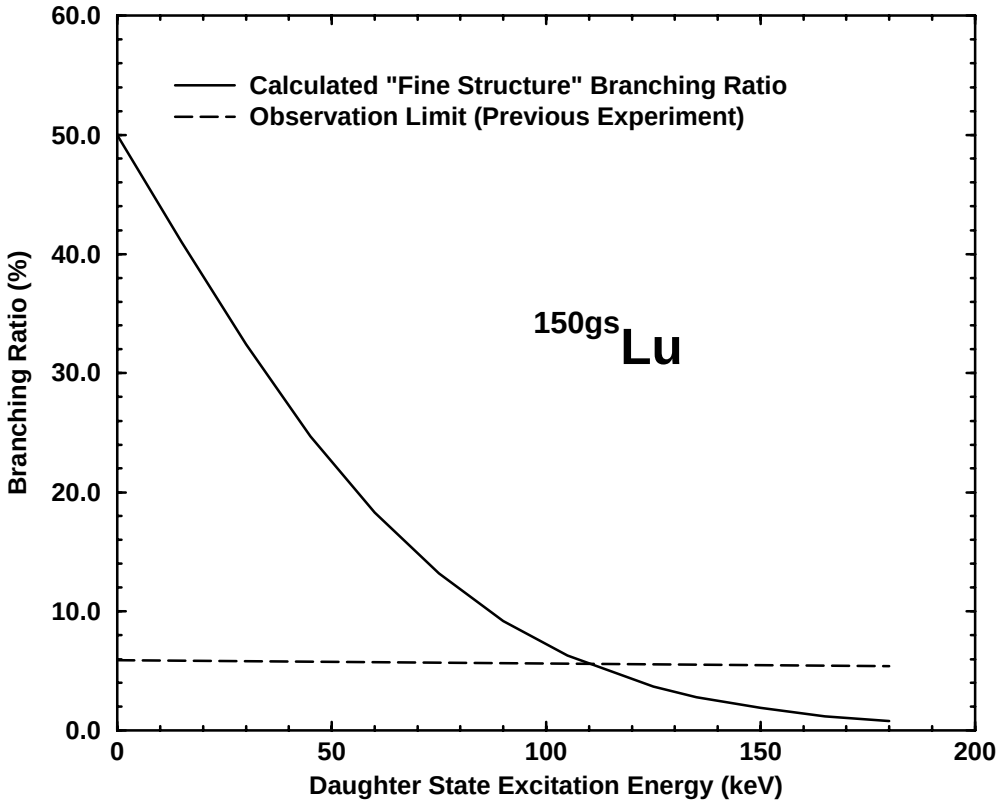


Figure 36: Calculated branching ratio using the WKB approach of Reference [60] for the $l = 5$ proton transition to an excited level in $^{149}$Yb as a function of the daughter state excitation energy. Since only energy difference for the proton decay energy $Q_p$ was accounted for, this curve should be understood as an upper limit for the "fine structure" branching ratio. Also shown is the observation limit reached in the previous experiment [50, 70]. The experiment we propose will increase the sensitivity by up to a factor of 20.

to have two proton-emitting states assigned to the same orbital [53, 60]. The neighboring proton-emitting odd-even and odd-odd pair of isotopes $^{151}$Lu and $^{150}$Lu both have a long-lived proton-emitting state based on the $h_{11/2}$ orbital and a short-lived state based on the $d_{3/2}$ orbital. The $\pi h_{11/2}$ and $\pi d_{3/2}$ proton-emitting states are known also for odd-even $^{147}$Tm. The nucleus $^{146}$Tm has not been studied with a system sensitive to short-lived proton activity. The HRIBF system, sensitive to proton half-lives as short as a few microseconds, very well may reveal a new proton-emitting state in $^{146}$Tm (based on the $d_{3/2}$ or $s_{1/2}$ orbital), which would make it the first nucleus observed with three proton-emitting states. If found, such a short-lived state would allow for a broader range of possible final states in the search for fine structure.

Because fewer $\alpha$-emitters are produced in the reaction used to make $^{146}$Tm, the low energy particle spectrum for $^{146}$Tm (see Reference [53]) has a much lower background from escaping $\alpha$-particles than does the spectrum for $^{150}$Lu (see top plot of Figure 35). This fact, together with the existence of the two proton-emitting states in $^{146}$Tm with millisecond half-lives, makes this nucleus an excellent case for a search for fine structure on the millisecond time scale.

Final Remarks

It is important to note that the purpose of the proposed study — namely to observe the excited neutron states in the very exotic nuclei $^{149}$Yb and $^{145}$Er — cannot be achieved by using presently existing "in-beam" spectroscopic techniques. Proton radioactivity studies *might offer the only way* to access this important information on the structure of nuclei beyond the proton drip-line. A particularly attractive option is to extend the proposed stable $^{58}$Ni beam experiment to one employing radioactive $^{56}$Ni when this beam become available at HRIBF. Since high selectivity and a low background in the low energy part of the recorded particle spectrum are crucial factors for observing fine structure, use of a $pn$ reaction channel instead of one involving $p3n$ is highly desirable.

## Detector Setup for Fine Structure Studies

Figure 37 shows the detector arrangement to be used at the RMS focal plane in the proposed experiment. By running the RMS in the converging mode we can deposit two charge states from the mass of interest instead of one into the DSSD for study. The converging mode thus provides

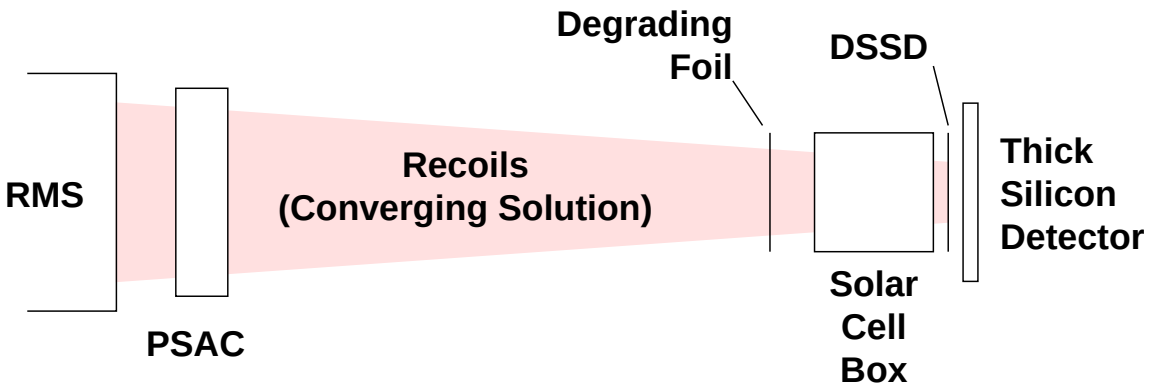


Figure 37: Proposed detector arrangement to be used in the study of proton emission from $^{150}$Lu and $^{146}$Tm.

roughly a factor of two increase in the production of the nuclei under study in comparison to the previous work in which only one charge state was used. Two detectors in our setup were not used in the previous work and are included now to provide better purity of the low energy particle spectra obtained from the DSSD — the solar cell box and the thick silicon detector. The thick silicon detector is placed behind the DSSD to detect $\beta$-particles and $\beta$-delayed protons ($\beta$p's), thus providing a veto signal for $\beta$p events. Since the silicon detector covers half of the solid angle into which nuclei in the strip detector can emit $\beta$- and $\beta$p-particles, it can reduce background events from $\beta$p's by a factor of two. The solar cell box is an arrangement of 4 inexpensive photo-voltaic cells around the sides of the front surface of the DSSD to detect charged particles ($\alpha$- and $\beta$p-particles) which do not deposit their full energy into the DSSD because they escape from its front surface. Since the solar cell box covers more than 80% of the solid angle from the front of the DSSD, the veto signal it provides can reduce background events from escaping $\alpha$-particles by up to a factor of five.

### Beam Time Request

For the $^{150}$Lu study we requested 5 days of beam time (15 shifts). In comparison to the previous HRIBF run [50, 70] a factor of two increase in statistics can be obtained from running time and up to a second factor of two increase from using the converging mode of the RMS. The use of the solar cell and silicon veto detectors can provide up to an additional factor of five in sensitivity from the reduction in background caused by escaping $\alpha$- and $\beta$p-particles. We thus improve our overall sensitivity for observing fine structure by up to a factor of 20. In this experiment there is the chance

to observe fine structure not only on the millisecond time scale from the long-lived proton-emitting state but also on the microsecond time scale from the short-lived state. The availability of the new DSSD electronics can increase the sensitivity for observing fine structure on the microsecond time scale by extending the observation window to shorter times.

For the $^{146}$Tm study 5 days of beam time (15 shifts) were requested. In comparison to the previous study performed at Daresbury [53], a factor of three increase in statistics can be obtained by increasing the beam current to 15 particle nA. Up to a factor of two increase can come from using the converging mode of the RMS. A factor of five increase can come from running time since the previous experiment lasted 18 hours. Up to a factor of five increase in sensitivity is expected from the background reduction provided by the solar cell box and the thick silicon detector for escaping $\alpha$- and $\beta$p-particles. Thus the overall sensitivity for observing fine structure can be increased by up to a factor of 150 in comparison to the previous work. This improvement factor is larger than the factor of 20 for $^{150}$Lu because a much more optimized setup was used for the recent $^{150}$Lu work [50, 70] than was used in the earlier study of $^{146}$Tm [53].

### Summary

Searches for fine structure in the proton emission from the odd-odd nuclei $^{150}$Lu (15 shifts) and $^{146}$Tm (15 shifts) are proposed in order to observe low-lying neutron states in the exotic daughter isotopes $^{149}$Yb and $^{145}$Er. The $^{150}$Lu study will be done first to ensure that we take advantage of the access we presently have to the *very rare* $^{96}$Ru target. The overall improvement in the detection power of the proposed experiment is up to a factor of 20 in comparison to the previous HRIBF study of $^{150}$Lu and up to a factor of 150 in comparison to the study of $^{146}$Tm at Daresbury.

### Latest Work on $^{150}$Lu and $^{146}$Tm

This section describes the latest results from experiments performed in the summer of 1999 to search for proton transitions to excited states in the daughter nuclei of the proton emitters $^{150}$Lu and $^{146}$Tm. This work is based on the proposal presented in the previous section. These results are a last-minute achievement and were not originally intended to be a part of this dissertation. The intention here is not to present experimental results that have been analyzed down to the last detail.

The spirit of this section, rather, is to give a flavor of on-going work related to what has already been presented.

## $^{150}$Lu

Among the motives for repeating the proton study of $^{150}$Lu was the need to obtain better statistics for determining the half-life of the new proton emitting state more precisely. The low statistics of the previous experiment led to so much uncertainty in the value we obtained for the half-life that we were not able to make use of the advantage offered by fast proton emission for determining the spectroscopic factor accurately — namely, that we do not have to worry about competition from the unknown branch to the EC/$\beta^+$ decay for determining the proton partial half-life. Additionally, the idea of searching for proton transitions to excited states in the daughter came from the data presented in Figure 33(b). The collection of three counts at 1.18 MeV suggests a peak caused by such a transition. Again, the low statistics of the previous experiment made it impossible to conclude whether this three count "peak" is real or not.

In this discussion, the $^{150}$Lu experiment which took place in 1998 is referred to as the "first" experiment and the one which took place in 1999 is referred to as the "second" experiment. Figure 38 summarizes the differences in the setup used for the two experiments. In the first experiment, the RMS was run in the diverging mode so that only a single charge state ($26^+$) of mass 150 ions was implanted into the strip detector. Use of the converging mode in the second experiment meant that two charge states ($25^+$ and $26^+$) could be implanted into the strip detector. The second experiment also employed a thin carbon foil placed 10 cm down stream from the target position while the first experiment did not. The purpose of this charge reset foil is to re-establish the charge state distribution for recoils whose charge states were disrupted by prompt internal conversion decays occurring during the 10 ns time-of-flight between the target and reset foil. The second experiment made use of the same beam ($^{58}$Ni ions at an energy of 315 MeV) and target (0.54 mg/cm$^2$ of $^{96}$Ru — 98% enriched — on a 2 mg/cm$^2$ gold foil, with the gold foil placed facing the beam) as was used in the first experiment.

Figure 39 compares the low energy decay events observed within the first 100 $\mu$s from the first and second experiments. The spectrum from the second experiment features three times more counts

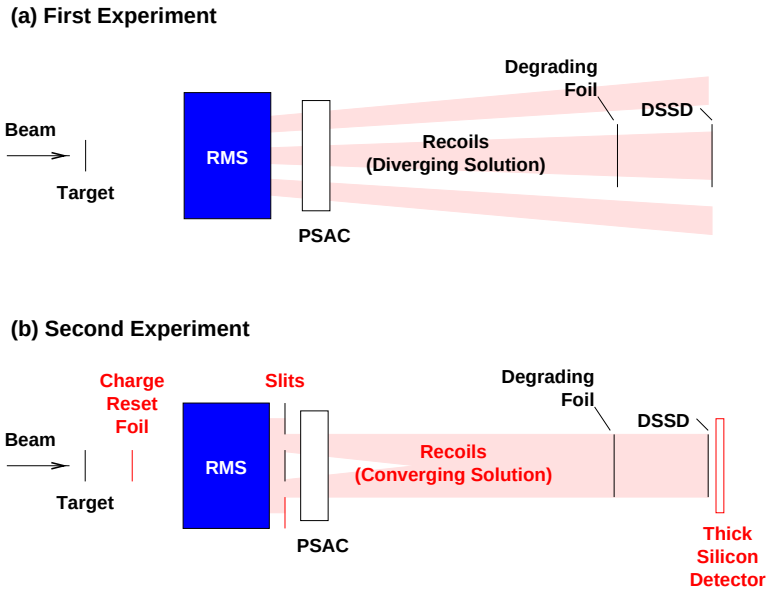


Figure 38: Comparison of the two experimental setups used to study proton emission from $^{150}$Lu. In the first experiment the RMS was run in the diverging mode to implant a single charge state of mass 150 recoils into the strip detector as is illustrated in (a). In the second experiment the RMS was run in the converging mode to deliver two charge states of mass 150 ions into the strip detector as is illustrated in (b); also a thin carbon foil placed 10 cm downstream from the target was used to reset the charge state distribution of the recoils.

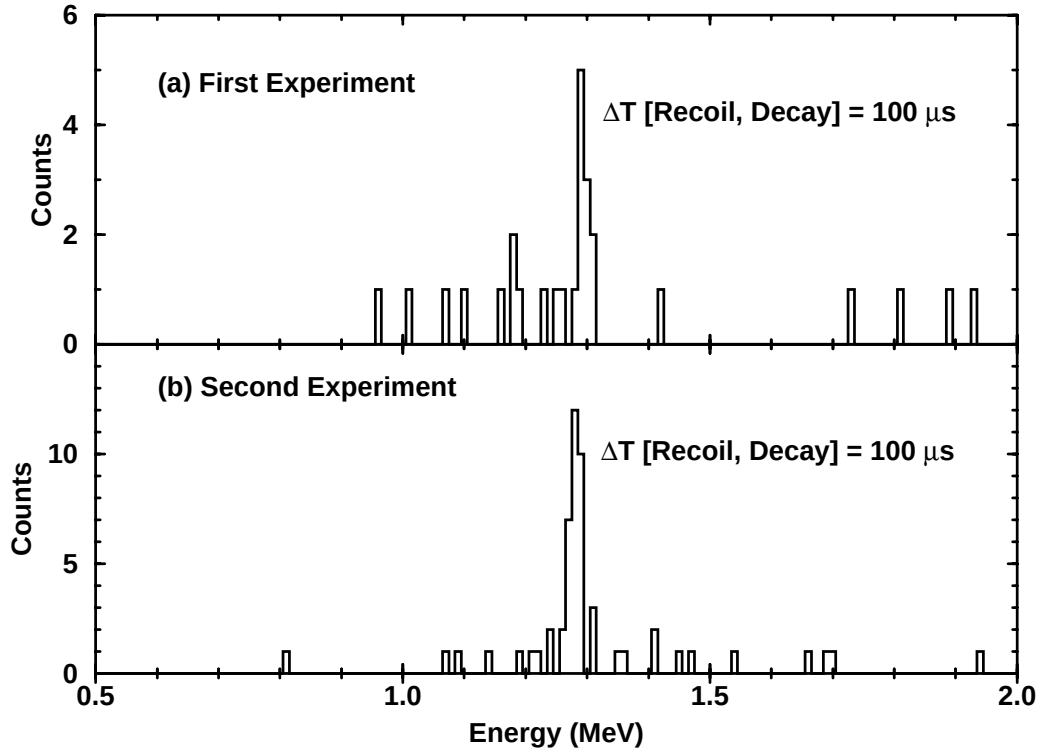


Figure 39: Data for the new proton transition at 1.295 MeV from (a) the first experiment and (b) from the second experiment. The data in (a) is from Figure 33(b).

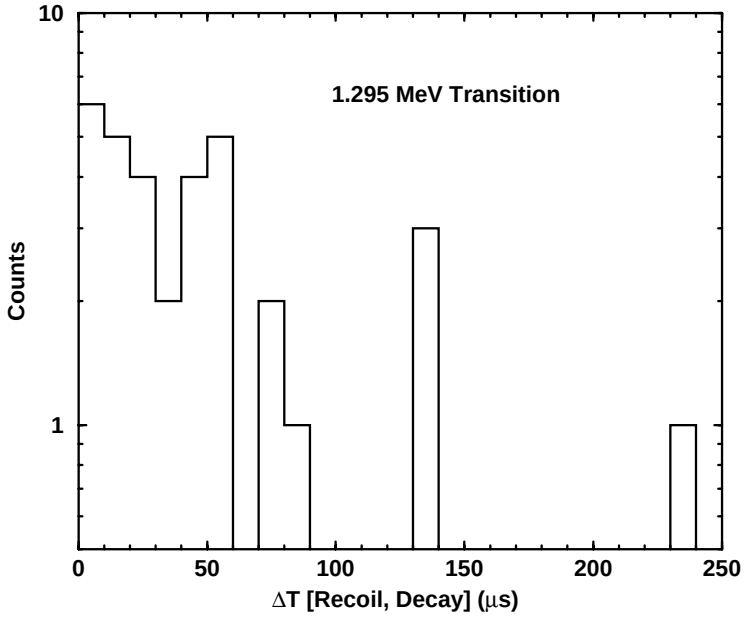


Figure 40: Time behavior of $^{150}$Lu 1.295 MeV proton transition from the second experiment. This data leads to a half-life estimate for the transition of 32 $\mu$s.

in the new transition together with a reduced background. We have not yet had a chance to make a careful determination of the half-life for the 1.295 MeV proton emitting state based on the data from the second experiment, but it is clear that we will be able to obtain a much more precise value from the new data. Figure 40 shows the time projection of this peak from the on-line data; the counts in this spectrum lead to a half-life estimate of 32 $\mu$s, confirming our previous assignment of a $d_{3/2}$ proton orbital to this transition. This half-life leads to an experimental spectroscopic factor of $S_p^{exp} = 0.25$, which is significantly less than the theoretical value of 0.73 [60]. This result is consistent with the trend we have noted for other $d_{3/2}$ proton transitions. Figure 39(b) clearly shows no evidence for a proton transition at 1.18 MeV. The three count "peak" in Figure 39(a) is apparently the result of background events and low statistics.

A large enhancement in the counts observed in the second experiment for the new $^{150}$Lu transition is related to the use of the charge reset foil behind the target. While the total number of events observed in the longer-lived proton transition at 1.261 MeV was almost the same for the two experiments (about 430 counts), we saw about 3 times as many total counts for the shorter-lived

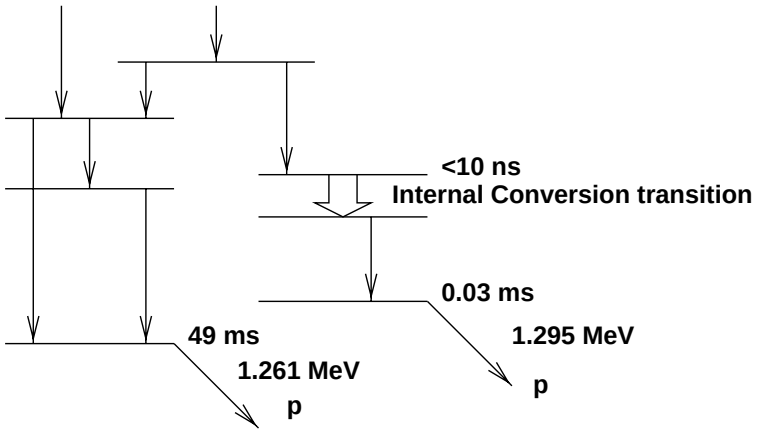


Figure 41: Level scheme illustrating how a nanosecond isomeric state populated in-beam and decaying by internal conversion could influence the observation of the fast proton transition at the focal plane for $^{150}$Lu depending on whether or not a charge reset foil is used just behind the target. An internal conversion transition occurring during the recoil's time-of-flight through the RMS can disrupt its charge state causing it not to reach the focal plane. If the transition occurs within about 10 ns — the time-of-flight for the recoil between the target and a reset foil placed 10 cm downstream from the target — the use of a reset foil can recover these lost ions by re-establishing their charge state distribution.

transition at 1.295 MeV in the second experiment (33 counts compared to 10). This significant increase in events shows that the state from which the 1.295 MeV proton transition originates is fed by a short-lived isomer (with a half-life on the order of 10 ns or less) which decays by internal conversion while the state from which the other proton transition originates is not. Figure 41 gives a schematic illustration of the kind of feature that must be present in the level structure of $^{150}$Lu populated in our reaction to account for this result.

### $^{146}$Tm

We produced $^{146}$Tm with a $p3n$ reaction channel. The target consisted of 0.91 mg/cm$^2$ of $^{92}$Mo and the beam was $^{58}$Ni at an energy of 292 MeV. As with the second $^{150}$Lu experiment — see Figure 38(b) — we made use of a charge reset foil 10 cm behind the target, and we ran the RMS in the converging mode to implant two charge states ($26^+$ and $27^+$) of mass 146 ions into the strip detector. We scaled the RMS to accept central ions of $^{146}$Tm at an energy of 90 MeV.

The previously published work on $^{146}$Tm [53] identified two proton transitions: one at $1.119 \pm 0.005$ MeV with a half-life of $235 \pm 27$ ms and the other at $1.189 \pm 0.005$ MeV with a half-life of $72 \pm 23$ ms. The Oak Ridge experiment represents an enhancement in the observed proton events by a factor of 20 over the previously published results. This new data set will clearly yield a better

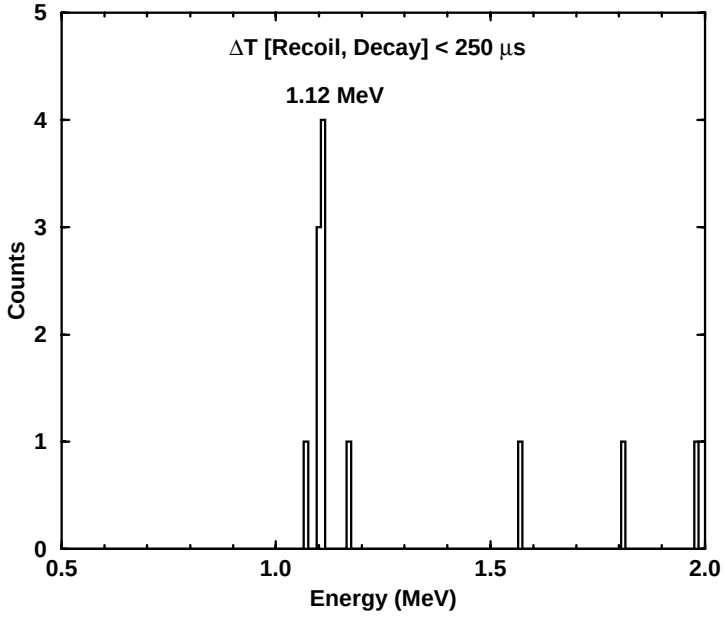


Figure 42: Decays following the implantation of mass 146 recoils into the DSSD within 250 $\mu$s. This plot illustrates that we found no evidence for a microsecond proton transition in $^{146}$Tm.

determination of the half-lives of the two known proton transitions.

One result from this experiment is that we did not find a new proton transition with a half-life on the microsecond time scale. Figure 42 shows the low energy decay events observed within 250 $\mu$s following the implantation of mass 146 ions into the DSSD. Other than a few background events (presumably from escaping $\alpha$-particles) the only events are from the strongly populated, previously observed proton transition at 1.12 MeV.

Another result from the experiment is that we observed at least one new proton transition from $^{146}$Tm. Figure 43 shows how we processed the on-line data to see the new transitions. Figure 43(a) shows the decay events observed on a much longer time scale than the previous figure — up to 50 ms after the arrival of a mass 146 ion at the detector. The two previously observed proton transitions are clearly visible at the lower end of this plot together with lines from longer-lived $\alpha$-transitions which appear between 4 and 5 MeV. Figure 43(b) shows the decay events occurring within a 50 ms time window 500 ms after the arrival of an ion. This plot gives a feel for what part of the events in Figure 43(a) are caused by long-lived activities and random events. Figure 43(c) is obtained by

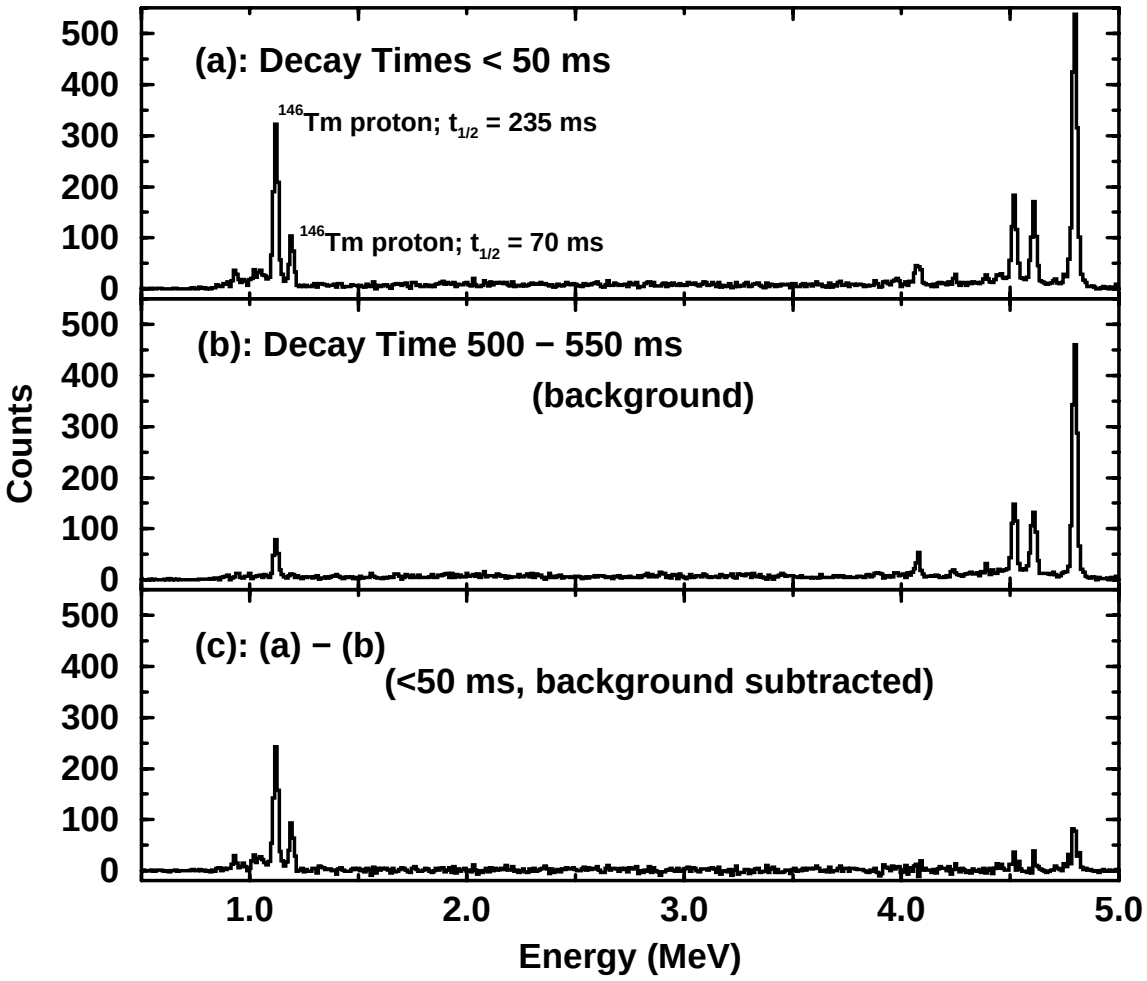


Figure 43: (a) Decays following the implantation of mass 146 recoils into the DSSD within the first 50 ms. (b) Decays in a 50 ms time window occurring half a second after the implantation of mass 146 recoils. This spectrum shows the contribution to the background in (a) from random correlations and long-lived decays. (c) A background subtracted spectrum of the decays occurring within 50 ms from the implantation of mass 146 ions. This spectrum was obtained by subtracting (b) from (a).

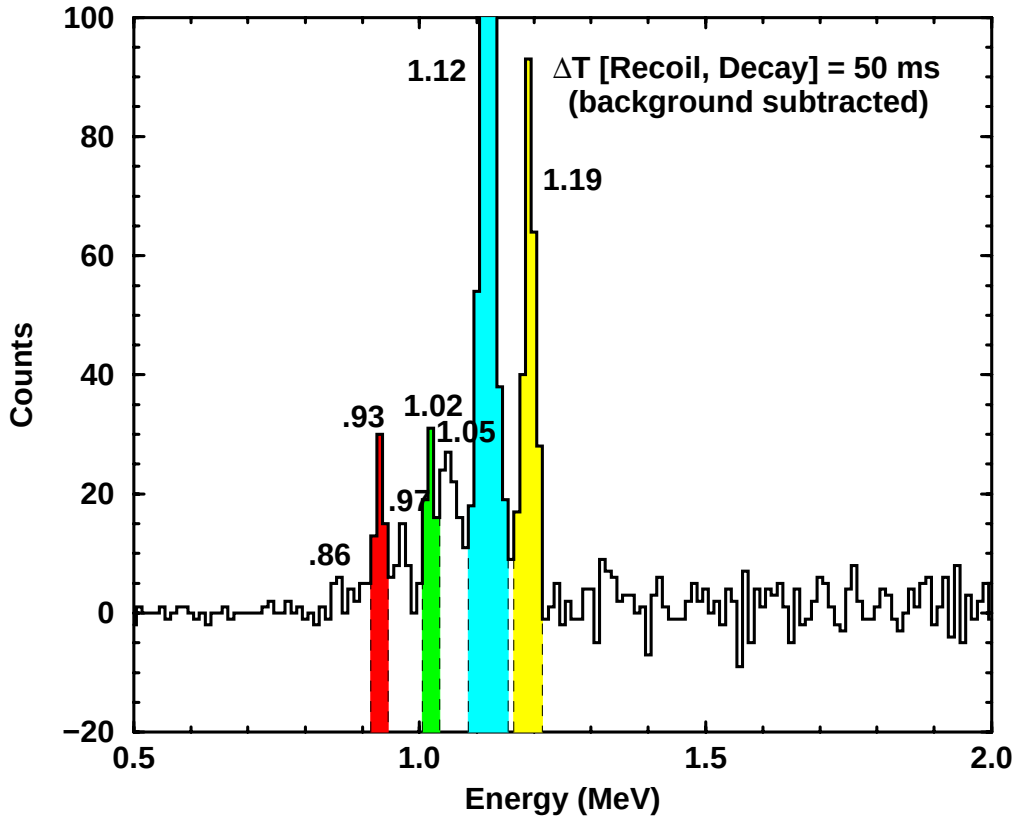


Figure 44: Expanded view of the proton peaks from Figure 43(c). The labels on the peaks are given for the channel with the highest number of counts. The color shading on the peaks shows the channels used to generate the time projections given in Figures 47 and 48.

subtracting the spectrum in (b) from that in (a). As the disappearance of the $\alpha$-particle lines shows, this approach does a reasonably good job of eliminating the random events from the Figure 43(a). Presumably this approach does an equally good job of eliminating the random background events in the vicinity of the proton peaks caused by escaping $\alpha$-particles.

Figure 44 provides a closer look at the low energy region of interest in Figure 43(c) around the strong proton peaks. Below these two peaks there are a few smaller peaks indicating new proton transitions — perhaps to excited states in $^{145}$Er. The peak at 1.05 MeV could be at least in part caused by the strong proton transition in $^{147}$Tm; we have not yet had a chance to screen the data from this possible source of contamination. There are at least two other reasonably strong new peaks: one at 0.93 MeV and the other at 1.02 MeV.

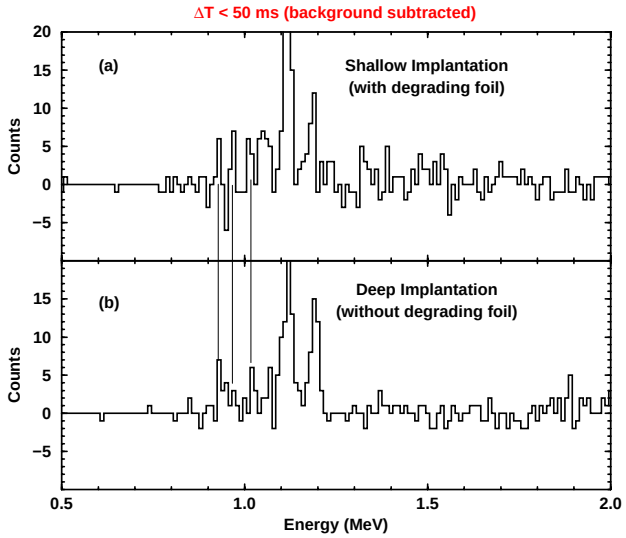


Figure 45: Proton transition spectra from the $^{146}$Tm experiment for the cases of (a) shallow and (b) deep implantation of recoils into the DSSD. Even with their poor statistics arising from the limited running times, these spectra show that the new peaks remain under very different experimental conditions. The peaks do not appear to be produced by escaping protons from the 1.12 and 1.19 MeV transitions. These background subtracted spectra were produced following the same procedure used to generate the spectrum in Figure 43(c).

When using strip detectors to study decay by charged particle emission, it is generally a good practice to slow down the recoils by using a degrading foil to decrease the amount of energy they deposit into the detector. This technique minimizes problems with the overloading and recovery of the decay amplifiers which can change the observed energy of prompt decay events as was discussed beginning on page 108. For the $^{146}$Tm experiment, however, we have shown that shifts in the observed energy of prompt decay events is not at all a critical issue since there is no fast proton activity. To investigate whether the new proton peaks might not somehow be caused by the process of protons from the two strong proton transitions escaping from the front of the detector, we substantially varied the depth of the implanted ions by choosing whether or not to use a thin copper foil in front of the strip detector — see Figure 38(b) — to lower the energy of the implanted ions. Without the degrader in place, ions arrive at the strip detector with an energy of more than 60 MeV. The use of a 2.27 mg/cm$^2$ Cu degrading foil reduces the energy of the recoils well below 20 MeV. Figure 45 compares the low energy decay spectrum produced with (a) shallow and (b) deep implantation of recoils. These background subtracted spectra, which show the decay events occurring within 50 ms

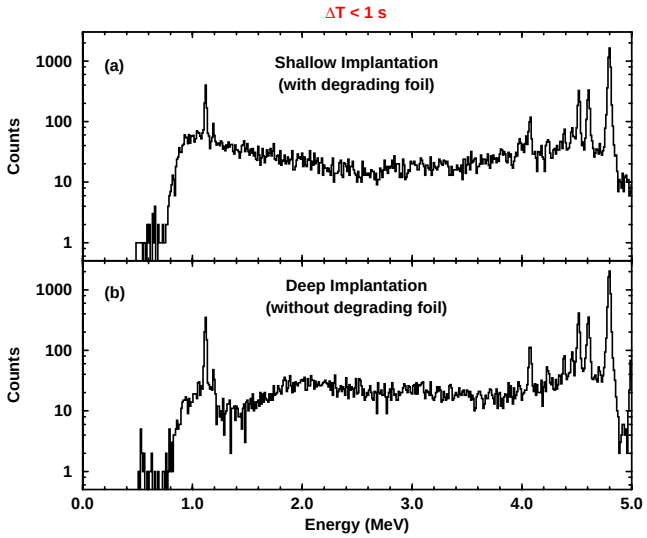


Figure 46: Influence of the implantation depth of ions in the DSSD on the background from escaping $\alpha$-particles in the decay spectrum. Both data sets were obtained in the $^{146}$Tm experiment. As is shown in (a), the hump from the background overlaps the energy region where the proton transitions occur when a degrader foil is used to lower the energy of the ions entering the DSSD. The distribution of background events shifts to higher energy, away from the critical region where proton transitions are observed when no degrader foil is used to slow down the ions as is shown in (b).

of the arrival of an ion at the DSSD, were produced following the same procedure used to produce Figure 43(c). The result of this test is that the new peaks remain present even under very different implantation conditions. This test gives us confidence that the peaks are indeed real.

Figure 46 demonstrates the advantage of not using a degrader to slow down the recoils by showing the effect of the implantation depth of recoils on the background caused by escaping $\alpha$-particles. The plots in the figure show the decay events observed within the first second after the arrival of recoils at the detector (a) with and (b) without the degrading foil. (No background correction was applied to these plots.) By implanting the ions more deeply into the detector, we shift the distribution of background events from escaping $\alpha$-particles to higher energies — away from the critical region of interest near 1 MeV where we observe the new proton transitions. Deeper implantation into the detector means that the $\alpha$-particles deposit more partial energy into the detector before escaping from the front. Thus, by not using a degrader we gain by reducing the background in the critical part of the decay spectrum where the proton activity is observed. The plot presented in Figure 44 was generated by using data from all runs and contains data produced with and without the use of

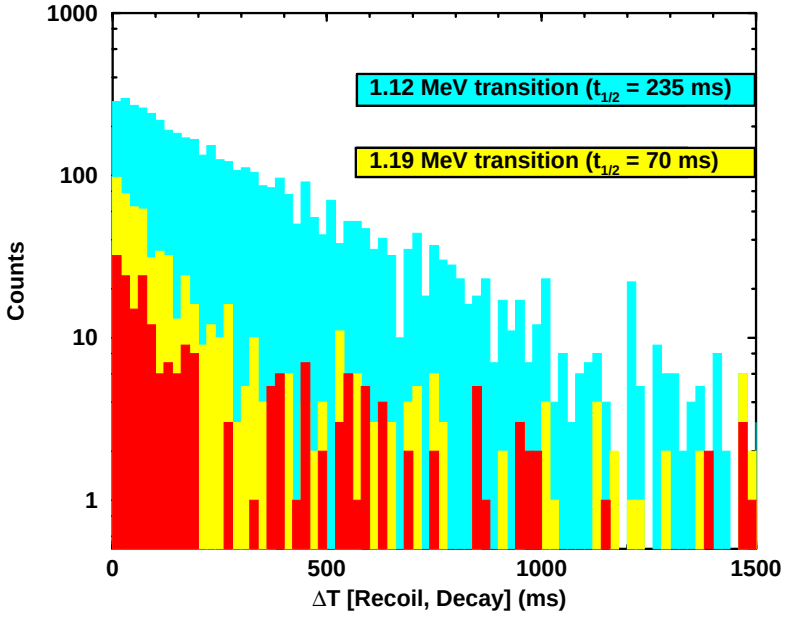


Figure 47: Time projection of the 0.93 MeV peak (shown in red) from the $^{146}$Tm experiment in comparison to the time projections of the proton transitions at 1.12 and 1.19 MeV. The decay behavior of this new transition is similar to the decay behavior of the 1.19 MeV transition which has a half-life of 70 ms.

the degrader foil in front of the DSSD. Most of the runs were performed without using the degrader.

Figure 47 shows the decay behavior of the 0.93 MeV peak (displayed in red) compared to that of the two strong transitions. (The spectra in this figure include a correction for background activity. [5]) The decay behavior of the 0.93 MeV transition follows the decay behavior of the 1.19 MeV transition which has a half-life of around 70 ms. Assuming that both transitions originate from the same state in $^{146}$Tm, we obtain a preliminary branching ratio of 20% for the 0.93 MeV transition compared to 80% for the one at 1.19 MeV by summing the counts in the corresponding data sets in Figure 47.

Figure 48 shows the decay behavior of the 1.02 MeV peak (displayed in green) compared to that of the two strong transitions. These spectra include the same type of background subtraction as was used for the spectra in Figure 47. Because of the low statistics associated with the 1.02 MeV peak it is difficult to conclude, at least for now, if this transition has a half-life that matches the half-life

[5] To perform this correction a spectrum taken to represent the background from random correlations and escaping $\alpha$-particles was generated by summing the time projection of the data in energy bins from 0.60 to 0.80 MeV with the time projection of data in energy bins 1.25 to 1.45 MeV. The normalization factor used for subtracting this background from the time projection of the data in each energy peak was determined by requiring the sum of counts in the resulting time spectrum between 1.5 and 2.5 seconds to be roughly zero.

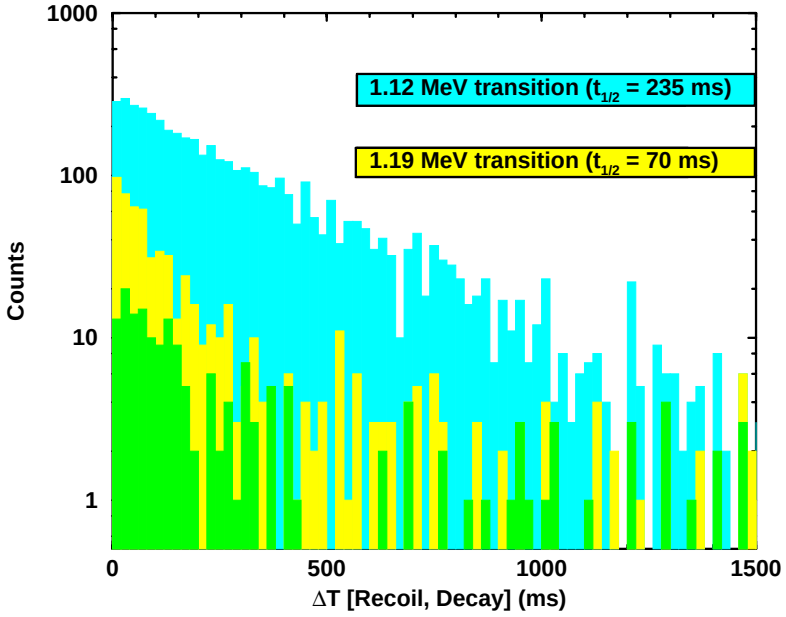


Figure 48: Time projection of the 1.02 MeV peak (shown in green) from the $^{146}$Tm experiment in comparison to the time projections of the proton transitions at 1.12 and 1.19 MeV. The low statistics of this new transition make it difficult to tell whether its decay behavior matches that of one of the other two transitions.

of one of the two strong transitions.

At this early stage of the analysis the interpretation of this data are not clear. One approach to the data is to interpret the new proton lines as originating from decays to excited states in the daughter nucleus. Figure 49 shows one such possible level scheme suggested by the data — in particular by the similarity in half-life of the 0.93 and 1.19 MeV transitions. The assignment given to the 0.86 keV transition is quite speculative and is entirely based on the similar energy differences. There is also a surprise with the branching ratio shown for the proton transitions de-populating the state at 1.19 MeV. The branching of 20% for the 0.93 MeV transition is much too large compared to the value of 0.04% expected by using a calculation based on the WKB approach presented in Reference [60]. Thus, if indeed the 0.93 MeV transition is to an excited state in $^{145}$Er there would have to be some nuclear structure effect present which strongly enhances this branch compared to the 1.19 MeV branch.

Another explanation for the data — at least for the peak at 0.93 MeV — is to argue that this line originates not from decays to excited state in $^{145}$Er but that instead it arises from a new proton

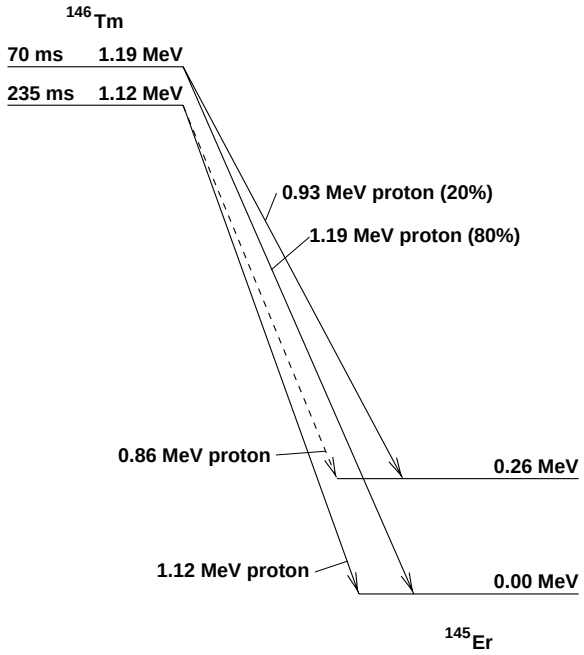


Figure 49: Tentative level scheme showing possible proton transitions to excited states from $^{146}$Tm.

emitting state in $^{146}$Tm with a $d_{3/2}$ orbital assignment. A calculation based on the WKB approach presented in Reference [60] supports this scenario by predicting a proton partial half-life of 63 ms for a 0.93 MeV transition from $^{146}$Tm.

It is clear that a more careful analysis of the data together with more thought into its interpretation is needed to make progress in settling these questions. If the new proton transitions we are observing are to excited states in the daughter nucleus, this would be the first time this effect has been observed in the case of a spherical proton emitter. This scenario is supported by the presence of more than one new proton transition in the data. If, on the other hand, the transition at 0.93 MeV is the manifestation of a new proton emitting state in $^{146}$Tm, the result is still very important. This would be the first case in which a nucleus has been observed with more than two proton emitting states.

## Outlook

Designed to be a new generation in a series of recoil mass spectrometers, the RMS has certainly lived up to expectations regarding its performance. Not only has the RMS repeatedly demonstrated its use as a powerful new research tool, but also there are a wealth of ideas on how to extend its use

by employing its unique achromatic focus. One idea being pursued is to place a detector station at the achromatic focus to take advantage of the shorter recoil flight path, good beam rejection, and possibly higher efficiency offered by the momentum achromat alone. Another idea is to run with a detector station behind all or part of the momentum achromat filled with a low pressure gas to enhance the charge state collection efficiency and to reduce the time-of-flight.

There are no impediments in sight to slow down the success of present lines of research taking place at the RMS including the study of proton emitters. As the Holifield Radioactive Ion Beam Facility carries out its challenging research and development mission as a first generation facility to develop sustainable and usable radioactive ion beams (RIBs), it is clear that these new beams will not be available 100% of the time. The RMS is ready and able not only to make use of these exotic beams, but also to make the most effective use of our nation's accelerator resources in Oak Ridge by doing the highest quality of nuclear research possible with stable ion beams as well. Carrying out the best research with stable beams is an essential part of the process that will allow the community of RMS users to develop the techniques and ideas necessary to address the difficult technical challenges of doing good science with low intensity RIBs.

The RMS possesses a true wealth of detector systems and electronics. In terms of this combination of resources there is not a better equipped nuclear structure laboratory in North America and perhaps even the whole world. Those of us who use the RMS must not think in terms of why the the conventional experiments of the past will fail. We must open ourselves to the possibilities of the not-yet-dreamed-of experiments of the future — to the experiments that we clearly already have the resources to make happen. The recent $^{66}$As isomer decay tagging experiment mentioned briefly on page 104 is an outstanding example of this spirit — by making an imaginative yet simple use of the abundant resources at our disposal. The RMS user community has the opportunity to create a center for uncovering exciting new physics with low intensity RIBs.

The future of the RMS looks bright.

[1] J. D. Cole, T. M. Cormier, J. H. Hamilton, and A. V. Ramayya, Nucl. Instrum. Methods B **70**, 343 (1992).
T. M. Cormier, J. D. Cole, J. H. Hamilton, and A. V. Ramayya, Nucl. Instrum. Methods A **297**, 199 (1990).
J. D. Cole, T. M. Cormier, and J. H. Hamilton, in *Exotic Nuclear Spectrosopy*, edited by W. C. McHarris (Plenum Press, New York, 1990), p. 11.

[2] P. F. Mantica, Nucl. Instrum. Methods B **99**, 338 (1995).

[3] C. J. Gross, T. N. Ginter, Y. A. Akovali, M. J. Brinkman, J. W. Johnson, J. Mas, J. W. McConnell, W. T. Milner, D. Shapira, and A. N. James, in CP392, *Application of Accelerators in Research and Industry*, edited by J. L. Duggan and I. L. Morgan (AIP Press, New York, 1997), p.401.

[4] C. J. Gross, T. N. Ginter, D. Shapira, W. T. Milner, J. W. McConnell, A. N. James, J. W. Johnson, J. Mas, P. F. Mantica, R. L. Auble, J. J. Das, J. L. Blankenship, J. H. Hamilton, R. L. Robinson, Y. A. Akovali, C. Baktash, J. C. Batchelder, C. R. Bingham, M. J. Brinkman, H. K. Carter, R. A. Cunningham, T. Davinson, J. D. Fox, A. Galindo-Uribarri, R. Grzywacz, J. F. Liang, B. D. MacDonald, J. MacKenzie, S. D. Paul, A. Piechaczek, D. C. Radford, A. V. Ramayya, W. Reviol, D. Rudolph, K. Rykaczewski, K. S. Toth, W. Weintraub, C. Williams, P. J. Woods, C.-H. Yu, and E. F. Zganjar, submitted to Nucl. Instrum. Methods **A**.

[5] T. M. Cormier, Annu. Rev. Nucl. Part. Sci. **37**, 537 (1987).

[6] T. M. Cormier and P. M. Stwertka, Nucl. Instrum. Methods **184**, 423 (1981).

[7] T. M. Cormier, M. G. Herman, B. S. Lin, and P. M. Stwertka, Nucl. Instrum. Methods **212**, 185 (1983).

[8] P. Spolaore, J. D. Larson, C. Signorini, S. Beghini, X.-K. Zhu, and H.-Z. Si, Nucl. Instrum. Methods A **238**, 381 (1985).

[9] C. Signorini, S. Beghini, A. D. Bello, G. Montagnoli, F. Scarlassara, G. F. Segato, F. Soramel, D. Ackermann, L. Corradi, A. Facco, H. Moreno, L. Müller, D. R. Napoli, and G. F. Prete, Nucl. Instrum. Methods A **339**, 531 (1994).

[10] C. N. Davids and J. D. Larson, Nucl. Instrum. Methods B **40/41**, 1224 (1989).

[11] C. N. Davids, B. B. Back, K. Bindra, D. J. Henderson, W. Kutschera, T. Lauritsen, Y. Nagame, P. Sugathan, A. V. Ramayya, and W. B. Walters, Nucl. Instrum. Methods B **70**, 358 (1992).

[12] A. K. Sinha, N Madhavan, J. J. Das, P. Sugathan, D. O. Kataria, A. P. Patro, G. K.Mehta, Nucl. Instrum. Methods A **339**, 543 (1994).

[13] J. P. Dufour, R. Del Moral, H. Emmermann, F. Hubert, D. Jean, C. Poinot, M. S. Pravikoff, A. Fleury, H. Delagrange, K.-H. Schmidt, Nucl. Instrum. Methods A **248**, 267 (1986).
R. Anne, D. Bazin, A. C. Mueller, J. C. Jacmart, and M. Langevin, Nucl. Instrum. Methods A **257**, 215 (1987).
A. C. Mueller and R. Anne, Nucl. Instrum. Methods B **56/57**, 559 (1991).
R. Anne and A. C. Mueller, Nucl. Instrum. Methods B **70**, 276 (1992).

[14] V. Ninov, K. E. Gregorich, C. A. McGrath, *ENAM98: Exotic Nuclei and Atomic Masses*, edited by B. M. Sherrill, D. J. Morrissey, and C. N. Davids (American Institute of Physics, Woodbury, New York, 1998), p. 704.

[15] M. Leino, J. Äystö, T. Enqvist, P. Heikkinen, A. Jokinen, M. Nurmia, A.Ostrowski, W. H. Trzaska, J. Uusitalo, K. Eskola, P. Armbruster, V. Ninov, Nucl. Instrum. Methods B **99**, 653 (1995).

[16] W. Reisdorf, Z. Phys. A **300**, 227 (1981).

[17] J. R. Beene, N. G. Nicolis, and D. G. Sarantites, Code evapOR (unpublished), evolved from the code PACE by A. Gavron, Phys. Rev. C **21**, 230 (1980).

[18] P. J. Sellin, P. J. Woods, D. Branford, T. Davinson, N. J. Davis, D. G. Ireland, K. Livingston, R. D. Page, A. C. Shotter, S. Hofmann, R. A. Hunt, A. N. James, M. A. C. Hotchkis, M. A. Freer, and S. L. Thomas, Nucl. Instrum. Methods A **311**, 217 (1992).

[19] S. Hofmann, I. Zychor, F. P. Hessberger, and G. Münzenberg, Z. Phys. A **325**, 37 (1986).

[20] E. S. Paul, P. J. Woods, T. Davinson, R. D. Page, P. J. Sellin, C. W. Beausang, R. M. Clark, R. A. Cunningham, S. A. Forbes, D. B. Fossan, A. Gizon, J. Gizon, K. Hauschild, I. M. Hibbert, A. N. James, D. R. LaFosse, I. Lazarus, H. Schnare, J. Simpson, R. Wadsworth, and M. P. Waring, Phys. Rev. C **51**, 78 (1995).

[21] J. H. Hamilton, *Proc. Fifth Adriatic Int. Conf. on Nuclear Phys.,* in *Fundamental Problems in Heavy Ion Collisions,* edited by N. Cindro, *et al.* (World Scientific, Singapore, 1984), p. 111.

[22] S. Wen, A. V. Ramayya, S. J. Robinson, C. F. Maguire, W. C. Ma, X. Zhao, T. M. Cormier, P. M. Stwertka, J. D. Cole, E. F. Zganjar, R. B. Piercey, M. A. Herath-Banda, J. Eberth, and M. Wiosna, J. Phys. G **11**, L173 (1985).

[23] A. N. James, T. P. Morrison, K. L. Ying, K. A. Connell, H. G. Price, and, J. Simpson, Nucl. Instrum. Methods A **267**, 144 (1988).

[24] K. L. Ying, P. J. Bishop, A. N. James, A. J. Kirwan, D. J. G. Love, T. P. Morrison, P. J. Nolan, D. C. B. Watson, K. A. Connell, A. H. Nelson, and J. Simpson, J. Phys. G **12**, L211 (1986).

[25] B. J. Varley, M. Campbell, A. A. Chishti, W. Gelletly, L. Goettig, C. J. Lister, A. N. James, and O. Skeppstedt, Phys. Lett. B **194**, 463 (1987).

[26] H. Wollnik, *Optics of Charged Particles* (Academic Press, New York, 1987).

[27] H. Wollnik, J. Brezina, M. Berz, and W. Wendel, Proc. AMCO-7, GSI Report THD-26 (1984) p. 679.
H. Wollnik, J. Brezina, and M. Berz, Nucl. Instrum. Methods A **258**, 1987 (402).

[28] S. Kowalski and H. A. Enge, Program RAYTRACE, Massachusetts Institute of Technology, Laboratory for Nuclear Science, unpublished.

[29] A. N. James, ORNL RMS Beam Optics Reports 1-7, 1995-1997 (unpublished).

[30] T. N. Ginter, in *Proceedings of the International Conference on Perspectives in Nuclear Physics, Nassau, Bahamas, 1998*, edited by J. H. Hamilton, H. K. Carter, and R. B. Piercey, (World Scientific Press, Singapore, 1999), p. 139.

[31] D. G. Sarantites, H.-F. Hua, M. Devlin, L. G. Sobotka, J. Elson, J. T. Hood, D. R. LaFosse, J. E. Sarantites, and M. R. Maier, Nucl. Instrum. Methods A **381**, 418 (1996).

[32] C. J. Gross, D. Shapira, J. Batchelder, J. W. Johnson, J. Blankenship, D. Rudolph, and A. Poland, Oak Ridge National Laboratory Report No. ORNL-6916: Physics Division Progress Report for Period Ending September 30, 1996, p. 1-57.

[33] C. J. Gross, D. Shapira, and J. Mas, "RMS Focal Plane Detector — Position Sensitive Avalanche Counter", Oak Ridge National Laboratory Report No. ORNL-6957: Physics Division Progress Report for Period Ending September 30, 1998.

[34] T. A. Lewis and D. Shapira, Oak Ridge National Laboratory Report No. ORNL-6916: Physics Division Progress Report for Period Ending September 30, 1996, p. 1-18.

[35] E. F. Zganjar, A. Piechaczek, J. C. Batchelder, and C. J. Gross, in *Proceedings of the International Conference on Perspectives in Nuclear Physics, Nassau, Bahamas, 1998*, edited by J. H. Hamilton, H. K. Carter, and R. B. Piercey, (World Scientific Press, Singapore, 1999), p. 187.

[36] S. D. Paul, C. Baktash, W. Satula, C. J. Gross, I. Birriel, R. M. Clark, R. A. Cunningham, M. Devlin, P. Fallon, A. Galindo-Uribarri, T. N. Ginter, D. R. Lafosse, J. Kay, F. Lerma, I. Y. Lee, C. Leyland, A. O. Macchiavelli, B. D. MacDonald, S. J. Metcalfe, A. Piechaczek, D. C. Radford, W. Reviol, L. L. Riedinger, D. Rudolph, K. Rykaczewski, D. G. Sarantites, J. X. Saladin, D. Shapira, G. N. Sylvan, S. L. Taybor, K. S. Toth, W. Weintraub, D. F. Winchel, V. Q. Wood, R. Wyss, and C.-H. Yu, Phys. Rev. C **58**, R3037 (1998).

[37] C.-H. Yu, J. C. Batchelder, C. R. Bingham, R. Grzywacz, K. Rykaczewski, K. S. Toth, Y. Akovali, C. Baktash, A. Galindo-Uribarri, T. N. Ginter, C. J. Gross, M. Karny, S. H. Kim, B. D. MacDonald, S. D. Paul, D. C. Radford, J. Szerypo, and W. Weintraub, Phys. Rev. C **58**, R3042 (1998).

[38] C. J. Gross, Y. A. Akovali, C. Baktash, J. C. Batchelder, C. R. Bingham, M. P. Carpenter, C. N. Davids, T. Davinson, D. Ellis, A. Galindo-Uribarri, T. N. Ginter, R. Grzywacz, R. V. F. Janssens, J. W. Johnson, J. F. Liang, C. J. Lister, J. F. Mas, B. D. MacDonald, S. D. Paul, A. Piechaczek, D. C. Radford, W. Reviol, K. Rykaczewski, W. Satula, D. Seweryniak, D. Shapira, K. S. Toth, W. Weintraub, P. J. Woods, C.-H. Yu, E. F. Zganjar, and J. Uusitalo, in *ENAM 98, Exotic Nuclei and Atomic Masses,* proceedings of the international conference, Bellaire, Michigan, USA, edited by B. M. Sherrill, D. J. Morrissey, and C. N. Davids (AIP Press, Woodbury, New York, 1998), p. 444.

[39] R. Grzywacz, S. Andriamonje, B. Blank, F. Boue, S. Czajkowski, F. Davi, R. Del Moral, C. Donzaud, J. P. Dufour, A. Fleury, H. Grawe, A. Grewe, A. Heinz, Z. Janas, A. R. Junghans, M. Karny, M. Lewitowicz, A. Musquere, M. Pfutzner, M.-G. Porquet, M. S. Pravikoff, J. E. Sauvestre, and K. Summerer, Phys. Lett. B **429**, 247 (1998).

[40] J. J. Ressler, A. Piechaczek, W. B. Walters, A. Aprahamian, J. C. Batchelder, C. R. Bingham, D. S. Brenner, T. N. Ginter, C. J. Gross, R. Grzywacz, D. Kulp, B. D. MacDonald, W. Reviol, J. R. Rikovska, K. Rykaczewski, M. Weischer, J. A. Winger, and E. F. Zganjar, submited to *Phys. Rev. Lett.*

[41] R. Grzywacz, American Physical Society Division of Nuclear Physics Meeting, Asilomar, CA, October, 1999.

[42] P. J. Woods and C. N. Davids, Annu. Rev. Nucl. Part. Sci. **47**, 541 (1997).

[43] P. Möller, J. R. Nix, W. D. Myers, and W. J. Swiatecki, At. Data Nucl. Data Tables **59**, 185 (1995).

[44] W. Nazarewicz, M. A. Riley and J. D. Garrett, Nucl. Phys. A **512**, 61 (1990).

[45] J. C. Batchelder, C. R. Bingham, K. Rykaczewski, K. S. Toth, T. Davinson, J. A. McKenzie, P. J. Woods, T. N. Ginter, C. J. Gross, J. W. McConnell, E. F. Zganjar, J. H. Hamilton, W. B. Walters, C. Baktash, J. Greene, J. F. Mas, W. T. Milner, S. D. Paul, D. Shapira, X. J. Xu, and C.-H. Yu, Phys. Rev. C **57**, R1042 (1998).

[46] K. Rykaczewski, J. C. Batchelder, C. R. Bingham, T. Davinson, T. N. Ginter, C. J. Gross, R. Grzywacz, M. Karny, B. D. MacDonald, J. F. Mas, J. W. McConnell, A. Piechaczek, R. C. Slinger, K. S. Toth, W. B. Walters, P. J. Woods, E. F. Zganjar, B. Barmore, L. Gr. Ixaru. A. T. Kruppa, W. Nazarewicz, M. Rizea, and T. Vertse, Phys. Rev. C **60**, 011301 (1999).

[47] C. R. Bingham, J. C. Batchelder, K. Rykaczewski, K. S. Toth, C.-H. Yu, T. N. Ginter, C. J. Gross, R. Grzywacz, M. Karny, S. H. Kim, B. D. MacDonald, J. Mas, J. W. McConnell, W. Nazarewicz, P. B. Semmes, J. Szerypo, and W. Weintraub, Phys. Rev. C **59**, R2984 (1999).

[48] B. Hubbard-Nelson, M. Momayezi, and W. K. Warburton, Nucl. Instrum. Methods A **422**, 411 (1999).

[49] J. F. Liang, D. Shapira, J. R. Beene, J. D. Bierman, A. Galindo-Uribarri, J. Gomez del Campo, C. J. Gross, M. L. Halbert, T. J. Harding, A. I. D. Macnab, S. P. McNeal, R. L. Varner, and K. Zhao, Nucl. Instrum. Methods A **435**, 393 (1999).

[50] T. N. Ginter, J. C. Batchelder, C. R. Bingham, C. J. Gross, R. Grzywacz, J. H. Hamilton, Z. Janas, M. Karny, S. H. Kim, J. F. Mas, J. W. McConnell, A. Piechaczek, A. V. Ramayya, K. Rykaczewski, P. B. Semmes, J. Szerypo, K. S. Toth, R. Wadsworth, C.-H. Yu, and E. F. Zganjar, Phys. Rev. **C** (to be published).

[51] S. Hofmann, in *Particle Emission from Nuclei*, edited by D. N. Poenaru and M. S. Ivaşcu (CRC Press, Boca Raton, Florida, 1989), Vol. 2, pp. 25-72.

[52] P. J. Sellin, P. J. Woods, T. Davinson, N. J. Davis, K. Livingston, R. D. Page, A. C. Shotter, S. Hofmann, and A. N. James, Phys. Rev. C **47**, 1933 (1993).

[53] K. Livingston, P. J. Woods, T. Davinson, N. J. Davis, S. Hofmann, A. N. James, R. D. Page, P. J. Sellin, and A. C. Shotter, Phys. Lett. B **312**, 46 (1993).

[54] R. D. Page, P. J. Woods, R. A. Cunningham, T. Davinson, N. J. Davis, S. Hofmann, A. N. James, K. Livingston, P. J. Sellin, and A. C. Shotter, Phys. Rev. Lett. **68**, 1287 (1992).

[55] K. Livingston, P. J. Woods, T. Davinson, N. J. Davis, S. Hofmann, A. N. James, R. D. Page, P. J. Sellin, and A. C. Shotter, Phys. Rev. C **48**, R2151 (1993).

[56] S. L. Thomas, T. Davinson, and A. C. Shotter, Nucl. Instrum. Methods A **288**, 212 (1990).

[57] R. D. Page, P. J. Woods, R. A. Cunningham, T Davinson, N. J. Davis, A. N. James, K. Livingston, P. J. Sellin, and A. C. Shotter, Phys. Rev. Lett. **72**, 1798 (1994).

[58] G. Audi and A. H. Wapstra, Nucl. Phys. A **565**, 66 (1993).

[59] S. L. Meyer, *Data Analysis for Scientists and Engineers* (Wiley, New York, 1975), p. 326ff.

[60] S. Åberg, P. B. Semmes, and W. Nazarewicz, Phys. Rev. C **56**, 1762 (1997); Phys. Rev. C **58**, 3011 (1998).

[61] F. Guzmán, M. Gonçalves, O. A. P. Tavares, S. B. Duarte, F. García, and O. Rodríguez, Phys. Rev. C **59**, R2339 (1999).

[62] S. G. Kadmensky and V. P. Bugrov, Yad. Fiz. **59**, 424 (1996); Phys. At. Nucl. **59**, 399 (1996).

[63] P. Möller, J. R. Nix, and K.-L. Kratz, At. Data Nucl. Data Tables **66**, 131 (1997).

[64] S. Hofmann, in *Nuclear Decay Modes*, edited by D. N. Poenaru (IOP, Bristol, 1996), pp 143-203.

[65] F. D. Becchetti, Jr. and G. W. Greenlees, Phys. Rev. **182**, 1190 (1969).

[66] S. Ćwiok, J. Dudek, W. Nazarewicz, J. Skalski, and T. Werner, Comp. Phys. Comm. **46**, 379 (1987).

[67] K. S. Toth, D. C. Sousa, P. A. Wilmarth, J. M. Nitschke, and K. S. Vierinen, Phys. Rev. C **47**, 1804 (1993).

[68] T. N. Ginter, J. C. Batchelder, C. R. Bingham, C. J. Gross, R. Grzywacz, J. H. Hamilton, S. D. Paul, A. Piechaczek, A. V. Ramayya, K. Rykaczewski, K. S. Toth, and E. F. Zganjar, *A search for neutron single-particle states in $^{149}Yb$ and $^{145}Er$ via proton radioactivity studies*, proposal accepted by the HRIBF Program Advisory Committee, March, 1999.

[69] K. Rykaczewski, J. C. Batchelder, C. R. Bingham, T. Davinson, T. N. Ginter, C. J. Gross, R. Grzywacz, Z. Janas, M. Karny, B. D. MacDonald, J. Mas, J. W. McConnell, A. Piechaczek, R. C. Slinger, J. Szerypo, K. S. Toth, W. B. Walters, P. J. Woods, E. F. Zganjar, W. Nazarewicz, and P. B. Semmes, Acta Phys. Pol. B **30**, 565 (1999).

[70] T. N. Ginter, J. H. Hamilton, A. V. Ramayya, J. C. Batchelder, C. R. Bingham, R. Grzywacz, S. H. Kim, J. F. Mas, J. W. McConnell, K. Rykaczewski, K. S. Toth, C.-H. Yu, C. J. Gross, A. Piechaczek, E. F. Zganjar, Z. Janas, M. Karny, and J. Szerypo, Bull. Am. Phys. Soc. **43**, 1559 (1998).